Scattering of polarized protons by nickel, strontium, cadmium, indium and tin isotopes

Citation for published version (APA):
Wassenaar, S. D. (1982). *Scattering of polarized protons by nickel, strontium, cadmium, indium and tin isotopes*. [Phd Thesis 1 (Research TU/e / Graduation TU/e), Applied Physics and Science Education]. Technische Hogeschool Eindhoven. https://doi.org/10.6100/IR134241

DOI:
10.6100/IR134241

Document status and date:
Published: 01/01/1982

Document Version:
Publisher’s PDF, also known as Version of Record (includes final page, issue and volume numbers)

Please check the document version of this publication:

• A submitted manuscript is the version of the article upon submission and before peer-review. There can be important differences between the submitted version and the official published version of record. People interested in the research are advised to contact the author for the final version of the publication, or visit the DOI to the publisher's website.
• The final author version and the galley proof are versions of the publication after peer review.
• The final published version features the final layout of the paper including the volume, issue and page numbers.

Link to publication

General rights
Copyright and moral rights for the publications made accessible in the public portal are retained by the authors and/or other copyright owners and it is a condition of accessing publications that users recognise and abide by the legal requirements associated with these rights.

- Users may download and print one copy of any publication from the public portal for the purpose of private study or research.
- You may not further distribute the material or use it for any profit-making activity or commercial gain
- You may freely distribute the URL identifying the publication in the public portal.

If the publication is distributed under the terms of Article 25fa of the Dutch Copyright Act, indicated by the “Taverne” license above, please follow below link for the End User Agreement:

www.tue.nl/taverne

Take down policy
If you believe that this document breaches copyright please contact us at:

openaccess@tue.nl

providing details and we will investigate your claim.

Download date: 04. Oct. 2023

SCATTERING OF POLARIZED PROTONS BY NICKEL, STRONTIUM, CADMIUM, INDIUM AND TIN ISOTOPES

S.D. WASSENAAR

DISSERTATIE DRUKKERIJ
wibro
HELMOND
TELEFOON 04920-23981

SCATTERING OF POLARIZED PROTONS BY NICKEL, STRONTIUM, CADMIUM, INDIUM AND TIN ISOTOPES

SCATTERING OF POLARIZED PROTONS BY NICKEL, STRONTIUM, CADMIUM, INDIUM AND TIN ISOTOPES

PROEFSCHRIFT

TER VERKRIJGING VAN DE GRAAD VAN DOCTOR IN DE TECHNISCHE WETENSCHAPPEN AAN DE TECHNISCHE HOGESCHOOL EINDHOVEN, OP GEZAG VAN DE RECTOR MAGNIFICUS, PROF. DR. S. T. M. ACKERMANS, VOOR EEN COMMISSIE AANGEWEZEN DOOR HET COLLEGE VAN DEKANEN IN HET OPENBAAR TE VERDEDIGEN OP VRIJDAG 12 NOVEMBER 1982 TE 16.00 UUR

DOOR

SIETSE DIRK WASSENAAR

GEBOREN TE LEEUWARDEN

DIT PROEFSCHRIFT IS GOEDGEKEURD
DOOR DE PROMOTOREN

PROF.DR. O.J. POPPEMA
EN
PROF.DR. B.J. VERHAAR

CO-PROMOTOR DR. P.J. VAN HALL

Oan Heit en Mem

This investigation was part of the research program of the "Stichting voor Fundamenteel Onderzoek der Materie" (FOM), which is financially supported by the "Nederlandse Organisatie voor Zuiver Wetenschappelijk Onderzoek" (ZWO).

CONTENTS

1 INTRODUCTION AND SUMMARY 1

2 THE EXPERIMENT 5
2.1 Introduction 5
2.2 Production of the polarized protons 5
2.3 Targets 6
2.4 Detection of the scattered protons 8
2.4.1 Scattering chamber and polarization monitor 8
2.4.2 Detectors 9
2.4.3 Electronic system 11
2.4.4 Data acquisition 11
2.5 Experimental procedure 12
2.6 Spectrum analysis 13
2.6.1 Translation, addition and comparison of spectra 13
2.6.2 Peak fitting 13
2.6.2.1 Kinematics 13
2.6.2.2 Peak shape 15
2.6.2.3 Background 16
2.6.2.4 Operation of PIEK 17
2.6.2.5 Results and plotting 18

3 SOME ASPECTS OF THE THEORY OF ELASTIC AND INELASTIC SCATTERING 19
3.1 Introduction 19
3.2 Optical model 20
3.3 Collective description of the inelastic scattering 21
3.3.1 Collective model 21
3.3.2 Weak-coupling model 23
3.3.3 Collective coupled channels (CC) model 23
3.4 Shell model 24
3.5 The calculation of the angular distributions 26
3.6 Core polarization 27
3.7 Reduced transition probabilities B(EL, 0→L) 28
Appendix Fast method to fit angular distributions 29

4 EXPERIMENTAL RESULTS AND COLLECTIVE MODEL ANALYSIS 33
4.1 Introduction 33
4.2 Optical model 33
4.2.1 Standard deviations of the parameters 34
4.2.2 Normalisation 34
4.2.3 Best Fits (BF) 35
4.2.4 Global Fits (GF) 45
4.2.5 Volume integrals and rms radii 45
4.2.6 Isospin dependence of optical model parameters 47
4.2.7 Isospin dependence of volume integrals and rms radii 49
4.2.8 Coupled channels fit for ^{60}Ni 49
4.3 Inelastic scattering and DWBA 51
4.3.1 Ni 53
4.3.1.1 One-phonon states of ^{60,64}Ni 53
4.3.1.2 Two-phonon states of ^{60}Ni 56
4.3.2 Sr 60
4.3.3 Cd 63
4.3.4 ^{115}In 66
4.3.5 Sn 70

5 A MICROSCOPIC ANALYSIS OF INELASTIC SCATTERING FROM ^{116}Sn AND ^{124}Sn 75
5.1 Introduction 75
5.2 Purely microscopic calculations 83
5.2.1 Effects of non-central forces 83
5.2.2 The importance of exchange 85
5.2.3 Proton and neutron contributions 85
5.2.4 Reduced transition probabilities 88
5.3 Calculations including core polarization 89

References 103
Samenvatting 107

Nawoord 111
Levensloop 112

CHAPTER 1 INTRODUCTION AND SUMMARY

The scattering of protons is an important tool for investigation of properties of atomic nuclei. These properties are reflected in the values of the parameters of the nuclear model that we adopt. Using this model and the general quantum-mechanical scattering theory, the observables are calculated and compared with the experimental results. The parameters of the model are varied in order to optimize the fit to the experimental data. When we use polarized protons as projectiles, in addition to the cross sections also analysing powers are obtained, which, in some cases are more sensitive to the values of the nuclear model parameters.

The experiments described in this work form a part of a larger program of experiments at the EUT, covering a wide range of nuclides.

The choice of the nuclei has the following reasons. From the literature it is known that the analysing powers for the first excited state of some nuclides having one closed shell, or a nearly closed shell, cannot be described with 'normal' parameters. One example is the 2^+ state of ^{54}Fe (N=28). So all our target nuclides have (nearly) one closed shell namely: ^{60,64}Ni (Z=28); ^{86}Sr (N=48); ^{88}Sr (N=50); ^{110,112,114}Cd (Z=48); ^{115}In (Z=49); ^{116,118,120,122,124}Sn (Z=50). Moreover often a series of isotopes is in itself interesting for the investigation of the effect of increasing neutron numbers on the experimental data and hence on the parameter values.

In our experiment, as described in chapter 2, we used polarized protons of 20.4 or 24.6 MeV. With the use of a special ion source it is possible to polarize the proton spins before they are accelerated by the A.V.F. cyclotron of the EUT. The energy range of the cyclotron is 3 to 26 MeV for protons. The accelerated protons are transported to a scattering chamber where some of these projectiles are scattered by the nuclei in the thin target foil. It is possible that in this process a nucleus is left in an excited state. In the detectors the energy spectrum of the scattered protons is measured. The different peaks in such a spectrum correspond to the energy levels of the target nuclide. The normalized number of counts in each peak is the differential cross section, $d\sigma(\theta)/d\Omega$, for that incident proton energy, final state and scattering angle. We have developed an automatic spectrum analysing program, that fits the peaks and sorts out all data. We always measured two spectra, which only differ in the direction of the beam polarisation $\vec{P}$, namely up (↑) and down (↓). The unpolarized cross section is now

$$\frac{d\sigma(\theta)}{d\Omega} = \frac{1}{2}\left(\frac{d\sigma(\theta,\uparrow)}{d\Omega} + \frac{d\sigma(\theta,\downarrow)}{d\Omega}\right) \tag{1.1}$$

and the analysing power is

$$A(\theta) = \frac{1}{\vec{P}\cdot\vec{n}}\left(\frac{d\sigma(\theta,\uparrow)}{d\Omega} - \frac{d\sigma(\theta,\downarrow)}{d\Omega}\right)/\left(\frac{d\sigma(\theta,\uparrow)}{d\Omega} + \frac{d\sigma(\theta,\downarrow)}{d\Omega}\right) \tag{1.2}$$

where $\vec{n}$ is the unit vector product of the linear momenta of the projectile and the ejectile.

Using an energy of around 20 MeV the direct scattering theory, as sketched in chapter 3, is supposed to be appropriate. In the application of this theory to our data, we adopt a model for the nucleus. We have used two currently available models for the nuclear structure part, namely the collective or macroscopic model and the microscopic or shell model. In the collective theory the nucleus is considered as a whole while in the microscopic model the motion of the individual nucleons is taken into account.

In chapter 4 the analysis of our data with the collective model is presented, at first for the elastic scattering and then for the inelastic scattering.

In all our cases the elastic scattering was the dominant process, which we analyzed with the optical model. With a chi-squared minimalization code the optical model parameters were calculated. The parameters found were in good agreement with standard sets parameters from the literature. Due to the additional analysing powers the parameters were well determined.

For the description of the inelastic scattering we used the distorted wave Born approximation (DWBA) or in some cases the coupled channels (CC) method. In the collective model the excited nuclear states are considered either as vibration of the nuclear surface or as rotations of a permanently deformed nucleus. So the optical model potential has non-spherical terms, which give rise to the excitation of the nucleus. The strength of this deformation is introduced as a parameter. The deformation parameters found are in good agreement with the values from the literature. In general the theoretical curves fit the experimental angular distributions well. For the description of our analysing powers no exceptional deformation parameters are needed.

For ^{60}Ni we performed some calculations with the CC approach, since for ^{60}Ni the coupling between the ground state and the first excited state is rather strong and the slope of the cross section of the 2^+ state could not be described by the DWBA. Only small differences, however, between the CC and DWBA curves were found so the more elaborate CC analyses was abandoned.

Some higher excited 2^+ and 4^+ states of ^{60}Ni could be described rather well as a mixture of one and two phonon contributions in the CC approach. By varying the mixing parameter we obtained information about the structure of these states.

^{115}In is the only odd-A nucleus, which we investigated. The L-values found with the collective DWBA analysis are in good agreement with the data from the literature. Also the deformation parameters agree well with those predicted by calculations with the weak-coupling model.

In the microscopic analysis, presented in chapter 5, the shell structure of the nucleus is taken into account. In the shell model an excitation is a jump of a valence nucleon from one shell-model orbit to another. It is assumed that the nucleons in the inner shells, the socalled core nucleons, do not partake in the microscopic process. In the field of all other nucleons the two body interaction takes place between the projectile and a valence nucleon, so an effective nucleon-nucleon interaction is needed. We used two different interactions, described in the literature. For ^{116}Sn and ^{124}Sn we performed microscopic calculations for the first 2^+, 3^- and 5^- states. We have chosen these Sn isotopes because in the literature already extensive microscopic analyses have been described, but at that time analysing power data were not yet available. In addition the spectroscopic amplitudes needed were available from recent BCS calculations. An important feature of this model for the Sn nuclei is that the Z=50 core is not taken as completely inert, but that a few proton-hole excitations are allowed.

The resulting microscopic curves, however, describe the structure and the height of the cross sections rather badly. The structure is too flat and the height too small. In the first place an imaginary contribution can be added to the microscopic contribution in order to improve the form of the cross sections. Hereto, as usual, the collective imaginary contribution is used. The importance of the diverse contributions is discussed.

In addition the height of the cross sections is increased using four methods. In all methods the enhancement of the cross section is due to the interaction of the projectile with the, up till now assumed inert, core. This is the socalled core polarization. We have developed a special search routine that could determine very fast the strengths of the various contributions. In the first two methods the core polarization is accounted for by enhancing the proton and neutron charges, so taking effective charges according to two different recipes. Either both charge parameters were varied in a fit to all observables, or the proton charge was calculated from the transition probability and the neutron charge was found from the fit to the cross section and analysing power. In the first procedure the fit to the analysing power of the 2_1^+ states was better then in the second one.

In the other two methods, which differ only a little, the core polarization is accounted for by adding real and imaginary collective terms, to the microscopic contributions. Now no effective charges are used, but a core coupling parameter appears. In all cases these methods give a good description of the data. Also now the 5_1^- state of ^{124}Sn could be described satisfactorily, since a relative large core polarization term was added.

In conclusion we can say that the elastic scattering of polarized protons us provides with reliable optical model parameters. The inelastic scattering offers a good testground for the collective and microscopic nuclear models. In both cases the analysing powers can play an important, if not decisive role.

CHAPTER 2 THE EXPERIMENT

2.1 Introduction

In this chapter we give an outline of our experimental arrangement. The second section deals with the production of the polarized protons. In section three the targets used are listed. Next the detection of the scattered protons is treated. Some comments on the measuring procedure follow in the fifth part of this chapter. The extraction of the experimental cross sections and analysing powers from the spectra is described in the last part. Additional information concerning the experiment can be found in the thesis of Melssen (Mel78).

2.2 Production of the polarized protons

For the production of the polarized protons we used an ion source of the atomic beam type. A description of the physical principles and the operation of such a source can be found a.o. in the papers of Clausnitzer (Cla56), Glavish (Gla70) and Clegg (Cle75). The ion source in our laboratory, that was developed and constructed by Van der Heide (Hei72), delivered 2-4 μA of 5 KeV protons with a degree of polarization ranging from 65% to 85%, depending on the vacuum conditions.

The injection of the protons into the A.V.F. cyclotron is done radially with a trochoidal injection system which is a copy of the Saclay one (Beu67). The electric field produced by appropriately shaped electrodes gives a force acting on the injected protons that compensates the Lorentz force due to the magnetic field of the cyclotron. We measured the transmission efficiency of the injector which was as good as 70% in a stable situation.

The acceleration and extraction of the polarized beam turned out to be rather difficult. As the aperture of the injector structure was only eight mm, probably a considerable part of the beam was cut off. So the system was very sensitive to any oscillations and instabilities during the acceleration process. First of all, an asymmetric excitation of the inner correction coils of the cyclotron proved to be necessary to get any accelerated beam. An additional problem arose from the fact that the beam did not move exactly in the median plane during the first part of the acceleration, but instead moved a bit upward (Bot81). Also the position of the dee was very important. To optimize the intensity, the injector orifice is adjustable with respect to the puller in all directions. During the experiments described in this thesis, the intensity of the extracted beam was 10-25 nA at 20 MeV and 5-15 nA at 24 MeV, with an energy-spread of 60-90 keV.

The extracted beam was transported over a distance of about 40 m to the scattering chamber. By means of five bending magnets (5, 45, 45, 30 and 30 degrees in succession), twenty quadrupoles and five steering magnets (Hag70), we achieved a spot of less than two mm in diameter on the target in the scattering chamber. The beam transport system was used in a doubly achromatic mode to get as much intensity on the target as possible. So the energy spread was, of course, the same as directly after the extraction. The scattering chamber was equipped with ten probes (diaphragms etc.), for monitoring the beam intensity and position. With these probes an accurate tuning of the beam was possible. We set as criterion that at most two per cent of the intensity should fall on a diaphragm with a three mm diameter aperture placed in the position of the target. The beam current passing through this aperture had to fall on the inner section of the Faraday cup located two meters further. So we were sure that all intensity fell on the ten mm diameter target, and that the target frame would not be hit by beam particles in order to avoid contributions to the background in our energy spectra.

2.3 Targets

As target we used self-supporting foils. All targets were obtained from A.E.R.E. Harwell, except the ^{115}In and the thin ^{116}Sn and ^{118}Sn targets which were manufactured at the KVI of the university of Groningen. Table 2.1 lists the targets that we used and gives their isotopic compositions.

Table 2.1 Isotopic composition of the used targets (in %).

Sn 1 mg/cm^2

target A	115	116	117	118	119	120	122	124
^{116}Sn	0.74	84.4	1.56	6.5	0.74	5.2	0.3	0.35
^{118}Sn	0.02	0.37	0.79	95.75	1.22	1.61	1.15	0.07
^{120}Sn	<0.05	0.20	0.12	0.5	0.39	98.39	0.15	0.26
^{122}Sn	<0.05	0.34	0.17	0.91	0.91	4.72	92.25	1.12
^{124}Sn	<0.05	2.33	1.21	3.99	1.40	5.69	1.40	83.98

Cd 1 mg/cm^2

target A	108	110	111	112	113	114	116
^{110}Cd	<0.22	92.94	3.27	2.34	0.31	<0.74	<0.05
^{112}Cd	0.05	0.24	2.01	95.53	1.34	0.71	0.05
^{114}Cd	0.29	0.18	0.15	1.75	0.31	96.97	0.34

Sr 2 mg/cm^2 mylar backing

target A	84	86	87	88
^{86}Sr	<0.05	97.6	0.68	1.73
^{88}Sr	≤0.002	0.065	0.184	99.75

Ni 1 mg/cm^2

target A	58	60	61	62	64
^{60}Ni	0.71	99.85	<0.02	<0.02	<0.02
^{64}Ni	2.14	0.94	0.05	0.43	99.44

Groningen: (≥ 0.5 mg/cm^2)

^{115}In	99.99%
^{116}Sn	95.6 %
^{118}Sn	94.9 %

2.4 Detection of the scattering protons

2.4.1 Scattering chamber and polarization monitor

For the detection of the scattered protons we used two arrays of four detectors, indicated in fig. 2.1 as D1-D4 and D5-D8, respectively. One array was mounted on the upper lid, the other on the lower lid of the vacuum chamber. The detectors attached to the upper lid were placed at a distance of 25 cm from the target, and had an angular acceptance of 1 degree. They were used for measurements at scattering angles between -20 and +120 degrees. The lower detectors were located at 12.5 cm from the target and were used for the measurements at angles from -60 till -165 degrees. The angular acceptance of the detectors in this backward block was two degrees.

Perpendicular to the scattering plane i.e. parallel to the polarization axis of the incident protons, we placed two detectors to monitor the beam intensity. This monitoring is then independent of the direction of the beam polarization. These monitor detectors were placed at scattering angles of 45 degrees above and below the reaction plane defined by the target and D1-D8. We used the sum of the counts from these out-of-plane detectors as a clock signal for the reversing of the polarization direction.

In the scattering chamber eight targets could be installed. Their positions were controlled remotely. One of these targets was the 3 mm aperture mentioned before.

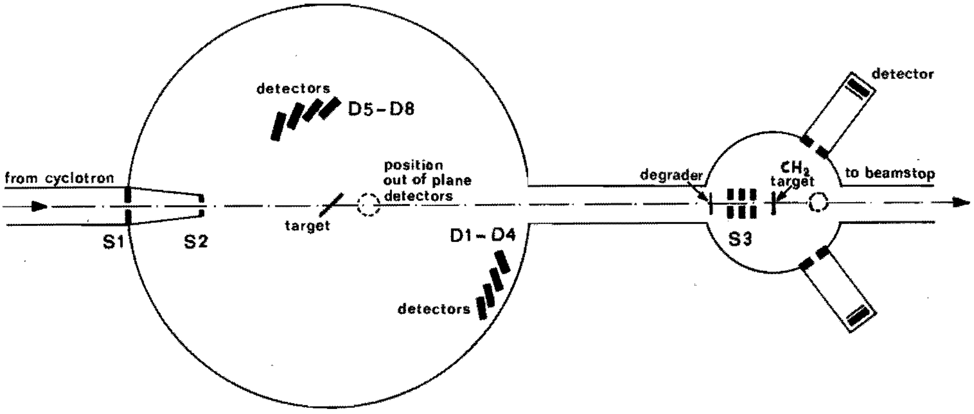

Fig. 2.1 The main scattering chamber, ∅ 56 cm × 18 cm and the polarization monitor ∅ 18 cm × 13.5 cm.

Downstream of the main scattering chamber the beam polarization was monitored in a separate smaller scattering chamber. The analysing power of the elastic scattering from ^{12}C at a scattering angle of 52.5 degrees is nearly independent of the energy from 12 till 16 MeV, and equals 67% (±1%), see H.O. Meyer et al., Nucl. Phys. A269 (1976) 269. So we chose this angle and energy range for the polarization monitoring. It was then necessary to degrade the beam energy to a mean energy of 16 MeV before the protons were scattered by a thin polyethylene foil.

An additional detector was placed above the reaction plane, like in the main scattering chamber, to monitor the beam intensity on the polyethylene target. Since the reversal of the polarization direction is timed by the two monitor detectors in the main scattering chamber, it could happen that inhomogeneities (e.g. pinholes) in the targets combined with a small drift in the beam position would result in unequal integrated intensities on the polyethylene target for the two polarization directions. This detector allowed us to correct the beam polarization for such effects. Fortunately the measured differences were always small, so the beam polarization was measured correctly.

As an accurate and extra check for the value of the beam polarization we always measured the elastic scattering from ^{12}C in the main scattering chamber. We compared the angular distribution of the analysing power with data from the literature and with our own previous measurements. So the absolute value of our analysing powers was determined well.

2.4.2 Detectors

The eight detectors, D1-D8, were two mm thick Si surface barrier detectors purchased from ORTEC. They were positioned askew at 45 degrees, as suggested by fig. 2.1. So the effective thickness of the detectors was increased up to about 3 mm.

During the experiments at 24 MeV on the Sr isotopes we used in the forward detector block a stack of two such detectors in telescope mode. The four detectors in the backward detector block were three mm drifted Si(Li) detectors from Philips, also placed askew.

As monitor detectors we used 0.5 mm thick Si surface barrier detectors. We degraded the energy of the impinging protons to 8 MeV, so that they were stopped in these detectors.

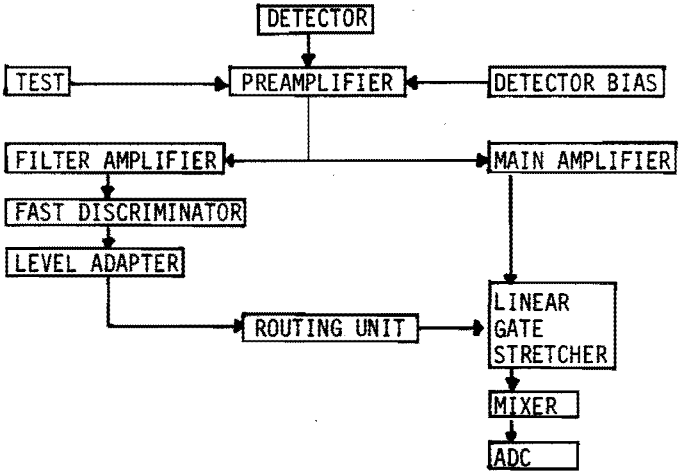

Fig. 2.2 The electronic system for one detector.

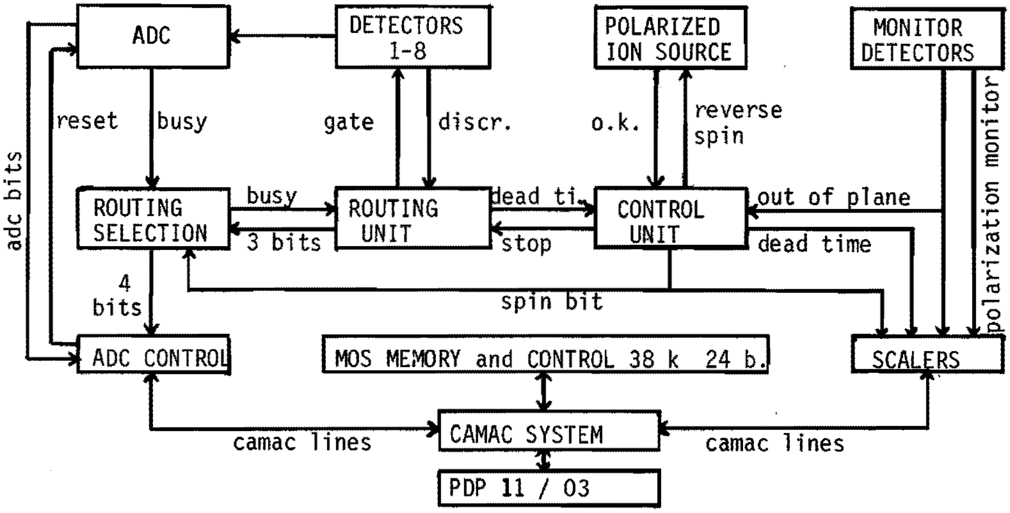

Fig. 2.3 The complete electronic system.

2.4.3 Electronic system

The electronics used in our experiments consisted mainly of standard NIM and CAMAC modules. A few special purpose devices for routing and controlling the analog signals have been designed and built in our laboratory. The relevant block diagrams for one detector and that of the complete electronic system are shown in figs. 2.2 and 2.3, respectively.

The use of fast logic permitted us to incorporate a pile-up inspection in the routing unit. This pile-up inspection has a pulse resolving time of about 300 nsec. The routing unit enabled the processing of one detector signal while inhibiting the signals in the other linear gate stretchers. It, moreover, generated the three detector identification bits for the routing selection unit. The busy signals of the ADC and of the control unit (stop signal) were combined in the routing unit to the dead time signal, which was sent to the scalers and the control unit.

The control unit had the following tasks: it reversed the spin direction in the ion source when the two out-of-plane detectors had together produced a preset number of counts. In addition, it supplied a spin bit for the routing selection unit and the scalers. After a preset number of reversals of the spin direction, the run was stopped. Then the results could be written onto a floppy disk. If the ion source accidently did not function correctly the control unit stopped the experiment.

Also the scalers have been developed in our laboratory using the Eurobus system (Nij79). Their functions were controlled via the CAMAC system.

2.4.4 Data acquisition

Our data acquisition system, developed by De Raaf, has been described in the literature (Raa79), so only a few details are mentioned here. The system worked independently of the PDP11 computer giving a minimum of computer overhead. Moreover, the data collected in the external MOS memory were always preserved. The functions of the MOS memory and the ADC controller were set via the CAMAC system by the PDP terminal.

Also, all data were processed via the CAMAC crate. From the terminal of the PDP11 computer we started and stopped the experiments, read the scalers, listed maxima in spectra and controlled the MOS memory.

The measured spectra were written onto floppy disks for further analysis. A connection with the central university computer (Burroughs B7700), running via a second PDP11 enabled us to store the spectra on a large disk pack.

2.5 Experimental procedure

When the beam had been focussed on the target in the scattering chamber, we first determined the energy of the incoming protons using the cross over method (Bar64). The beam energy was deduced with an accuracy of 0.1 MeV. The preset numbers of counts of the control unit were adjusted so that the spin direction reversed about once in a minute. This reversion rate was fast enough to avoid false asymmetries that could occur due to drifts. Most spectra were measured in runs of one hour or less. We divided the total time, needed to collect a desired number of counts into peak of interest, in parts of about one hour. This method was preferred to making only one long run which otherwise would have been more risky because of drift in amplifiers, beam quality variations and possible break downs during the run. In practice the separate spectra were nearly equal and could be added without problems.

The relative angular acceptances of the detectors, which were needed for the calculation of the cross sections, were deduced by taking spectra with different detectors at the same angle. Afterwards, the deduced cross sections and analysing powers of the various runs were compared, which was a good check on the reliability of the experimental data.

Since all targets contained more or less contaminations of H, C and O, we always measured the scattering from a mylar target (contains H, C and O) at each angular setting of the detector blocks. We used these spectra in order to correct the peak contents that were a sum of the contributions of the scattering from an isotope of interest and a contamination.

2.6 Spectrum analysis

2.6.1 Translation, addition and comparison of spectra

As mentioned before, the spectra were sent from the PDP11 to the B7700 computer and stored on a disk. First of all, these data had to be translated from PDP11 words to B7700 words. A program called CHI was written for this purpose which, moreover, compared spectra that were measured at the same angular settings of the detectors. For each combination of two equivalent spectra a normalized chi squared value was calculated (Nij78). If this value was near unity, then those spectra were added, otherwise e.g. the gain of the amplifiers, the scattering angles or the detector quality had been different for the two spectra. In this case the spectra were not added, but analysed separately.

2.6.2 Peak fitting

In order to analyse the spectra we wrote a peak fitting program called PIEK, which is an extended and adapted version of the program POESPAS written by Blok and Schotman (Blo75). With this program (sketched below), it was possible to analyse the measured spectra nearly automatically. In fig. 2.4 we show an example of our energy spectra with the fit found. In the fitting procedure the parameters of the shape, height and position of the peaks together with two background parameters were varied. The starting values of these parameters were partly given as input and partly deduced by PIEK.

In the first subsection we treat the energy calibration calculated from the kinematics. The starting values of the peak position parameters are deduced by this calibration. More details about the peak shape and the background follow in the next subsections. In subsection four, the operation of the program and some options of it are noted. The last subsection deals with the sorting out of the results and our general plot program.

2.6.2.1 Kinematics

The kinematics of the reaction were taken into account in PIEK. The expected energy spectrum was calculated from the input data such as the masses of the incoming and outgoing particles, the laboratory angle of the detectors and the composition of the target. The target

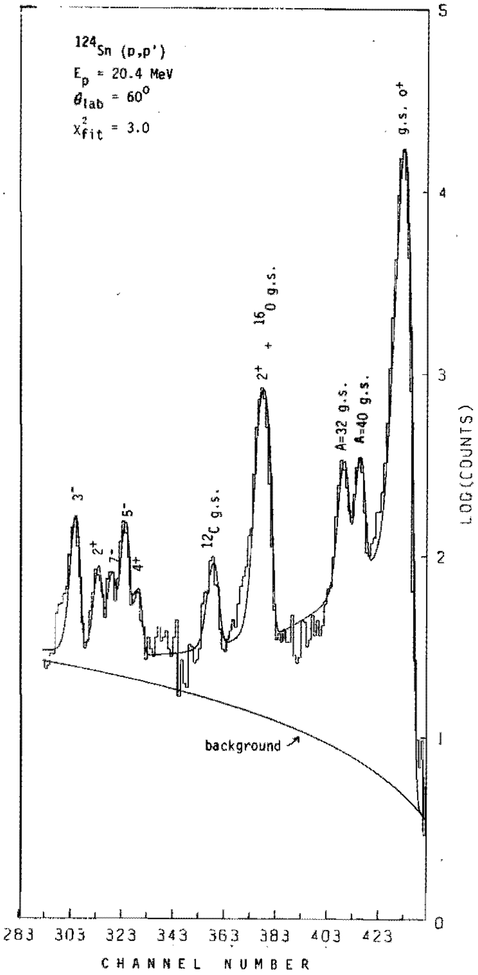

Fig. 2.4
Spectrum of ^{124}Sn fitted with PIEK.

composition was a list of names of elements in the target with their mass numbers A and proton numbers Z. After every name followed the Q values of the states we wanted to analyse and some further identification (spin etc.). Since our energy resolution did not enable us to look for new excited states in the nuclides under investigation, we took the spectroscopic data from the literature, e.g. the Nuclear Data Sheets. With these data the energies were calculated of the outgoing particles, leaving the target nuclides in the various excited states. By sorting out these energies the sequence of the expected peaks was found and possible overlaps were noted.

In order to match this calculated sequence to the actual peaks in the energy spectrum we applied the following procedure. The position of a peak in a spectrum was calculated from an energy calibration. A linear dependence was sufficient, so two calibration parameters i.e. the offset and the conversion gain were needed. As starting values we took, of course, the digital offset of the ADC and the conversion gain that followed from the setting of the nominal energy at channel number 990. To refine the starting values the following procedure was applied. The peak of the elastic scattering from the heaviest target nuclide was identified with the last large maximum in the spectrum, corresponding with the highest energy. Using the starting values of the calibration, the positions of the other peaks were calculated and the differences with nearby lying maxima were found. These differences were minimized by varying the calibration parameters. Only a selected number of large peaks was used in this calibration procedure. It was also possible to vary the detector angle and the energy of the incoming particles, in order to achieve a closer agreement between calculated and experimental peak positions.

Every maximum in the spectrum that occurred within five channels from a calculated position of a peak was identified as being the peak in question, and labeled with A, Z, J and the element name. With this identification it was possible to take into account the kinematical broadening, by multiplying the shape parameters of the peak by a mass dependent factor. After completing the spectrum analysis, these identification data were used again for sorting out the results and for the calculation of the transformation from the laboratory system to the centre-of-mass system.

2.6.2.2 Peak shape

In a peak fitting program it is necessary to define a standard peak shape. The most convenient way is to choose a continues function with a continues derivative. Because a proper choice of this function determines the quality of the fit we discuss our peak shape here. We started with the peak shape used in the program POESPAS (Blo72, Blo75), which is a asymmetrical gaussian with at the high energy side an exponential tail and at the other side a long double exponential tail. So the peak shape f(x) consists of four regions, centered aroun p_1:

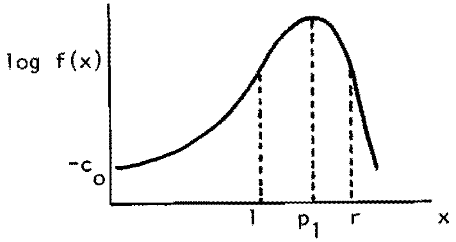

Fig. 2.5
The peak shape.

$$\begin{aligned}
x &< l &&: \quad f(x) = \exp\left\{c_l\, e^{-p_5(p_1-x)} - c_o\right\} \\
l &\leq x < p_1 &&: \quad f(x) = \exp\left\{-\left(p_3(p_1-x)\right)^2\right\} \\
p_1 &\leq x < r &&: \quad f(x) = \exp\left\{-\left(p_4(x-p_1)\right)^2\right\} \\
x &\geq r &&: \quad f(x) = \exp\left\{-\, p_6(x-p_1) + c_r\right\}
\end{aligned}$$

The shape parameters are p_3-p_6; c_o is a constant and the values of c_l, c_r, l and r are determined by the requirement that at x=l and x=r the function f(x) and its derivative are continuous. This shape, however, was designed for the analysis of rather narrow peaks (e.g. for spectra taken with a spectrograph), while we had rather broad peaks, since we used surface barrier detectors. Solid state detectors always give peaks with a long tail at the low energy side, which are difficult to describe with an analytical function with only a small number of shape parameters.

Ultimately we found that the sum of a large asymmetric peak, with at both sides single exponential tails and a lower peak with a long double exponential tail at the low energy side, gave the best results. The two functions had different width, height and tail parameters, but the ratios of these parameters were fixed, and were deduced by experience. So the number of shape parameters was the same as in POESPAS, but our shape could describe the low energy tail better.

2.6.2.3 Background

Since a proper choice of the starting values of the background parameters turned out to be very important, we have developed the following procedure. The two parameters were calculated from a linear least squares fit through a number of minima between the peaks. These minima were corrected for expected contributions of nearby peaks. The correction was calculated with the starting values that were already available. In our analysis we took a linear background, since a quadratic background did not produce better results.

2.6.2.4 Operation of PIEK

The normal operation of the program PIEK was as follows: we first fitted the sum spectrum, which is the sum of a spin up and a spin down spectrum, with four general peak shape parameters, two parameters for the background and for every peak a height parameter. We allowed the positions of the peaks to be shifted from the calculated value. This shift was restricted to one channel or less. All peaks in our calculated energy spectrum were fitted simultaneously. The different peaks had the four shape parameters in common, namely the width parameters of the gaussians and the tail parameters. Only their individual heights were fitted. So we fitted the complete spectrum with basically one peak shape and one continuous background function. With this possibility one of the drawbacks of the POESPAS program, where every multiplet was fitted separately with its own shape and background, was overcome.

Also peaks that overlapped each other were fitted reliably since the peak shape is determined mainly by the large peaks, and the background is determined by the complete spectrum. Completely overlapping peaks are treated as one peak but not stored on the file of results.

The up and down spectra were fitted using parameters found from the fitting of the sum spectrum. Here we fixed the peak shape and the position parameters, only the height and background parameters had to be refitted. Sometimes the background was also fixed at half of the value found in the fitting of the sum spectrum. So the calculation of the analysing powers was not obscured by differences in peak positions or shape.

A check of the fitting process was the difference between the contents of a peak in the sum spectrum and of the sum of the contents of the corresponding peaks in the up and down spectra. In general this difference was small.

Since the total numbers of parameters must be less then 31, we sometimes used the option that instead of all separate peak positions, the two calibration parameters were varied.

After the peak identification was done it was possible to fit a smaller part of the spectrum, e.g. only one multiplet. This option was especially effective in the case of tiny peaks superimposed on a large background. In that case we forced the background to go through the minima around the first and last channels that were fitted.

2.6.2.5 Results and plotting

The results of all fittings were stored on a disk file, which afterwards was sorted out. The normalizations of the various runs and of the detector efficiencies were adjusted if needed. Values at equal angles were compared and the weighted averages were calculated. The resulting data: cross sections transformed to the centre-of-mass system and the analysing powers were punched, for use in the program that stored all our experimental data on disk pack. This file of experimental data was accesible to the optical model codes and the general plot program.

This plot program can be seen as the link between the experimental data and the theoretical curves calculated by the optical model and DWBA programs. It calculates the scaling factors and deformation parameters by normalizing the theoretical curve to the experimental cross section in a given angular range.

In conclusion we can say that the spectrum analysis works automatically for a large part, from spectra up to tables and plots of experimental data and theoretical curves.

CHAPTER 3 SOME ASPECTS OF THE THEORY OF ELASTIC AND INELASTIC SCATTERING

3.1 Introduction

The scattering of nucleons from an atomic nucleus has to be described by quantum-mechanical scattering theory. In our case of a not too low energy of the incoming particles we only have to deal with the theory of direct reactions (Aus70). The general scattering theory gives us expressions for the differential cross section and the analysing power as sums over the products of the transition matrix elements T_{fi}, the amplitudes of the outgoing scattered wave for a specific initial channel i and final channel f.

In order that the scattering theory can be applied to the scattering of protons, we have to choose a model for the nucleus. To describe the observed phenomena we have two alternatives: the collective or macroscopic and the microscopic approach. In collective theories the nucleus is treated as a whole with respect to the projectile, while in the microscopic model the projectile interacts with the individual nucleons.

The scattering process can be elastic or inelastic. When the inelastic scattering is strong compared to the elastic process a coupled channels (CC) theory is appropriate, otherwise these processes can be treated separately, i.e.: the optical model for the elastic and the distorted wave Born approximation (DWBA) for the inelastic scattering.

In section 3.2 we discuss the optical model. Then the calculation of the inelastic angular distribution from the transition amplitudes is treated. In the next two sections the calculation of these transition amplitudes with the collective and microscopic DWBA is discussed. Section 3.6 gives us some formulae for the combined collective and microscopic approximation. In the last section, 3.7, the calculation of the reduced transition probabilities B(EL) is given.

3.2 Optical model

The first step in our theoretical analysis consisted of the search for a set of optical model parameters in order to fit the experimental elastic cross sections and analysing powers as well as possible. These optical model potentials were needed in all further calculations, of the inelastic scattering. The conventional optical model potential has been used, of which we give here the explicit form:

$$\begin{aligned} U(r) = {} & V_c(r,r_c) - V_o\, f(r,r_o,a_o) + \\ & - i\,\{W_V\, f(r,r_i,a_i) + 4a_i\, W_D \frac{d}{dr} f(r,r_i,a_i)\} + \\ & + \left(\frac{\hbar}{m_\pi c}\right)^2 V_{so} \frac{1}{r}\frac{d}{dr} f(r,r_{so},a_{so})\; \vec{\sigma}\cdot\vec{l} \end{aligned} \qquad (3.1)$$

wherein f is the usual Woods-Saxon function:

$$f(r,r_x,a_x) = \left[1 + \exp\left(\frac{r - r_x A^{1/3}}{a_x}\right)\right]^{-1}$$

The parameters that can be varied are the strengths V_o, W_V, W_D and V_{so} and the geometric parameters r_c, r_o, a_o, r_i, a_i, r_{so} and a_{so}. We have tested the addition of a real central surface term, as suggested by Sinha (Sin75) and of an imaginary spin-orbit part to the optical model potential. These terms, however, turned out to be negligible, see section 4.2.4.

Since we performed no absolute measurement of the cross section, we normalized the experimental elastic cross section to the optical model value. In our optical model analysis the normalization was left free, in other words: every turn of the search procedure the normalization was calculated from the minimalization of the chi squared value of the cross section, $\partial\chi^2/\partial N=0$. We used the complete angular distribution of the cross section (and not only the forward part) for the derivation of the normalizations. In this way the absolute values of the elastic and inelastic cross sections were deduced.

The standard deviations for the parameters p_i were calculated from a correlation matrix (Ros53, Vos72):

$$(\Delta p_i)^2 = (C^{-1})_{ii} \qquad (3.2a)$$

where

$$C_{kl} = \frac{1}{2}\frac{\partial^2}{\partial p_k \partial p_l}\chi^2 . \qquad (3.2b)$$

We used these errors as indications for the quality of the minimalization process (see section 4.2.1). In order to prevent an underestimation of the absolute errors one should multiply them with a factor $(\chi^2/N_f)^{\frac{1}{2}}$, where N_f is the number of degrees of freedom, defined as the number of experimental points minus the number of varied parameters (Ros53, Vri77).

From the optical model potentials some quantities can be derived, which fluctuate less than the various parameter sets in a certain mass region. These quantities are the volume integral defined by:

$$J = \int U(r)\, d\vec{r} \qquad (3.3)$$

and the root mean square (rms) radius:

$$\langle R^2\rangle^{\frac{1}{2}} = \left(\int U(r) r^2 d\vec{r}/J\right)^{\frac{1}{2}}$$

We computed these values for the real central, imaginary central and the real spin-orbit part of the optical model potential. In section 4.2 we compare these values with results from folding models (Gre68) and other optical model theories (Bri77, Bri78).

3.3 Collective description of the inelastic scattering

3.3.1 Collective model

In the collective model the excited states of a nucleus are supposed to be either rotations of a permanently deformed nucleus or vibrations of a spherical nucleus (Boh53, Boh75). For the calculation of the cross section and analysing power of the inelastic scattering we mostly used the collective, first order, distorted wave Born approximation (DWBA). There are two situations for which we cannot apply such a DWBA analysis:

1. The coupling between the ground and excited state is strong. This is in particular the case for the permanently deformed nuclei. Then a coupled channels (CC) analysis is needed, see section 3.4.3.

2. Higher order processes are important, e.g. the first order process is forbidden. Here again the CC method should be applied.

We now give here some basis formulae for the calculation of the transition amplitudes for the collective DWBA. From these amplitudes the cross sections and analysing powers can be calculated as will be described in section 3.5. For an even-even nucleus and a central collective interaction that causes the transition, we obtain after a multipole expansion the following expression for the transition amplitude (Aus70):

$$T_{fi}(\vec{k}_f,m_f,M_f;\vec{k}_i,m_i,M_i) = \sum_{LSJ} C_c \int \chi_f^-(\vec{r})\, F_{LSJ}(r)\, Y_{LM}^*(\theta)\, \chi_i^+(\vec{r})\, d\vec{r} \tag{3.5}$$

with indices i for the initial and f for the final state and where

$\vec{k}$ = wave number,

χ = the distorted wave function,
+ labels the incoming, - the outgoing wave,

Y_{LM} = the spherical harmonic,

C_c = some Clebsch Gordon coefficients,

s = spin of the particle,

m = projection of the particle spin, the quantization axis is chosen according to the Basel convention,

M = projection of the total transferred angular momentum J,

θ = scattering angle,

$\vec{L}$ = $\vec{J}-\vec{S}$ the transferred orbital angular momentum,

$\vec{S}$ = $\vec{s}_i-\vec{s}_f$ the transferred spin, being 0 ot 1,

$\vec{J}$ = $\vec{J}_i-\vec{J}_f$ the transferred total angular momentum, and

F_{LSJ} = the collective form factor.

For the first order vibrational excitation of the nuclear surface or the rotational excitation of a permanently deformed axial symmetric even-even nucleus the collective form factor is proportional to the derivative of the optical model potential U(r) (Tam65):

$$F_{LSJ}(r) = \beta_L\, R\, \frac{dU(r)}{dr} \tag{3.6}$$

with

R = the radius of the undeformed nucleus and

β_L = the deformation parameter.

In all our calculations the complete optical model potential has been deformed so we have three parts contributing to the inelastic scattering: the real central plus coulomb part, the imaginary central and the real spin-orbit part. The spin-orbit form factor had the full Thomas form. For a good description of the analysing power this form is absolutely needed (She68, Ray71, Ver72, Ver74). In principle it is possible to give these three collective interactions different deformation parameters.

3.3.2 Weak-coupling model

If the target nucleus is not an even-even nucleus, but can be seen as a core plus or minus one nucleon then the weak-coupling model may be applied to calculate the inelastic scattering (Sha61, Bla59). In this model the extra nucleon or hole is coupled to a collective phonon. If the nucleon or hole has a total angular momentum j then the parent state with momentum L is split up into a multiplet of states with total angular momenta ranging from |L-j| till L+j. In this case the transition amplitudes for these multiplet states are given by:

$$T(J_i \to J_f) = \left(\frac{2J_f + 1}{(2J_i+1)(2L+1)}\right)^{\frac{1}{2}} T_{parent}(0 \to L) \qquad (3.7)$$

Moreover the weighted average excitation energy should be equal to the excitation energy of the parent state. We have applied this model for the description of the scattering from ^{115}In in section 4.3.4.

3.3.3 Collective coupled channels (CC) model

A CC analysis is needed if the coupling between states is strong, so that a separation of the channels as done in the DWBA is no longer a reliable approximation. A strong coupling between the ground state and an excited state is reflected by a large deformation parameter.

In a CC analysis the optical model parameters should be deduced by fitting the ground state and the strongly coupled excited state(s) simultaneously. For ^{60}Ni we have performed such a search, see section 4.2.8, in order to find the effect on the slope of the cross section of the 2_1^+ state.

Due to the higher order terms in the CC calculation now also non-natural parity states and first-order forbidden states can be described. For some higher excited states of ^{60}Ni, see section 4.3.1, we have done a second order vibrational CC calculation. We investigated the mixing of the first and second order contributions to the angular distributions.

3.4 Shell model

With the collective model it is not possible to describe the inelastic scattering from all states of a nucleus. We know that some excited states have a predominantly single-particle character. For such states a microscopic calculation is appropriate. But also states that could be described very well with the collective model should be described microscopically by the sum of all contributing single-particle transitions.

In the microscopic DW theory the shell structure of the nucleus is taken into account, so shell model wave functions must be calculated. The projectile interacts through an effective nucleon-nucleon interaction with the valence nucleons of the target nucleus. By this interaction a valence nucleon can be excited into a different state.

Apart from the direct contribution it is also possible that the valence nucleon interchanges its role with the projectile, which gives an exchange contribution to the transition amplitude. So due to the antisymmetrization of the wave functions there are exchange contributions.

In the microscopic antisymmetrized DWA the transition amplitude can be expressed as the sum of the contributing single-particle transition amplitudes (Ger71):

$$T_{fi} = \sum_{j_1 j_2} S(j_1 j_2 J_i J_f J) \langle J_i M_i J M | J_f M_f \rangle \; T_{sp}(JM) \qquad (3.8)$$

The indices 1 and 2 refer to the two single-particle valence states involved. The sum over j_1 and j_2 means that all possible combinations of the proton and neutron single-particle states giving the right J^π value, are included with their spectroscopic amplitudes S. The single particle transition amplitudes T_{sp} are:

$$T_{sp}(JM) = \sum_{m_1 m_2} (-)^{j_1-m_1} \langle j_1 j_2 - m_1 m_2 | JM\rangle \times$$

$$\langle \chi_f^-(0)\phi_2(1)|V_{eff}|\chi_i^+(0)\ \phi_1(1) - \chi_i^+(1)\ \phi_1(0)\rangle \qquad (3.9)$$

The second term describes the exchange contribution, further

χ = again the distorted wave function
0 labels the projectile and
1 the valence nucleon,
ϕ = bound state single-particle wave function depending on j and m,
V_{eff} = the effective nucleon-nucleon interaction.

Moreover we have introduced the reduced spectroscopic amplitudes S, which read in second quantization

$$S(j_1 j_2 J_i J_f J) = \frac{1}{\sqrt{2J_f+1}} \langle\Phi(J_f)||\left(a^\dagger(j_2)\ a(j_1)\right)_J||\Phi(J_i)\rangle \qquad (3.10)$$

They weigh the contributions of the various single-particle transitions and should be derived from separate shell model calculations. $\Phi(J)$ is a shell model wave function.

The transformation from the i^L convention for the spherical harmonics used in these theoretical calculations to our convention gives the following phase factor for the spectroscopic amplitudes:

$$(i)^{L+l_1-l_2} \qquad (3.11)$$

The quantum numbers of the states involved in above single-particle transition are (n_1,l_1,j_1) and (n_2,l_2,j_2), respectively, while the transferred angular momentum equals L.

One of the difficulties one encounters in microscopic analyses lies in finding the proper effective nucleon-nucleon interaction; effective because of the influence of all other nucleons of the target nucleus on the free nucleon-nucleon interaction. Hamada and Johnston (Ham62), among others, have derived a free nucleon-nucleon interaction from the phase shift analysis of nucleon-nucleon scattering. This interaction is made effective by truncating it, i.e. using only the part beyond a certain separation distance for which we used a value of 1.05 fm. Another possibility is to use a phenomenological effective interaction like that of Austin (Aus79).

Thus far we discussed the central part of the nucleon-nucleon interaction. This interaction has to be completed with non-central parts, namely a tensor and a spin-orbit part. We used hereto the interactions of Eikemeier and Hackenbroich (Eik71) or those of Sprung (Spr72). Though these terms have asmall contribution to the transition amplitudes, they could be of importance for the evaluation of the analysing powers.

In above interactions no imaginary part is included. An oftenly followed approach is that of Love and Satchler who added the collective imaginary transition amplitude to the microscopic one (Lov67). Another approach is that of Brieva, Rook and Georgiev (Bri77, Bri78) who have developed a method to derive a complex effective nucleon-nucleon interaction from a free one. They solved a Bethe-Goldstone type integral equation in order to find this complex interaction. In addition, using a folding model in nuclear matter, they also could derive a microscopic optical model potential.

3.5 The calculation of the angular distributions from the transition amplitudes

The angular distributions of the inelastic scattering are calculated from the transition amplitudes (Aus70). In the previous two sections we sketched the calculation of these transition amplitudes by collective and microscopic models.

The differential cross section is expressed in the transition amplitudes as follows:

$$\frac{d\sigma(\theta)}{d\Omega} = \frac{1}{2s_i+1}\,\frac{1}{2J_i+1}\,\frac{\mu_i\mu_f}{(2\pi\hbar)^2} \sum_{m_i m_f M_i M_f} |T_{fi}|^2 = C \sum |T_{fi}|^2 \qquad (3.12)$$

with

T_{fi} = transition amplitude, see eqs. (3.5) or (3.9) (being in general the sum of several transition amplitudes),

μ = reduced mass.

Also the analysing power is expressed in the transition amplitude:

$$A(\theta) = \frac{C}{\sigma(\theta)} \sum_{m_i m_f M_i M_f} (-)^{\frac{1}{2}-m_i}\, |T_{fi}|^2 \qquad (3.13)$$

3.6 Core polarization

It is not realistic, however, to think that only the valence nucleons contribute to the transition amplitude. Also the remaining core nucleons do contribute, in a similar way as in the collective model (Lov67). In other words the core is 'polarized', so in general we need a combination of the collective and microscopic model.

There are two possibilities to bring the core polarization into account. Either the effective charges of the protons and neutrons can be enhanced or the core polarization term can be added to the microscopic interaction.

The effective charge method is a.o. followed by Terrien (Ter73). In this approach the effective charges e_p and e_n are varied in order to fit the observables. So the total transition amplitude (we omit now the subscripts fi) is then:

$$T = e_p T_p + (e_n+1) T_n + T_I$$

where T_p and T_n are proton and neutron part of the microscopic transition amplitude. T_I is the collective imaginary contribution.

In the core ploarization approach the prescription of Love and Satchler is followed. If the initial and final channel potentials are the same then the multipole component of the effective force is given by (Lov67, Ger71):

$$F_{L,\mathrm{core}}(r(0),r(1)) = y_L\, R_{om}(0)\, \frac{dU_{om}(r(0))}{dr(0)}\, R_{bs}(1)\, \frac{dU_{bs}(r(1))}{dr(1)} \tag{3.14}$$

where

U_{bs} = the shell model potential of the valence nucleon (1) and

U_{om} = the optical model potential of the scattered proton (0).

Comparing this equation with eq. (3.6) we see that the direct core polarization strength y_L can be calculated in a similar way as the deformation parameter β_L, since each valence term will become a factor

$$<\phi_1(1)\ |R_{bs}(1)\ dU_{bs}(r(1))/dr(1)|\ \phi_2(1)>$$

in the sum (3.9) while, apart from this factor, all transition amplitudes

$$<\chi_f^-(0)\ |R_{om}(0)\ dU_{om}(r(0))/dr(0)|\ \chi_i^+(0)>$$

are equal. In this approach the total transition amplitude is:

$$T = T_p + T_n + y_L T_{core}$$

The strength y_L can be varied in order to fit the observables.

3.7 Reduced transition probabilities B(EL,0→L)

Analogous to the reaction amplitudes also the reduced electromagnetic probabilities can be calculated with a collective or a microscopic model. In the collective model (Boh75) we used the deformation parameters found from the scaling of the theoretical to the experimental cross section:

$$B(EL,0\rightarrow L) = \left((3/4\pi)\ e\ Z\ R_{eq}^L\ \beta_L\right)^2 \qquad (3.15)$$

Here we introduce an equivalent transition radius R_{eq}, which equals the Coulomb radius R_c for a uniform charge distribution. For the more realistic Woods-Saxon distribution this radius is (Owe64):

$$R_{eq}^L = \frac{r_o \int df(r,r_o,a_o)/dr_o\ r^{L+2}\ dr}{3 \int f(r,r_o,a_o)\ dr} \qquad (3.16)$$

In our calculations we used for this Woods-Saxon distribution the parameters of the real central optical model potential. R_{eq} is L-dependent but does not differ much from R_c.

In the microscopic model, using the effective charge approach, the transition probability is

$$B(EL,0\rightarrow L) = (e_p\ D_{pv} + e_n\ D_{nv})^2 \qquad (3.17)$$

where e_p and e_n are the effective charges of the protons and the neutrons. D_{pv} and D_{nv} are the sums of contributions of the electromagnetic field interacting directly with the valence protons and neutrons, respectively. We give here D_{pv} to full extent (Bru77):

$$D_{pv} = \left[\frac{(2J_f+1)}{(2L+1)(2J_i+1)}\right]^{\frac{1}{2}} \sum_{j_1 j_2} S_p(j_1 j_2 J_i J_f J)\ <\phi_1||r_p^L||\phi_2> \times e \qquad (3.18)$$

$$\langle\phi_1||r_p^L||\phi_2\rangle = (-)^{j_1+\frac{1}{2}}\left[\frac{(2j_1+1)(2j_2+1)(2L+1)}{4\pi}\right]^{\frac{1}{2}} \times \begin{pmatrix} j_1 & L & j_2 \\ -\frac{1}{2} & 0 & \frac{1}{2} \end{pmatrix} \frac{1}{2}\left(1 + (-)^{l_1+l_2+L}\right) \langle r^L\rangle \tag{3.19}$$

$$\langle r^L\rangle = \int \phi_1(r)\, r^{L+2}\, \phi_2(r)\, dr \tag{3.20}$$

The same spectroscopic amplitudes, S, as for the calculation of the transition amplitude are used (eq. (3.10)). For the neutron transitions equal formulae hold.

In the core polarization model the transition probability is the sum of the contributions of the electromagnetic field interaction directly with the valence (index v) particles and indirectly via the core (index c). The valence particles here are protons (p) since the effective charge of neutrons is 0. So we get:

$$B(EL,0\rightarrow L) = (D_{pv} + y_L D_{pc})^2 \tag{3.21}$$

with

$$D_{pc} = \frac{3}{4\pi} Z R_c^L y_L \times e \times \left[\frac{(2J_f+1)}{(2L+1)(2J_i+1)}\right]^{\frac{1}{2}} \sum_{j_1 j_2} S_p(j_1 j_2 J_i J_f J) \langle\phi_1||R_c \frac{dU_{p,bs}(r)}{dr}||\phi_2\rangle \tag{3.22}$$

where $U_{p,bs}(r)$ is the bound state potential for a proton single-particle state.

In chapter 5.4 we have applied both approaches. We fitted then the angular distributions and the transition probability simultaneously.

APPENDIX: Fast method to fit angular distributions

In general we will have a sum of transition amplitudes T_j, that form the total transition amplitude:

$$T = \sum_{j=1}^{n} (a_j+ib_j)\, T_j \,. \tag{A.1}$$

with complex weights (a_j+ib_j). These weights could be strengths of the effective interactions, or deformation parameters or effective charges.

Often we varied these weights in order to find an optimal fit to the experimental inelastic angular distributions. In section 3.6 some examples can be found.

In order to speed up the computation we developed the following procedure. Instead of using these n legnthy T matrices, each consisting of 6916 complex numbers, it is possible to calculate the angular distributions from 192 n^2 real numbers, which we shall call 'partial' cross sections and analysing powers. This made a single calculation about a factor of hundred faster. Now a search procedure in order to find the optimal values of the complex weights, is more feasible, since the 'partial' angular distributions have to be calculated only once. Also in case that the separate transition amplitudes are not available the method is applicable, if we can compute the 'partial' cross sections and analysing powers, as defined below, in another way. We form the following partial cross sections for every pair transition amplitudes T_j and T_k:

$$\text{for } j=k: \quad \sigma_{jj} = C \sum |T_j|^2 \tag{A.2}$$

$$\text{for } j<k: \quad \sigma_{jk} = C \sum |T_j+T_k|^2 - \sigma_{jj} - \sigma_{kk} \tag{A.3}$$

$$\text{for } j>k: \quad \sigma_{jk} = C \sum |T_j+iT_k|^2 - \sigma_{jj} - \sigma_{kk} \tag{A.4}$$

where we use the same sum and factor C as in eq. (3.12). The last partial cross section can be omitted if we deal with real weights only in eq. (A.1), (b_j=0). The cross section can now be expressed as:

$$\sigma = \sum_{j=1}^{n} \sum_{k=1}^{n} g_{jk}\, \sigma_{jk} \tag{A.5}$$

with weights

$$\left.\begin{aligned} &\text{for } j\leq k: \quad g_{jk} = a_j a_k + b_j b_k \\ &\text{for } j>k: \quad g_{jk} = a_j b_k - a_k b_j \end{aligned}\right. \tag{A.6}$$

The same formulae hold for the derivation of the analysing power if we replace σ by Aσ, using

$$\text{for } j=k: \quad A_{jj}\, \sigma_{jj} = C \sum (-)^{\frac{1}{2}-m_i}\, |T_j|^2 \tag{A.7}$$

and so on. The same weights are used to calculate A:

$$A = \sum_{j=1}^{n} \sum_{k=1}^{n} g_{jk} \sigma_{jk} A_{jk}/\sigma \tag{A.8}$$

So in the analyses the partial angular distributions had to be calculated only once, which saved a lot of computing time.

CHAPTER 4 EXPERIMENTAL RESULTS AND COLLECTIVE MODEL ANALYSIS

4.1 Introduction

In this chapter we present the experimental results and the collective model analysis of the scattering of polarized protons from a series of nuclides. The following nuclides have been investigated: ^{60,64}Ni, ^{86,88}Sr, ^{110,112,114}Cd, ^{115}In and ^{116,118,120,122,124}Sn. Some of these nuclei have a single closed shell, while the others have a closed shell minus one or two nucleons. An aim of our investigation was to detect a possible effect of shell-closing on the analysing power. Since this investigation is a part of a larger research program of scattering of polarized protons around an energy of 20 MeV, we used in nearly all cases a bombarding energy of 20.4 MeV (Hal75, Hal77, Hal80, Mel78, Mel82, Was80).

For the Sr isotopes we have chosen an energy of 24.6 MeV since we wanted to compare our results with the high-resolution experiment of scattering of unpolarized protons of Kaptein (Kap78). An additional measurement on ^{120}Sn at 24.6 MeV has been performed for comparison with the results of Beer.

The experimental angular distributions of the cross sections and analysing powers were analyzed with standard optical model and collective DWBA techniques. Some basic formulae, used in these calculations have already been discussed in chapter 3. Preliminar results have been reported at the Santa Fé conference (Hal80, Was80). In the next section of this chapter we discuss the optical model analysis, while in the third section we pay attention to the DWBA analyses and CC analyses of the inelastic scattering.

4.2 Optical model analysis

In order to fit the elastic scattering and to find a good set of optical model parameters for use in the DWBA and CC calculations, a search procedure was applied, wherein the parameters of the optical model potential, as defined in section 3.2, were varied. The sum of the chi squared values of the fits to the cross section and analysing power was minimized.

For all optical model calculations we used the program OPTIMO (Vos72). In addition, in the case of ^{60}Ni we have done a limited search with the CC code ECIS (Ray72), since in that nucleus the first excited state is rather strongly coupled to the ground state.

As a consequence of the uncertainties in the normalizations of the separate runs and of the diverse detectors we estimate the minimal relative errors of the elastic cross sections to be 2% and the minimal absolute errors of the analysing powers to be 1%. In general the statistical errors were less for the elastic scattering. These errors give about equal chi squared values for the cross section and analysing power in the minimization procedure.

4.2.1 Standard deviations of the parameters

Special attention was payed to the standard deviations of the parameters, calculated following eqs. (3.2a) and (3.2b). At the bottom of tables 4.1a and 4.2a we have given the averaged values of the standard deviations for all fits, since the separate fits gave nearly equal values. If these errors remained too large the fitting process was continued with a smaller stepsize. We see that the real central radius and strength, r_o and V_o, as well as the imaginary central radius, r_i, are the best determined parameters, while the volume absorption W_v is more uncertain. Sometimes we have fixed W_v in the search analysis at the standard value of Becchetti and Greenlees (Bec69). In the literature often W_v is taken 0.

Due to the inclusion of the analysing power data in the fit, the spin-orbit parameters are rather well defined. The absolute errors in the optical model parameters are found by taking the product $\Delta p(\chi^2/N_f)^{\frac{1}{2}}$

4.2.2 Normalization

Since we did not perform an absolute measurement of the cross section, we normalized the experimental elastic cross section to the optical model value. Our normalization procedure has been described in section 3.2. For equivalent sets of optical model parameters, for example the best fit, the ultimate normalization for the diverse targets did not differ much, less than 5%, when we accounted for the specific thicknesses. So these free normalizations are reliable and can be used for the normalization of the cross sections of the inelastic scattering.

For different sets of optical model parameters the resulting normalizations can be quite different: e.g. for the experiment on ^{120}Sn at 24.6 MeV, we found with the geometrical parameters of Beer (Bee70) a normalization that was a factor of 1.24 larger than the normalization found with our GF parameters of section 4.2.4 (see fig. 4.6). This normalization also effects the deformation parameters of the inelastic scattering (section 4.3). The normalization of the DWBA curve, however, is again influenced by the optical model parameters but in opposite way. So the deformation parameters are more or less independent from the optical model parameters. For the above mentioned experiment on ^{120}Sn we found for both sets of optical model parameters the same deformation parameters as listed in table 4.7 for 20 MeV.

As a check we have also varied the normalization of the analysing power in some cases. This normalization stayed near the value of 1.0, so the value of the experimental beam polarization (see section 2.4.1) was deduced correctly.

4.2.3 Best fits (BF)

Starting with the potential parameters of Becchetti and Greenlees (Bec69), BG, we fitted the elastic scattering for each nucleus separately. These fits, wherein all parameters were allowed to vary are called the best fits and the corresponding parameter sets are denoted by BF. The parameters of BG gave already quite good fits, but the chi squared values of the best fits are about a factor four smaller. We have reanalyzed the data of ^{58,62}Ni of Melssen (Mel78) in the way as outlined above. The different normalization procedure only caused some small differences in the parameters. Table 4.1a lists the BF parameters for all 20 MeV experiments, table 4.2a the results for the 24 MeV experiment on Sr. From the tables 4.1b and 4.2b we learn that the chi squared values of the cross sections and analysing powers are of the same order of magnitude. So in the minimalization process the cross section and the analysing power have a comparable weight. We also give here the chi squared values per degree of freedom.

Table 4.1a Best fit optical model parameters, at 20.4 MeV.

A	V_o (MeV)	r_o (fm)	a_o (fm)	W_v (MeV)	W_D (MeV)	r_i (fm)	a_i (fm)	V_{so} (MeV)	r_{so} (fm)	a_{so} (fm)
Ni										
58$^{a)}$	49.52	1.200	0.753	1.70	8.46	1.363	0.408	4.93	1.062	0.433
60	53.29	1.173	0.747	1.45	9.41	1.308	0.476	5.74	1.031	0.574
62$^{a)}$	50.38	1.205	0.742	1.38	10.18	1.289	0.486	5.38	1.046	0.510
64	55.33	1.148	0.714	0.63	8.26	1.264	0.651	6.17	0.946	0.634
Cd										
110	52.12	1.213	0.691	0.63$^{b)}$	9.78	1.210	0.700	6.26	1.128	0.571
112	53.21	1.200	0.688	0.63$^{b)}$	9.36	1.194	0.760	6.11	1.110	0.582
114	54.38	1.181	0.732	0.63$^{b)}$	9.70	1.183	0.811	6.09	1.097	0.569
In										
115	54.33	1.176	0.697	2.21	8.60	1.278	0.667	6.05	0.854	0.647
Sn										
116	53.71	1.194	0.713	1.25	8.85	1.265	0.675	5.59	1.060	0.566
118	55.08	1.180	0.714	1.65	8.40	1.266	0.700	5.63	1.022	0.645
120	55.63	1.169	0.749	2.02	8.70	1.278	0.690	5.65	1.000	0.670
122	55.74	1.166	0.740	0.43	10.23	1.255	0.739	5.76	0.984	0.700
124	55.98	1.161	0.755	0.46	10.74	1.258	0.726	5.64	0.921	0.764
(%)$^{c)}$	(0.3)	(0.2)	(0.5)	(13)	(5)	(0.3)	(1.1)	(0.9)	(1.0)	(2.6)

The Coulomb radius parameter is fixed at 1.25 fm.

a) from Melssen (Mel78), reanalysed.

b) fixed value.

c) (%) are the standard deviations of the varied parameters in per cent, averaged for all isotopes.

Table 4.1b Volume integrals, rms radii and chi squared values for the best optical model fits at 20.4 MeV (BF).

A	J_o/A	J_i/A	$J_{so}/A^{\frac{1}{3}}$	$\langle R_o^2\rangle^{\frac{1}{2}}$	$\langle R_i^2\rangle^{\frac{1}{2}}$	$\langle R_{so}^2\rangle^{\frac{1}{2}}$	σ_R b)	χ_σ^2	χ_A^2	χ^2/N_f c)
	(	MeV fm^3	)							
Ni										
58 a)	451.9	104.1	131.5	4.5609	5.3327	4.3300	1074	624	601	23.56
60	454.6	116.0	148.7	4.5132	5.3409	4.4203	1113	874	385	24.21
62 a)	457.5	121.1	141.4	4.6108	5.3549	4.4398	1159	343	506	16.98
64	434.5	118.1	146.6	4.3474	5.6116	4.2739	1208	748	202	18.26
Cd										
110	443.7	115.5	177.2	5.1819	6.3973	5.6939	1385	303	280	11.23
112	438.8	117.0	170.2	5.1583	6.4697	5.6533	1433	342	234	11.06
114	436.1	127.0	167.8	5.2045	6.5581	5.6096	1529	255	175	8.95
In										
115	424.1	122.0	129.8	5.1310	6.5554	4.2625	1425	602	517	21.95
Sn										
116	440.1	114.1	148.8	5.2332	6.6174	5.4669	1417	231	197	9.96
118	436.0	116.5	144.5	5.2093	6.6568	5.4065	1452	222	178	8.51
120	434.4	123.7	141.9	5.2639	6.6940	5.3626	1503	605	184	14.61
122	430.2	130.4	142.4	5.2575	6.8658	5.3516	1552	349	205	11.81
124	428.0	134.2	130.5	5.2880	6.8842	5.1792	1571	350	218	12.07

a) from Melssen (Mel78), reanalyzed.

b) σ_R = reaction cross section.

c) N_f = the number of degrees of freedom.

Table 4.2a Best fit optical model parameters for Sr at 24.6 MeV.

A	V_o (MeV)	r_o (fm)	a_o (fm)	W_v (MeV)	W_D (MeV)	r_i (fm)	a_i (fm)	V_{so} (MeV)	r_{so} (fm)	a_{so} (fm)
86	52.54	1.167	0.756	2.65$^{c)}$	7.15	1.277	0.675	5.73	1.020	0.604
88	52.54	1.163	0.761	2.65$^{c)}$	7.00	1.309	0.654	6.03	0.979	0.716
(%)	(0.3)	(0.2)	(0.5)		(0.5)	(0.2)	(0.8)	(0.9)	(0.6)	(1.3)
88$^{a)}$	51.65	1.17	0.725	0$^{c)}$	8.99	1.266	0.673	6.49	1.01	0.75
88$^{b)}$	52.51	1.17	0.725	0$^{c)}$	9.52	1.266	0.673	5.56	1.01	0.75

a) Set P_2 of Kaptein, unvaried.
b) Set P_2 of Kaptein, with V_o, W_D and V_{so} varied.
c) Fixed value.

Table 4.2b Derived and chi squared values for the best optical model fit of Sr at 24.6 MeV.

A	J_o/A	J_i/A	$J_{so}/A^{\frac{1}{3}}$	$\langle R_o^2\rangle^{\frac{1}{2}}$	$\langle R_i^2\rangle^{\frac{1}{2}}$	$\langle R_{so}^2\rangle^{\frac{1}{2}}$	σ_R	χ_σ^2	χ_A^2	χ^2/N_f
	(	MeV fm^3	)	(fm)	(fm)	(fm)	(mb)			
86	424.1	120.4	146.8	4.8801	6.0157	4.8840	1427	823	851	33.47
88	419.8	120.2	148.2	4.9033	6.1208	4.8975	1452	543	761	26.06

Table 4.2c Chi squared values for diverse optical model fits to ^{88}Sr.

reference		fit	remark	χ_σ^2	χ_A^2	χ^2/N_f
Kaptein	(Kap78)	start	a)	3601	4469	144
		3V	b)	1468	1458	52
BG	(Bec69)	start	c)	4561	982	99
		3V	d)	1834	1720	64
Best fit				543	761	26

a) Set P_2, no parameters varied.
b) Set P_2, V_o, W_D and V_{so} varied.
c) No parameters varied.
d) V_o, W_D and V_{so} varied.

In table 4.2c we compared the optical model parameters found by Kaptein (Kap78) with our results for ^{88}Sr at 24.6 MeV. His set P2 gives chi squared values, both for the cross section and analysing power, that are a factor of 7 larger than our BF result. Probably this comes from the fact that Kaptein fitted experimental cross sections till an angle of 120 degrees instead of 165 degrees. Also no analysing powers were fitted by Kaptein.

The set optical model parameters deduced by Beer (Bee70), who also performed experiments with (unpolarized) protons of 24.5 MeV, scattered by the same sequence of Sn isotopes as we have used, gives rather bad descriptions of our experiments. The same arguments as mentioned above can be applied here.

In the analysis of the experimental results obtained at 24.6 MeV on ^{120}Sn we found the same effect: using the geometrical parameters of Beer instead of the GF parameters of our 20.4 fit (see section 4.2.4) we obtained chi squared values that were a factor of 4 larger, as can be seen in tables 4.3a and 4.3b.

Table 4.3a Fixed geometry optical model parameters for ^{120}Sn at 24.6 MeV. V_o, W_D and V_{so} were varied.

	V_o (MeV)	r_o (fm)	a_o (fm)	W_V (MeV)	W_D (MeV)	r_i (fm)	a_i (fm)	V_{so} (MeV)	r_{so} (fm)	a_{so} (fm)
GF[a]	53.33	1.178	0.730	2.17	8.63	1.266	0.695	6.36	0.970	0.699
Beer[b]	56.39	1.130	0.744	0.00	10.62	1.330	0.650	6.47	1.130	0.750
(%)	(0.09)				(0.6)			(1.1)		

a) Geometry of the global fit of Sn.

b) Geometry of Beer (Bee70).

Table 4.3b Derived and chi squared values for the fixed geometry optical model fit of ^{120}Sn at 24.6 MeV.

GF[a]	422.0	122.8	154.7	5.2545	6.6390	5.2617	1594	178	156	8.32
Beer[b]	400.8	128.5	183.6	5.1271	7.0675	6.0510	1606	735	392	28.16

a) Geometry of the global fit of Sn.

b) Geometry of Beer (Bee70).

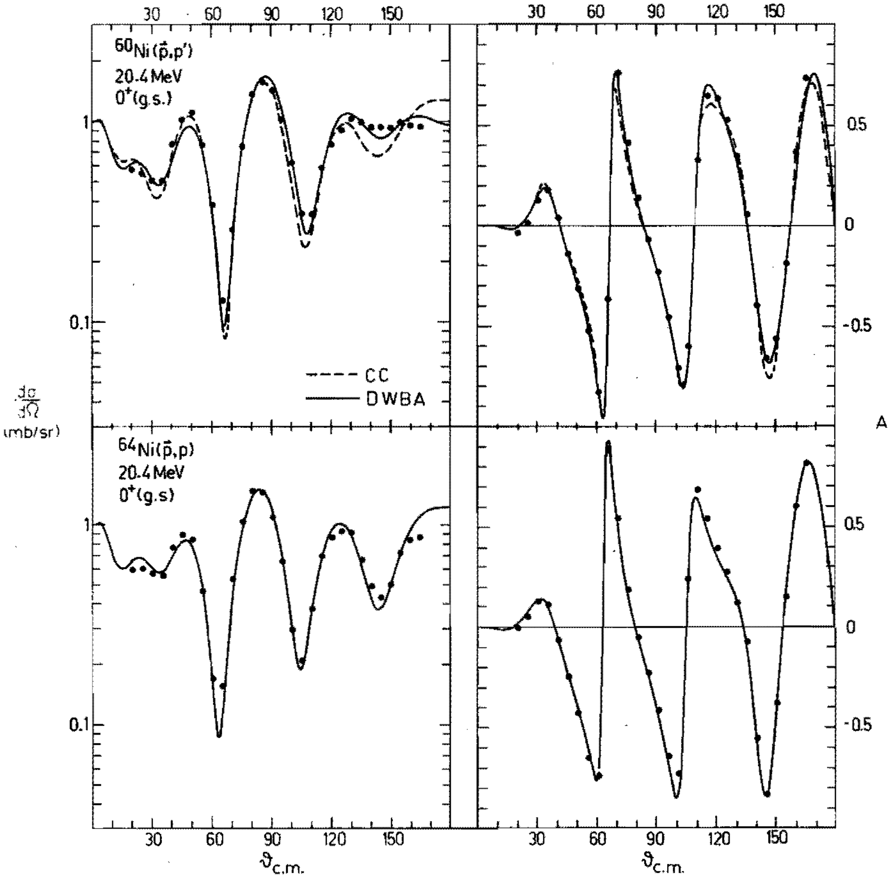

Fig. 4.1 Differential cross section and analysing power for elastic scattering of protons by $^{60,64}Ni$ at 20.4 MeV.
The curves are calculated with the optical model, using the BF parameters.
For ^{60}Ni the dashed curve is calculated with the CC parameters.
The error bars, if not smaller than the dots, indicate the statistical errors.

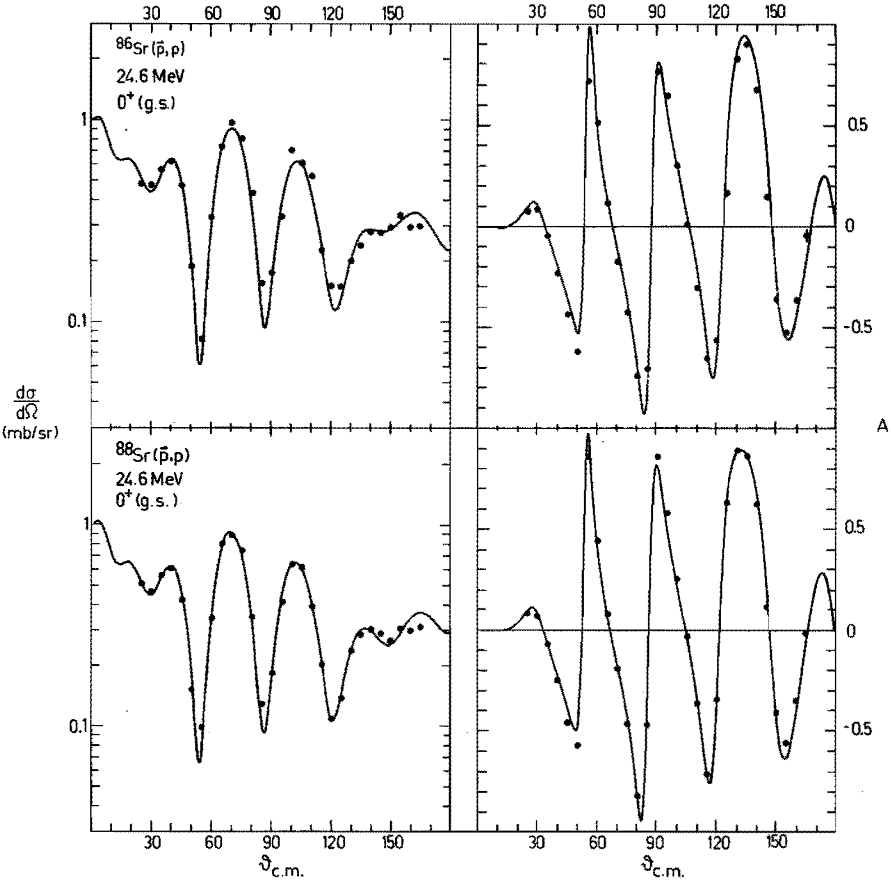

Fig. 4.2 Differential cross section and analysing power for elastic scattering of protons by ^{86,88}Sr at 24.6 MeV. The curves are calculated with the optical model, using the BF parameters.

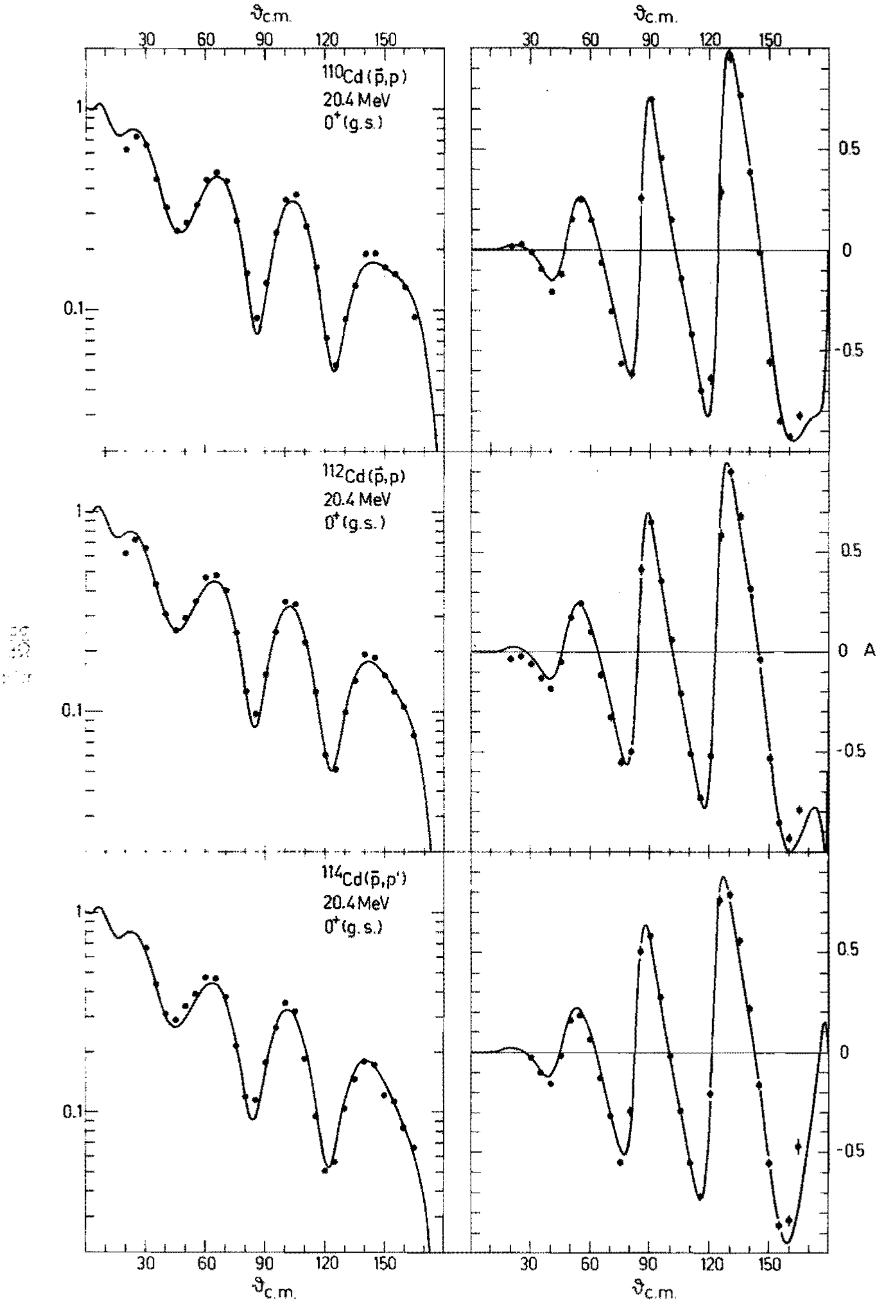

Fig. 4.3 Differential cross section and analysing power for elastic scattering of protons by ^{110,112,114}Cd at 20.4 MeV. The curves are calculated with the optical model, using the BF parameter.

The experimental results and the BF curves are drawn in figs. 4.1 for Ni, 4.2 for Sr and 4.3 for Cd. The curve of ^{115}In in fig. 4.4 resulted from a search wherein the geometrical optical model parameters were fixed to the values of the GF set of Sn, which set is described in the next section, while the three strength parameters V_o, W_d and V_{so} were varied.

Reviewing the results we can conclude that the optical model describes the experimental angular distribution very well.

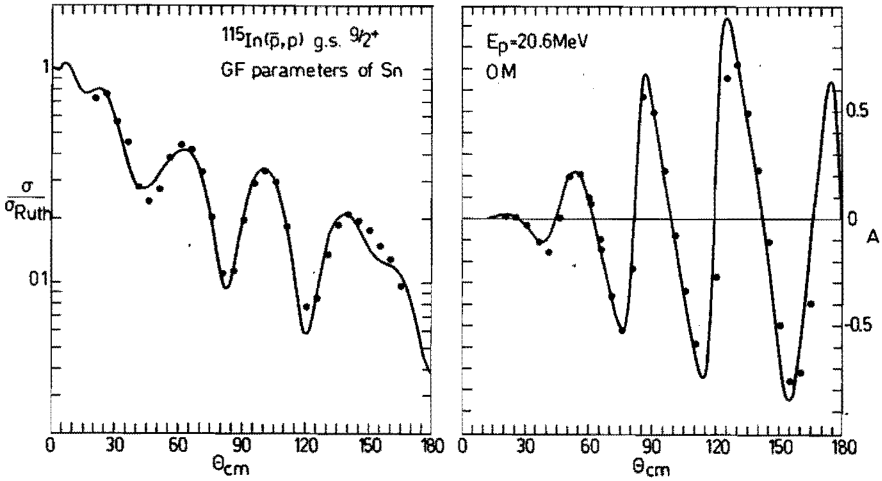

*Fig. 4.4 Differential cross section and analysing power for elastic scattering of protons by ^{115}In at 20.4 MeV.
The curves are calculated with the optical model, using for the geometry the GF parameters of Sn, the strengths were varied.*

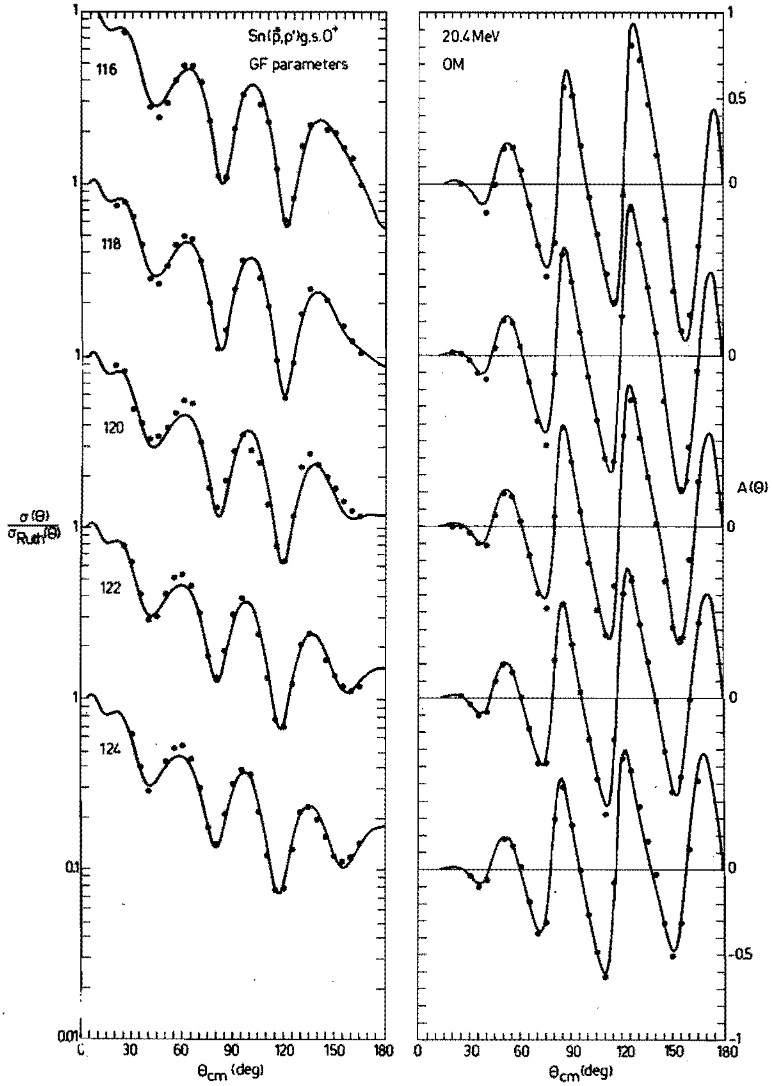

Fig. 4.5 Differential cross section and analysing power for elastic scattering of protons by ^{116,118,120,122,124}Sn at 20.4 MeV. The curves are calculated with the optical model, using the GF parameters.

4.2.4 Global Fits (GF)

For the Ni, Cd and Sn isotopes we also have performed a global optical model search, called GF, which means that we fitted all angular distributions of a series of isotopes with one set isospin dependent parameters. As starting values we took the averages of the BF parameters. In fig. 4.5 we show the results of the GF fits for the Sn isotopes. Visual inspection hardly shows any difference between the BF and GF curve, so here only the GF curves are displayed.

In the GF search we tried various isospin, (N-Z)/A, dependences of the strength and diffuseness parameters. It turned out that only the surface absorption parameter W_D had a noticeable isospin dependence. All other parameters were thus equal for each isotope in a sequence.

Table 4.4a lists the GF parameters, which are very well determined (small standard deviations), since a large amount of data points is fitted simultaneously. The best GF set is that of Sn, which differs only a little from the average of the individual best fits. Compare also the values of χ^2/N_f in tables 4.1b and 4.5a. In the case of Ni we better use the BF parameters in the DWBA calculations, but for the Sn and Cd isotopes the BF and GF parameters are nearly equal. So here for the analyses of the inelastic scattering the GF set is preferable.

In order to check the fitting procedure we repeated the BF searches starting with the GF sets. The same parameters as in table 4.1a were found.

Since we have a well defined data-set for Sn we also could investigate the influence of the addition of extra optical model parameters. Sinha (Sin75) suggested a real central surface term. In our analysis this term, however, turned out to be small with a large standard deviation. Also the addition of an imaginary spin-orbit term did not improve the fits. So these extra terms are not necessary for the optical model analysis of our experimental data.

4.2.5 Volume integrals and root mean square radii

It is known that in a certain mass region the volume integrals and rms radii show less variation than the individual optical model

Table 4.4a Global fit optical model parameters at 20.4 MeV (GF).

V_o (MeV)	r_o (fm)	a_o (fm)	W_V (MeV)	W_{D0} (MeV)	W_{D1} (MeV)	r_i (fm)	a_i (fm)	V_{so} (MeV)	r_{so} (fm)	a_{so} (fm)
Ni$^{b)}$										
52.47	1.176	0.745	1.30$^{a)}$	7.24	21.8	1.302	0.518	5.64	1.023	0.554
Cd$^{c)}$										
52.97	1.201	0.700	0.63$^{a)}$	5.55	27.7	1.192	0.759	6.12	1.108	0.585
Sn$^{d)}$										
54.97	1.178	0.730	1.20$^{a)}$	5.93	21.1	1.266	0.695	5.65	0.970	0.699
(0.2)	(0.08)	(0.2)		(1.7)	(3.0)	(0.3)	(0.7)	(0.4)	(0.5)	(0.8)

a) Fixed value.
b) $\chi^2/N_f = 30.77$.
c) $\chi^2/N_f = 10.81$.
d) $\chi^2/N_f = 13.53$.

Table 4.4b Theoretical and experimental values of the volume integrals and rms radii from literature compared with our results; the units are in MeV·fm³ and fm, respectively.

reference		J_o	$<R_o^2>^{\frac{1}{2}}$	J_i	$<R_i^2>^{\frac{1}{2}}$	J_{so}	$<R_{so}^2>^{\frac{1}{2}}$
Brieva$^{a)}$	(Bri77)	436	5.23	73	6.2	107	5.30
Greenlees$^{b)}$	(Gre68)	436	5.25	-	-	-	-
Agrawell	(Agr75)	-	-	115	-	-	-
BG	(Bec69)	434	5.27	122	6.79	138	5.51
our exp.	^{120}Sn BF	434	5.26	124	6.69	141	5.36
	^{120}Sn GF	435	5.25	123	6.73	138	5.26

a) Average of the values for ^{40}Ca and ^{208}Pb, at E_p = 21 MeV.
b) Averaged values for ^{120}Sn, 20 MeV.

parameters. We learn from tables 4.1b, 4.2b that those quantities indeed have this property.

First we compare our data with other experimental values from the literature. For ^{120}Sn at 20 MeV the average value of the real volume integral is equal to the average value given by Greenlees, Pyle and Tang (Gre68), see table 4.4b. Using the BG optical model potential we find a somewhat smaller value. The imaginary volume integeal J_i/A is slightly A-dependent for a sequence of isotopes, see table 4.1b, but remains in the interval of 115±15 MeV fm^3, which was quoted by Agrawell and Sood (Agr75) and by Hodgson (Hod76).

Second we compare our results with theoretical values. Brieva and Rook (Bri78) have deduced theoretically the optical model potential in a microscopic way from the effective nucleon-nucleon interaction folded with the nuclear density. The averages of the real central volume integrals and rms radii of Cd and Pb, at 21 MeV compared with our values of BF and GF for ^{120}Sn are in excellent agreement, as can be seen in table 4.4b. Also the real spin-orbit values agree satisfactorily. Since Brieva and Rook used an imaginary spin-orbit term and we not, the imaginary values are not comparable.

4.2.6 Isospin dependence of optical model parameters

The isospin dependence of the optical model parameters and of the corresponding volume integrals is of interest for they give information about the difference between proton and neutron interactions (Gre68, Sat69, Fin80). In this section we will discuss the isospin dependence of some optical model parameters of the Sn isotopes. For our definition of the optical model parameters and for proton scattering (τ=+1) we can split the real central strength as follows:

$$V_o \doteq V_{oo} + \tau\ (N-Z)/A\ V_{o1}$$

For neutron scattering we use τ=-1. In the same way other terms can be split, like W_D, J_o etc.

Since in the BF calculations geometrical as well as strength parameters were varied, these fits are not used for the investigation of the isospin dependence. We performed separate searches for the five Sn isotopes, wherein the three strength parameters V_o, W_D and V_{so} were varied while the geometry was fixed on the GF values. We

Table 4.5a Isospin dependences of the central potential for $^{116-124}$Sn.

projectile	energy (MeV)	reference	remark	V_{o1} (MeV)	W_{D1} (MeV)
p	20	FG3	a)	-3.9(4.4)$^{e)}$	21(1)$^{e)}$
p	20	GF5	b)	-3.1(1.1)	23(3)
p	24	(Bee70)	d)	26.2(5.1)	15(6)
p	16	(Mak68)	c)	20.2(2.0)	20(8)
n	11	(Fin80)		15.6(2.3)	12(2)
p	global	(Bec69)		24.0	12

All real central potentials are corrected for the Coulomb potential by a factor 0.4 $Z/A^{1/3}$, which lowers the value of V_{o1} by 1.5 MeV.

a) Search with the Fixed Geometry from the global fit, table 4.3, and the three strength parameters varied.

b) Global fit like in section 4.2.4 but now the geometry is fixed as for FG3 and the parameters V_{o0}, V_{o1}, W_{D0}, W_{D1} and V_{so} are varied. The errors here are from the optical model fit, section 4.2.1.

c) Without the values for ^{112}Sn, when ^{112}Sn is included then V_{o1}= 16 MeV.

d) From table 2 of Beer with W_s = 0.

e) Between parentheses the standard deviations of the linear regression fit, except for FG3.

Table 4.5b Isospin dependence of the volume integrals (in MeV fm^3) calculated for the global fit and best fit potentials

isotope	fit	J_{o0}/A	J_{o1}/A	J_{i0}/A	J_{i1}/A	$J_{so0}/A^{\frac{1}{3}}$	$J_{so1}/A^{\frac{1}{3}}$
Ni	GF	454	-66	100	212	145	0
Cd	GF	446	-43	85	231	170	0
	BF	478	-278	-	-	232	-426
Sn	GF	443	-46	91	195	138	0
	BF	469	-210	61	377	187	-275

also performed a global fit, like in section 4.2.4, with as parameters V_{oo}, V_{o1}, W_{Do}, W_{D1} and V_{so}, but now also with the geometry fixed to the previous GF values.

The resulting isospin dependences, together with values from the literature are compiled in table 4.5a. Surprisingly, a small negative value of V_{o1} is found in both cases while in the literature a positive value of around 20 MeV is given. The values of Beer (Bee70) and those of Makofske (Mak68), however, have been deduced by fitting the cross section in a smaller angular range as we have used, while Becchetti and Greenlees (Bec69) have fitted a very large range of nuclei in a general global fit.

The imaginary isospin dependence, W_{D1}, has a value that is in accordance with the results of Beer and those of Makofske but is higher than the value of Finlay (Fin80) and Becchetti. Also here the differences can be caused by different fitting methods and data regions.

4.2.7 Isospin dependence of volume integrals and rms radii

We investigated also the isospin dependences of the volume integrals of the Ni, Cd and Sn isotopes. As data for the linear least squares fit we used the values listed in table 4.1b. The results are listed in table 4.5b. For comparison we also give in the same table the isospin dependences using the GF parameters. We see that for the BF the isospin contribution J_{o1} is much larger than for the GF. Further we observe for all isotopes similar dependences: decreasing for the real central and spin-orbit volume integrals but increasing for the imaginary volume integral.

In conclusion we can say that the inclusion of analysing power data does not remove the isospin dependences of the volume integrals, but that those dependencies strongly depend on the used search method.

4.2.8 Coupled channels fit for ^{60}Ni

For ^{60}Ni we performed in addition to the optical model fit, a search with the coupled channel code ECIS (Ray72). We fitted the ground state and the 2_1^+ state simultaneously. Nine optical model parameters and the deformation parameter were varied. As can be seen

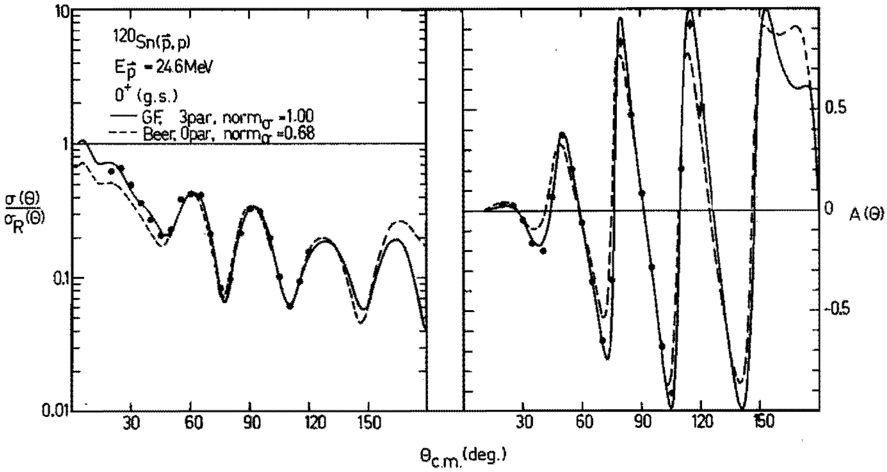

Fig. 4.6 Differential cross section and analysing power for elastic scattering of protons by ^{120}Sn at 24.6 MeV. The curves are calculated with the optical model, using the geometry of the GF parameters of Sn, full line, and of Beer, dashed line.

Table 4.6 Optical model and deformation parameters deduced from a CC fit to the ground state and the 2_1^+ state of ^{60}Ni, with the code ECIS. For comparison also the best fit (BF) and DWBA data are given.

fit	V_o (MeV)	r_o (fm)	a_o (fm)	W_v (MeV)	W_D (MeV)	r_i (fm)	a_i (fm)	V_{so} (MeV)	r_{so} (fm)	a_{so} (fm)
BF	53.3	1.17	0.75	1.45	9.4	1.31	0.48	5.7	1.03	0.57
CC	53.3	1.15	0.75	1.45	6.1	1.35	0.61	5.4	0.97	0.58
(Sd)a)	(7)	(.09)	(.03)		(1.7)	(.03)	(.12)	(0.7)	(.04)	(.12)

fit	β_2	$\chi_\sigma^2(gs)$	$\chi_A^2(gs)$	$\chi_\sigma^2(2_1^+)$	$\chi_A^2(2_1^+)$
BF	0.255	874	385	26654	3484
CC	0.207(0.007)a)	3282	742	4099	799

a) These are the standard deviations of the CC fit.

in fig. 4.6 some differences between the optical model and CC fit exist. For the forward angles of the cross section, the CC fit is better than the optical model fit, but at backward angles the situation is reversed. The analysing powers differ not so much. In table 4.6 we list the parameters found from the CC fit. We see that the chi squared values of the CC fit are larger than for the standard optical model fit. This is caused by the difficulty to fit the slope of the 2_1^+ state which influences here also the fit to the ground state.

In conclusion, we can say that the elastic scattering is described very well by the standard optical model.

4.3 Inelastic scattering and DWBA

In our experiments only the strongest collective transitions produced enough statistics to give reliable angular distributions. Sometimes experimental data points are missing from an angular distribution because of an overlap of the peak of interest with such a large peak, arising from a contamination in the target (^{1}H, ^{12}C, ^{16}O), that a reliable correction was impossible.

For the theoretical analysis of the inelastic scattering data we used the well known standard collective DWBA method (see section 3.4). We used a DWBA code, written by Verhaar and Tolsma (Ver72). In this program a full Thomas spin-orbit form factor was incorporated. The curves of Cd and Sn have been calculated with the GF, all other curves with the BF optical model potentials.

The deformation parameters, listed in table 4.7, are the only free parameters in the DWBA calculations. They were deduced from the scaling of the first maximum, around 30 deg, to the experimental points (in our program PLOT). In general these deformation parameters are quite close to the values from the literature, which are also listed in table 4.7. As consequences of the statistical errors in the experimental points and the normalization procedure for the ground state and the inelastic state, we estimate the errors in the deformation parameters to be about 10%.

We now make some remarks concerning the various nuclides.

Table 4.7 *Deformation parameters.*$^{c)}$

	2_1^+ states			3_1^- states			
A	E_x(MeV)	β	β_{lit}	E_x(MeV)	β	β_{lit}	reference
^{60}Ni	1.33	0.255	0.26	4.42	0.209	0.19	(Mel78)
^{64}Ni	1.34	0.206	0.200	3.56	0.203	0.181	(Car66)
^{86}Sr	1.08	0.158	0.130	2.48	0.185	0.153	(Ram72)
^{88}Sr	1.84	0.114	0.110	2.73	0.177	0.166	(Kap78)
^{115}In	1.13	0.089$^{a)}$		2.13	0.092$^{a)}$		
(L=2	1.29	0.075$^{a)}$		2.46	0.106$^{a)}$		
or 3)	1.48	0.066$^{a)}$					
^{110}Cd	0.66	0.168	0.175	2.08	0.146	0.175	(Mak68)
^{112}Cd	0.62	0.165	0.173	1.97	0.154	0.164	(Mak68)
^{114}Cd	0.59		0.169	1.96	0.145	0.160	(Mak68)
^{116}Sn	1.29	0.151	0.143	2.27	0.164	0.188	(Bee70)
^{118}Sn	1.23	0.138	0.134	2.33	0.158$^{b)}$	0.174	(Bee70)
^{120}Sn	1.17	0.136	0.128	2.41		0.161	(Bee70)
^{122}Sn	1.14	0.127	0.122	2.49	0.141	0.149	(Bee70)
^{124}Sn	1.14	0.109	0.119	2.61	0.123	0.138	(Bee70)

Other states of ^{60}Ni, 2^+ and 4^+:

J (nr)	E_x(MeV)	β	β_{lit}	reference
2 (2)	2.15	0.0303	0.022	(Ino68)
2 (3)	3.12	0.0509	0.06	(Ino68)
4 (1)	2.51	0.127	0.085	(Ino68)
4 (3)	3.67	0.0664	0.045	(Ino68)

5_1^- states of Sn:

A	E_x(MeV)	β	β_{lit}	reference
^{122}Sn	2.24	0.0844	0.0859	(Bee70)
^{124}Sn	2.21	0.0879	0.0886	(Bee70)

a) Does not include the statistical factor $\sqrt{(2J_i+1)(2L+1)/(2J_f+1)}$.

b) After correction for the 5_1^- overlap strength.

c) The estimated errors in our experimental values β are about 10%.

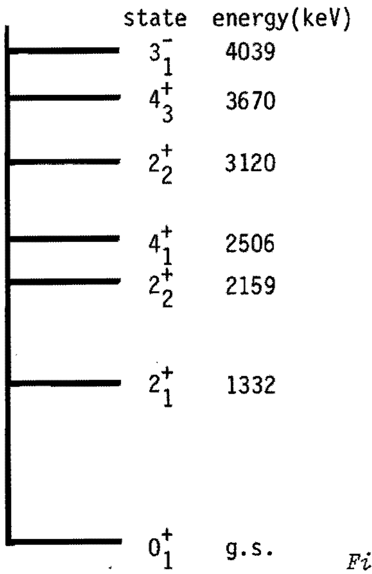

Fig. 4.7a
Analysed states of ^{60}Ni.

Analysed states of ^{60}Ni.

4.3.1 Ni

The Ni isotopes are nuclides of interest because of their closed proton shell, Z=28. The statistics of the measurements on ^{60}Ni were much better than previous results (Hal77). So we could extract data for some of the two-phonon states. In fig. 4.7a the level scheme of the states of ^{60}Ni that we have analysed is displayed. First we will discuss the one-phonon states and in the next sub-section the two-phonon results.

4.3.1.1 One-phonon states of ^{60,64}Ni

In fig. 4.7 we see that the slope of the theoretical cross section of the 2_1^+ state is not as steep as that of the experimental cross section. This phenomenon was already encountered in the work of Melssen (Mel78) on ^{58,60,62}Ni and also in more recent experiments, in our group on ^{64,66,68,70}Zn (Hal80). Only for ^{70}Zn the theoretical and experimental cross sections agreed. The agreement becomes less when going to the lighter Zn isotopes. The same trend holds for the Ni isotopes and the Sn isotopes (fig. 4.17).

Since for ^{60}Ni the 2_1^+ state is rather strongly coupled to the ground state, which is seen from the deformation parameter having a

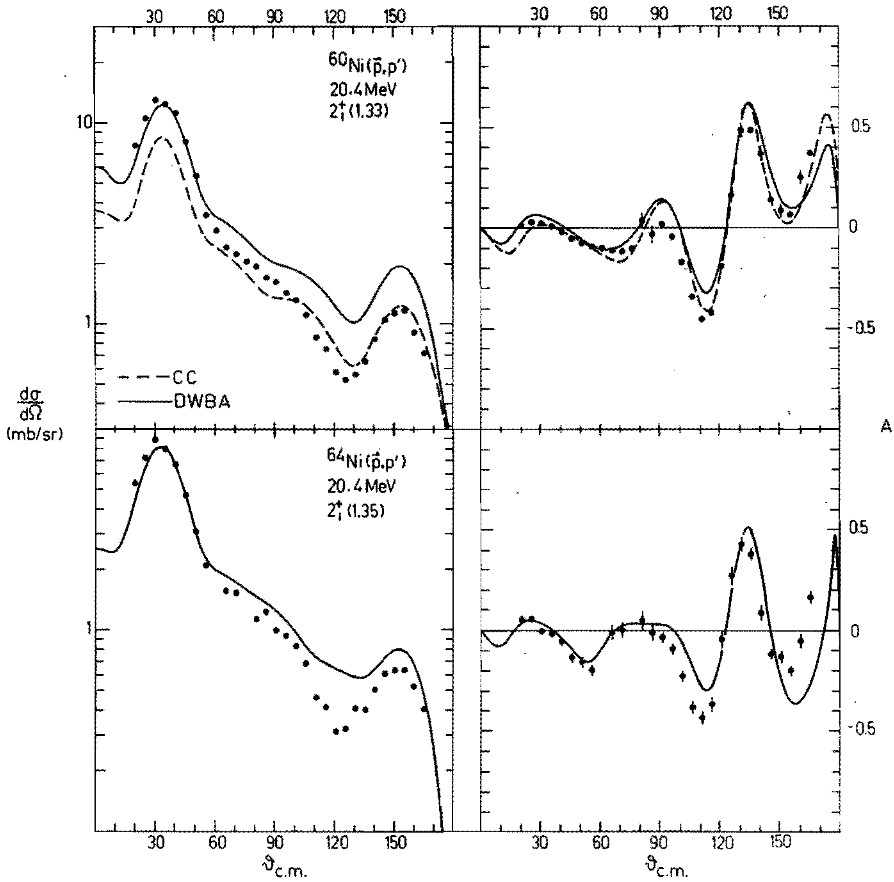

Fig. 4.7 Differential cross section and analysing power for inelastic scattering of protons by ^{60,64}Ni at 20.4 MeV leaving the target in the 2_1^+ state.
The full curves are calculated with the DWBA, using the BF optical model parameters, the dashed curve for ^{60}Ni with the CC method.
The DWBA curve is scaled on the first maximum while the CC curve is scaled on the complete angular distribution.

value of 0.255, we tried to explain this disagreement by performing a CC analysis for ^{60}Ni, in two ways:

a. We used the code CHUCK (Kun69) in a calculation wherein the two-phonon multiplet, 0^+, 2^+, 4^+, around 2.5 MeV was coupled to the 2_1^+ state. Indeed the theoretical cross section is now lower at the backward angles, but it is not lowered enough to give a satisfactory result. See table 4.8a for the various cross sections at the backward angle of 126 degrees.

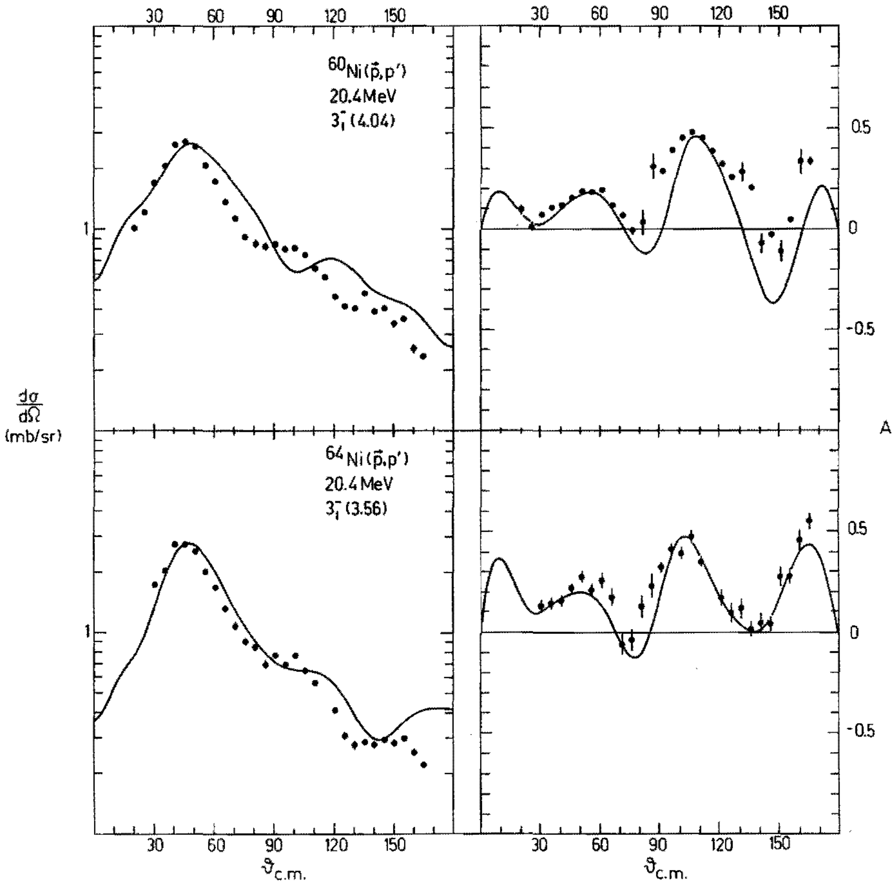

Fig. 4.8 Differential cross section and analysing power for inelastic scattering of protons by ^{60,64}*Ni at 20.4 MeV leaving the target in the* 3_1^- *state.*
The curves are calculated with the DWBA, using the BF optical model parameters.

b. A limited search with the program ECIS (Ray72) was performed. We varied nine optical model parameters together with the deformation parameter β_2, in order to fit the elastic scattering (see section 4.2.8), and the inelastic scattering simultaneously. This gives a better fit of the analysing power of the 2_1^+ state, but its cross section does not change so much, as can be seen in fig. 4.7. The resulting parameters are listed in table 4.6. We notify the value of β_2, which is considerably lower (20%) as that given in table

Table 4.8a Cross section of the 2_1^+ state at θ=126° in mb/sr of ^{60}Ni.
The theoretical curves are normalized at the experimental maximum around 30°.

theoretical values:		
DWBA calculation		1.00
CC with coupling of gs to 2_1^+ and fit of OM parameters;	ECIS	0.86
CC with couplings between gs, 2_1^+ and 0_2^+, 2_2^+ and 4_2^+, no fit;	CHUCK	0.80
experimental value and error		0.52 (0.01)

4.7. This simply comes from the fact that in ECIS the complete inelastic angular distribution is used for the scaling of the theoretical cross section to the experimental points, while in the DWBA calculation we used the angular range around the first maximum only. The cross section at 126 degrees calculated with ECIS is nearly the same as calculated with CHUCK after a renormalization at the first maximum, see also table 4.8a. So the steepness of the 2_1^+ cross section remains a difficulty that cannot be explained by the CC theory.

The 3_1^- states of ^{60}Ni and ^{64}Ni are very well described by the DWBA theory, as is shown in fig. 4.8 and the deduced deformation parameters are in agreement with the values from the literature.

4.3.2.1 Two-phonon states of ^{60}Ni

From our spectra we could extract angular distributions with good statistics for some states which are believed to have (partly) a two-phonon character. Theoretically the 0^+, 2^+ and 4^+ states of the two-quadrupole phonon multiplet should have energies around 2.6 MeV. From the energies and J values of the states of ^{60}Ni, which are given in the Nuclear Data Sheets (Aub79), the most probable candidates for the two-phonon multiplet are the states at 2.15 (2_2^+), 2.28 (0_2^+) and 2.51 (4_1^+) MeV. In fig. 4.7a we display the states that we have analysed. We have found states at 2.15, 2.51, 3.12 and 3.67 MeV, so the 0_2^+ state was not observed in our energy spectra. We could not

Table 4.8b Some 2^+ and 4^+ states of ^{60}Ni fitted with a mixture of one-phonon and two-phonon contributions, calculated with the CC model.

J^π	E_x(MeV)	β^{DWBA}	case[a)]	λ_{1ph}	λ_{2ph}	χ^2_σ	χ^2_A
2^+_2	2.15	0.303	DWBA	1	0	6340	868
			mixed	0.227	0.625	3400	305
			2 ph	0	0.694	3926	441
2^+_3	3.12	0.509	DWBA	1	0	2983	542
			mixed	1.010	-0.232	2511	350
			2 ph	0	1.123	6413	1118
4^+_1	2.51	0.127	DWBA	1	0	40155	1097
			mixed	0.927	0.586	22477	1074
			2 ph	0	1.909	248990	2515
4^+_3	3.67	0.066	DWBA	1	0	4354	1218
			mixed	0.516	-0.243	624	1274
			2 ph	0	1.004	3839	1549

a) Case DWBA is only one-phonon and case 2 ph is a pure two-phonon calculation.

separate the 4^+_2 and the 2^+_3 in our spectra, but in the literature only a small deformation parameter for the 4^+_2 state is given. So we treated this state as a pure 2^+ state.

We analysed these four states with first- and second-order CC using the vibrational model. In the second order approach a mixing of 'direct' or one-phonon and of two-phonon distributions was allowed. We calculated with the code ECIS these contributions separately and also a special mixed case wherein the direct and two-phonon contributions had equal weights.

With these three angular distributions we could not apply the approach as outlined in the appendix of chapter 3. We used our program

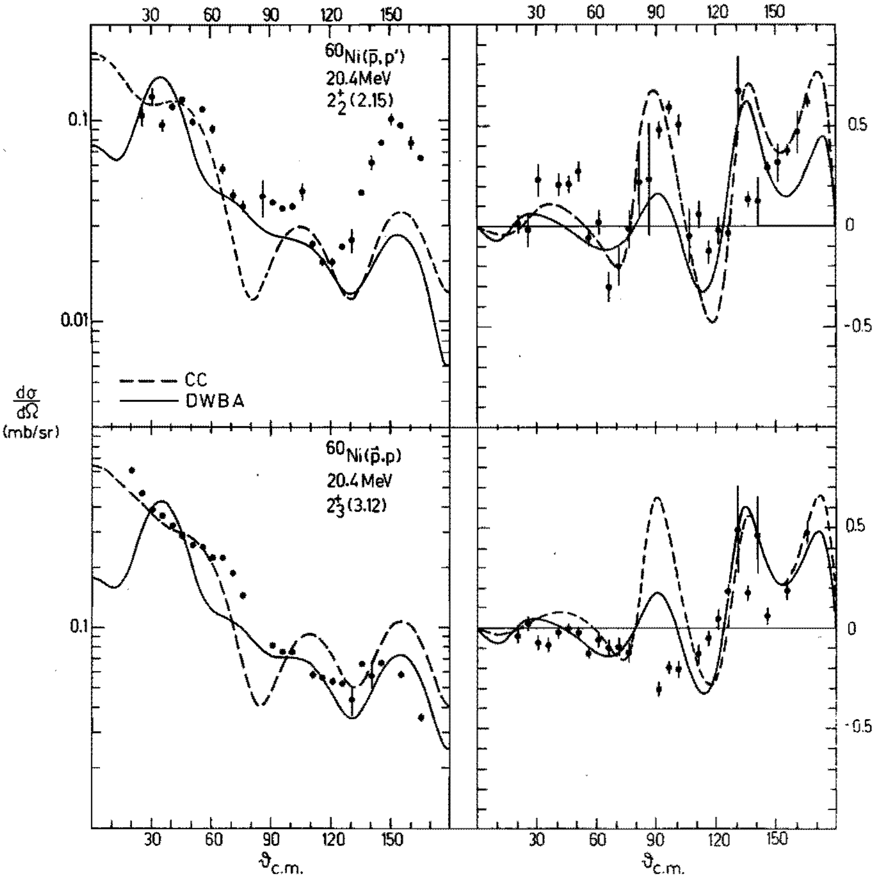

Fig. 4.9 *Differential cross section and analysing power for inelastic scattering of protons by ^{60}Ni at 20.4 MeV leaving the target in the 2_2^+ and 2_3^+ states.*
The curves are calculated with the CC model, with the optimum mixing of one-phonon and two-phonon contributions.

CHIMIX to find the best values of the two strengths. This code searched for a minimal chi squared value for both the cross section and analysing power by varying the strength parameters of the direct and two-phonon contributions.

From the resulting strengths, that are compiled in table 4.8b, we can conclude that the two 2^+ states have a different character. Note in fig. 4.9 especially the differences in the analysing powers. The large maximum at backward angles of the cross section of the

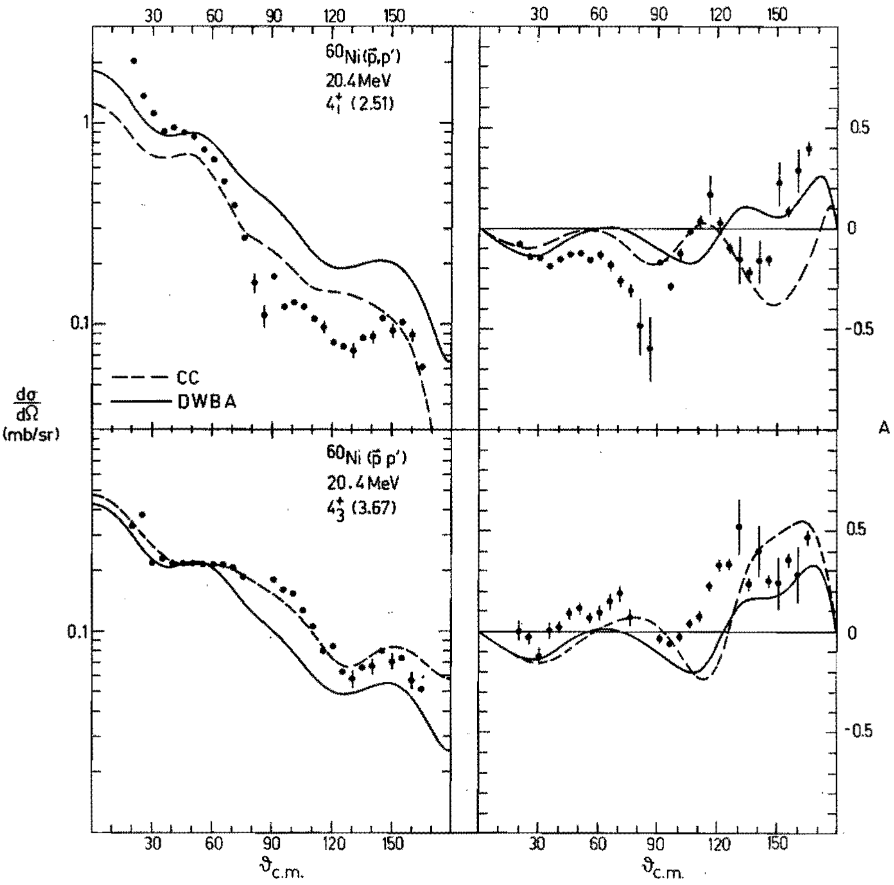

Fig. 4.10 Differential cross section and analysing power for inelastic scattering of protons by ^{60}Ni at 20.4 MeV leaving the target in the 4_1^+ and 4_3^+ states.
The curves are calculated with the CC model, with the optimum mixing of one-phonon and two-phonon contributions.
It should be noted that the scaling of the curve labeled CC of the cross section of the 4_1^+ state has been chosen differently from the other scalings. Here the complete angular distribution has been used for the normalization, while in all other cases the first maximum around 30 degrees has been used.

2_2^+ state cannot be described by the theory. Another difficulty is the rather large positive analysing power around 30 degrees (compare the 2_1^+ state of ^{54}Fe at 20 MeV (Hal77)). So we learn from table 4.8b that the 2_2^+ state has a strong two-phonon contribution, so it belongs to the multiplet. A direct DWBA description gives much larger chi squared values. For the 2_3^+ state the mixed description gives no significant lower chi squared values than the direct approach, while a pure two-phonon description gives very large chi squared values.

Since the theoretical one-phonon and two-phonon angular distributions do not differ much in shape, it is not possible to show clearly with our mixing procedure that the 4_1^+ state belongs to the multiplet and that the 4_3^+ state has a one-phonon character. In fig. 4.10 we see that these two states have quite different angular distributions: the cross section of the 4_1^+ is much steeper than that of the 4_3^+, while the analysing powers have nearly opposite phases. We see that for the 4_3^+ state a relatively small two-phonon contribution added to the direct contribution gives an excellent fit for the cross section. The cross section of the 4_1^+ state, however, is always fitted badly.

We checked the mixing procedure in CHIMIX by performing exact calculations with ECIS for some combinations of the mixing parameters. The differences with the results of CHIMIX were less than 2% for the cross sections and less than 1% for the analysing powers. The angular distributions here are of course not independent, since the various states are coupled indirectly, but these higher order couplings are only weak.

So, in conclusion, we have shown that the 2_2^+ state indeed is nearly a pure two-phonon state, while the 2_3^+ state is predominantly a one-phonon state. The excitation of the 4^+ states seems to have a more complex character.

4.3.2 Sr

The investigation of the nuclide ^{88}Sr is of interest because it has a closed neutron shell (N=50). For comparison we also measured the scattering from ^{86}Sr. The quantity of interest here is the value of the enhancement parameter of the spin-orbit deformation β_{so}, defined as:

$$\lambda = \beta_{so}/\beta_c$$

where β_c is the deformation parameter of the central terms.

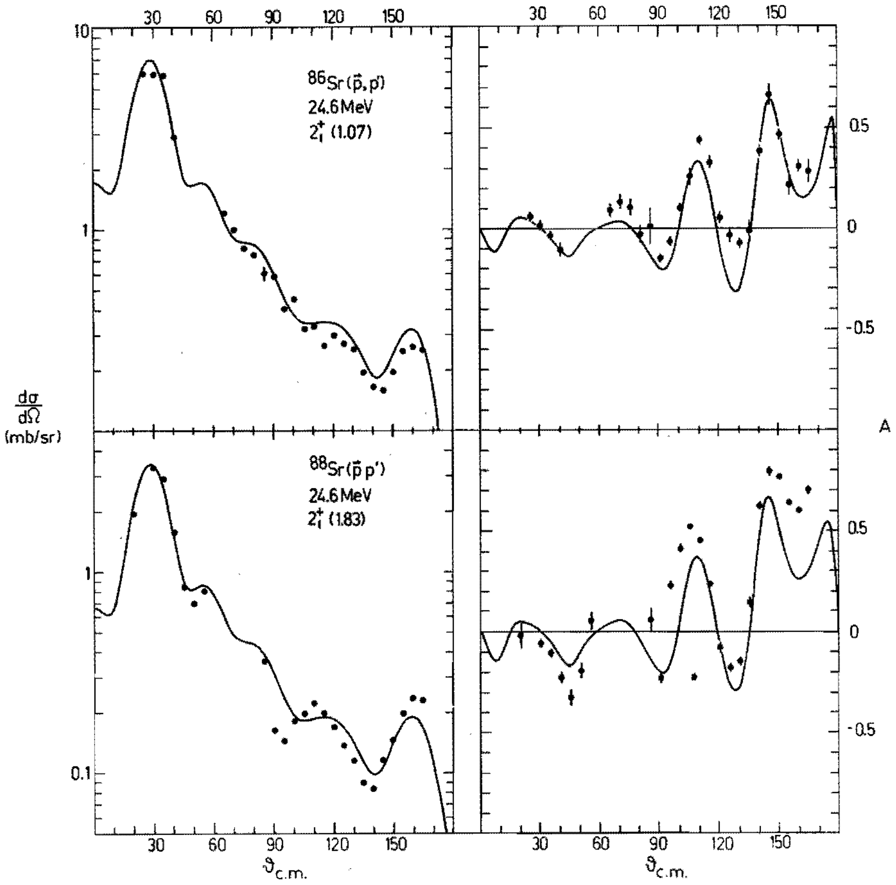

Fig. 4.11 *Differential cross section and analysing power for inelastic scattering of protons by* ^{86,88}*Sr at 24.6 MeV leaving the target in the* 2_1^+ *state.*
The curves are calculated with the DWBA, using the BF optical model parameters.

From the literature (Gla67, Swi78, Swi79, Mel82) we know that other isotopes with N around 50 need an extraordinary large value of λ to describe the analysing power at forward angles of the first 2^+ state. Also for other nuclei with one closed shell this anomaly appears in the scattering of polarized protons in the energy range of 15-25 MeV. One example is ^{54}Fe (Hal77). The results of our experiment and those from the literature are compiled in table 4.9, where we see that λ is energy- and mass-dependent. Also for ^{92}Zr, which nuclide has no

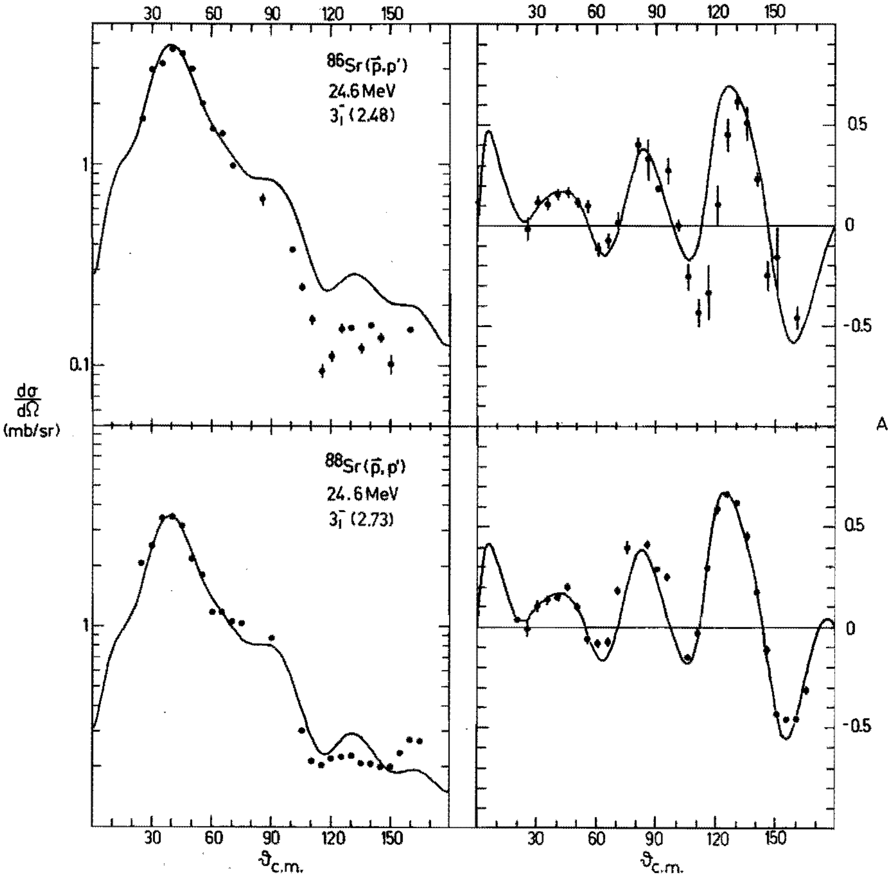

Fig. 4.12 Differential cross section and analysing power for inelastic scattering of protons by ^{86,88}*Sr at 24.6 MeV leaving the target in the* 3_1^- *state.*
The curves are calculated with the DWBA, using the BF optical model parameters.

closed neutron shell but a closed shell plus two neutrons, a large λ value is needed at E_p = 20 MeV. For ^{86,88}Sr, however, at 24.6 MeV proton energy we deduced a normal spin-orbit deformation. In fig. 4.11 we see that the description is quite good. At lower energies, e.g. 17 MeV, possibly a larger enhancement parameter will be needed.

The 3_1^- states of the Sr isotopes are very well described using normal λ values (see fig. 4.12). The deformation parameters are in agreement with the values from the literature.

Table 4.9 Ratio of spin-orbit and central deformations of the 2_1^+ state for nuclei around N=50.

E_p (MeV)	^{86}Sr	^{88}Sr	^{89}Y	^{90}Zr	^{92}Zr	^{92}Mo
20	-	-	2.0$^{a)}$	3.0$^{b)}$	2.5$^{b)}$	1.5$^{c)}$
25	1.0$^{d)}$	1.0$^{d)}$	-	-	-	-
30	-	-	-	1.5$^{c)}$	1.5$^{c)}$	1.5$^{c)}$
40	-	-	-	1.0$^{c)}$	1.0$^{c)}$	-

a) L=2 states of Melssen (Mel82).
b) Glashausser (Gla67).
c) de Swiniarski (Swi77, Swi78, Swi79).
d) this experiment.

4.3.3 Cd

The Cd isotopes have been chosen because they are situated in the neighbourhood of the Sn isotopes. They are well known examples of vibrational nuclei. In Cd, however, the proton shell is not closed, Z=48, and this results in appreciably lower excitation energies for the 2_1^+ and 3_1^- collective states. The experimental cross sections and analysing powers are very well fitted by the DWBA calculations, as can be seen in figs. 4.13 and 4.14.

For ^{114}Cd the 2^+ excitation at forward angles was masked too much by contaminations, so we could not find here a reliable deformation parameter. Compared with the results of Makofske (Mak68), in table 4.7, we see that our deformation parameters are systematically a 7% lower, which can be caused by a different normalization procedure. Makofske, for instance, had only cross sections for angles larger than 30 degrees. The trends, however, are the same.

The 3_1^- states, shown in fig. 4.14 have experimentally more structure than the theoretical curve, especially for the heavier isotopes.

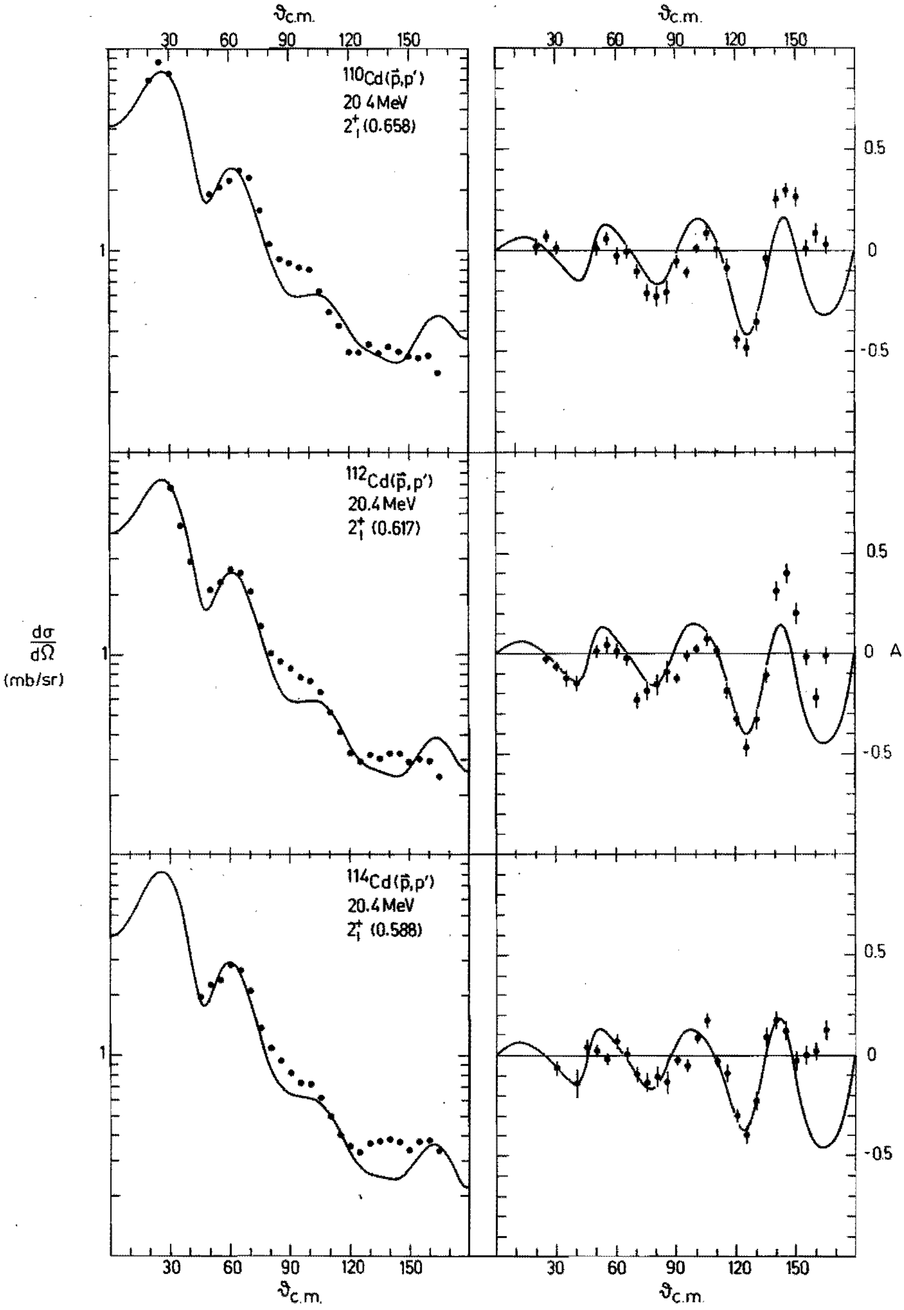

Fig. 4.13 Differential cross section and analysing power for inelastic scattering of protons by ^{110,112,114}Cd at 20.4 MeV leaving the target in the 2_1^+ state.
The curves are calculated with the DWBA, using the GF optical model parameters.

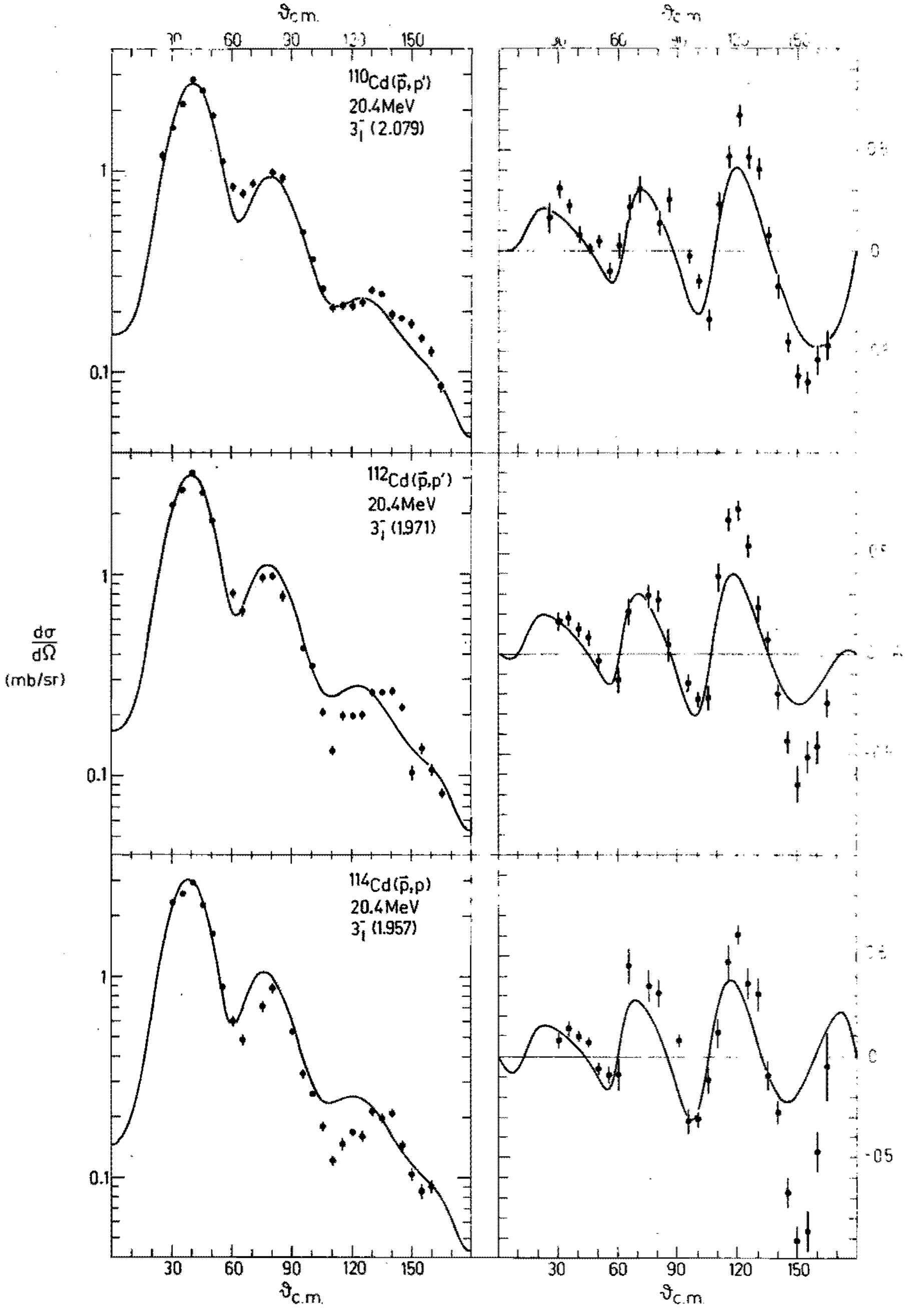

Fig. 4.14 *Differential cross section and analysing power for inelastic scattering of protons by* ^{110,112,114}*Cd at 20.4 MeV leaving the target in the* 3_1^- *state.*
The curves are calculated with the DWBA, using the GF optical model parameters.

4.3.4 ^{115}In

The nuclide ^{115}In has been studied already extensively (Smi76, Smi77), but until now no results of scattering of polarized protons have been published. In first approximation we can consider ^{115}In as nuclide with a closed proton shell. It has only one 1g 9/2 proton hole in the Z=50 shell. So the collective excitations should be described by the weak-coupling model. The proton hole is coupled to the collective phonons of the parent nuclide ^{116}Sn.

According to the weak-coupling model (see section 3.4.2), we expect five L=2 and seven L=3 transitions in ^{115}In, with weighted

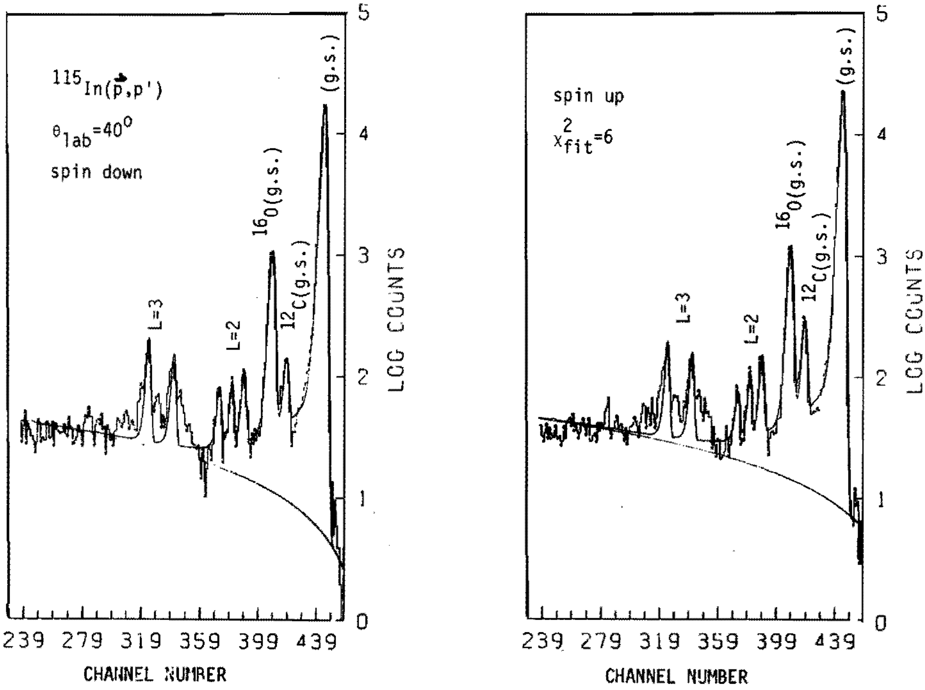

Fig. 4.14a Pulse height spectrum for ^{115}In, for spin up and spin down, analyzed with PIEK.

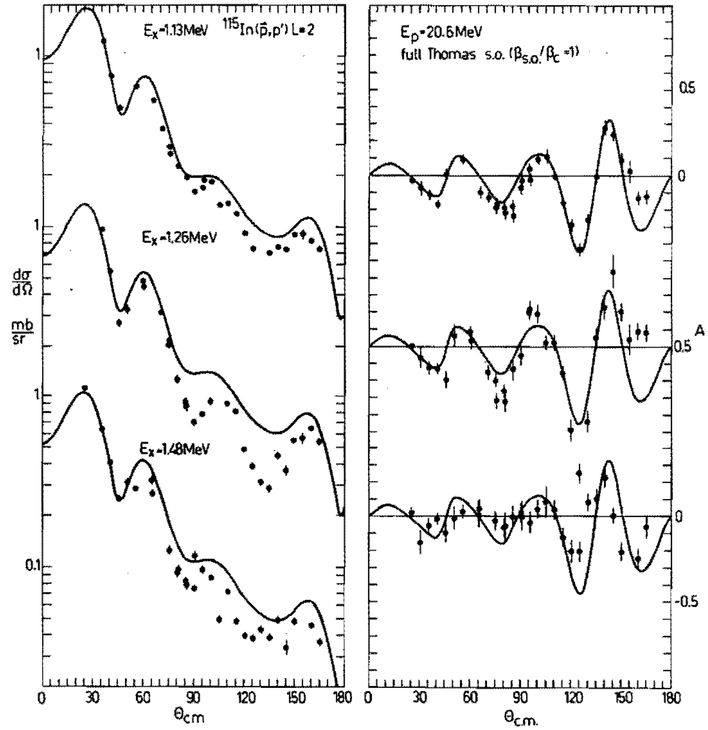

Fig. 4.15 Differential cross section and analysing power for inelastic scattering of protons by ^{115}In at 20.4 MeV leaving the target in the L=2 states. The curves are calculated with the DWBA, using the fixed geometry optical model parameters of Sn.

mean energies equal to the energies of the corresponding parent states in ^{116}Sn. The experimental deformation parameters should show a 2J+1 dependence for each final state and their sum should equal the deformation parameter of the parent state.

As a consequence of the energy resolution of 60 keV we could see only three L=2 and five L=3 transitions in our spectra. Fig. 4.14a shows a typical energy spectrum of ^{115}In. Only two of the five L=3 transitions had enough statistics to be analysed. Our experimental results and the DWBA curves are plotted in figs. 4.15 and 4.16 for the L=2 and L=3 states, respectively. We used here as optical model parapeters the GF set of Sn, so only the parameter W_D was different from the value for ^{116}Sn. The DWBA calculations describe the L=2 and L=3 states very well.

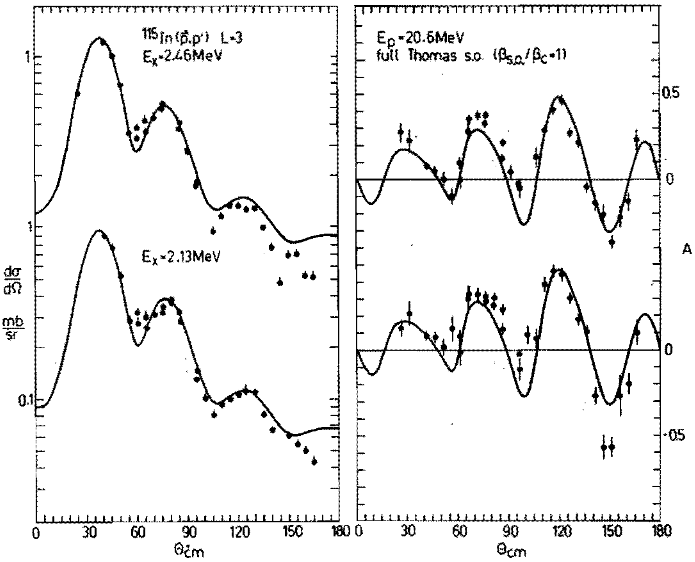

Fig. 4.16 Differential cross section and analysing power for inelastic scattering of protons by ^{115}*In at 20.4 MeV leaving the target in the L=3 states.*
The curves are calculated with the DWBA using the fixed fixed geometry optical model parameters of Sn.

First we will discuss the results for the quadrupole multiplet. The total strength of the analysed transitions amounted to be 79% of the parent 2^+ strength of ^{116}Sn, see table 4.10. We see from the peak fitting of the energy spectrum in fig. 4.14a that the missing strength of the multiplet based on the 2^+ state is only small.

Calculations with the weak coupling model for ^{115}In have been carried out by Dietrich (Die70), Covello (Cov73) and Smits (Smi77). Due to the mixing, the wave functions of the ground state and the excited states have the form

$$\sum_{NR} c^J_{NR} \; |(9/2)^+,NR;JM> \qquad N = 0,1,2 \qquad (4.1)$$

Here we use N quadrupole phonons, coupled to R; coupled to the hole $(1g\ 9/2)^+$, giving total angular momentum J. The factors c^J_{NR} are the decomposition factors. Dietrich has given a list of his decomposition factors, so we will use his results for the calculation of the overlap of the ground state and an excited state wave function. We multiply this overlap with 2Jf+1, giving $B_{f,th}$, which should be compared with:

Table 4.10 Experimental and theoretical B_f values of ^{115}In, L=2.

J^π	E_x (MeV)	$B_{f,th}$ a)	$B_{f,exp}$	2J+1
$5/2^+$	1.08	4.0	-	6
$11/2^+$	1.14	8.2	-	12
		12.2	17.5	18
$13/2^+$	1.29	9.8	12.4	14
$7/2^+$	1.46	6.1	-	8
$9/2^+$	1.49	1.5	-	10
		7.6	9.6	18
		29.6	39.5	50

$\bar{E}_{x,th.}$ = 1.27 MeV

exp. = 1.27 MeV

parent = 1.29 MeV

a) Calculated with the data of Dietrich (Die70) for 0 and 1 phonons.

Table 4.11 Review for the L=3 states of ^{115}In.

E_x (Mev)	B_f^{exp}	$2J_f+1$
2.13	22.7	
2.46	30.2	
	52.9	70

Weighted average energy (MeV):

$\bar{E}_{x,parent}$ ^{116}Sn = 2.27

exp. = 2.32

$$B_{f,exp} = (\beta_{f,exp}/\beta_{parent})^2(2J_i+1)(2L+1) \qquad (4.1)$$

Here β_{parent} is the deformation parameter of ^{116}Sn, 2_1^+. In table 4.10 we present the results. We see that due to the mixing of the two $9/2^+$ states the strength of the $9/2^+$ state at 1.49 MeV is reduced. Apart from a factor of about 1.3 the trend in $B_{f,exp}$ is very well reproduced. Using the decomposition factors of Smits we find nearly the same result.

The energy controid of the L=2 multiplet is only 2% lower than the excitation energy of the parent state. This small shift can be caused by the mixing of the states.

In table 4.11 we give a review of the L=3 data. The total strength of the analysed octupole states is 76% of the parent strength. But here some small peaks, which are visible in the energy spectrum, have not been analysed and so this percentage should be somewhat higher. Since for the L=3 states no spin assignments are available we cannot check the 2J+1 rule. We only can say that the largest J values of this multiplet should be situated around the energies of 2.13 and 2.46 MeV.

The weighted averaged energy is only 3% higher than in the parent state, which is a satisfactory result.

In conclusion we can say that the weak coupling model describes the experiment very well. A high resolution experiment with polarized protons would be desirable for a further study of ^{115}In. Also the low energy single-hole excitations, which are very weak but visible in our spectra, could be of much interest for a microscopic analysis.

4.3.5 Sn

Since tin has a more or less closed proton shell many stable isotopes are available. This enables us to investigate the influence of the increasing neutron number on the optical model parameters, volume integrals and so on. In accordance with our program of scattering of polarized protons we have chosen the energy of 20.4 MeV.

All curves were calculated with the collective DWBA using our GF optical model parameters. In all cases the spin-orbit deformation could be taken equal to the deformation of the central well. From the cross sections of the 2_1^+ states one can see in fig. 4.17 that the minimum around 120 degrees is described better for the heavier isotopes, whereas for the 3_1^- states, see fig. 4.18, the opposite is true.

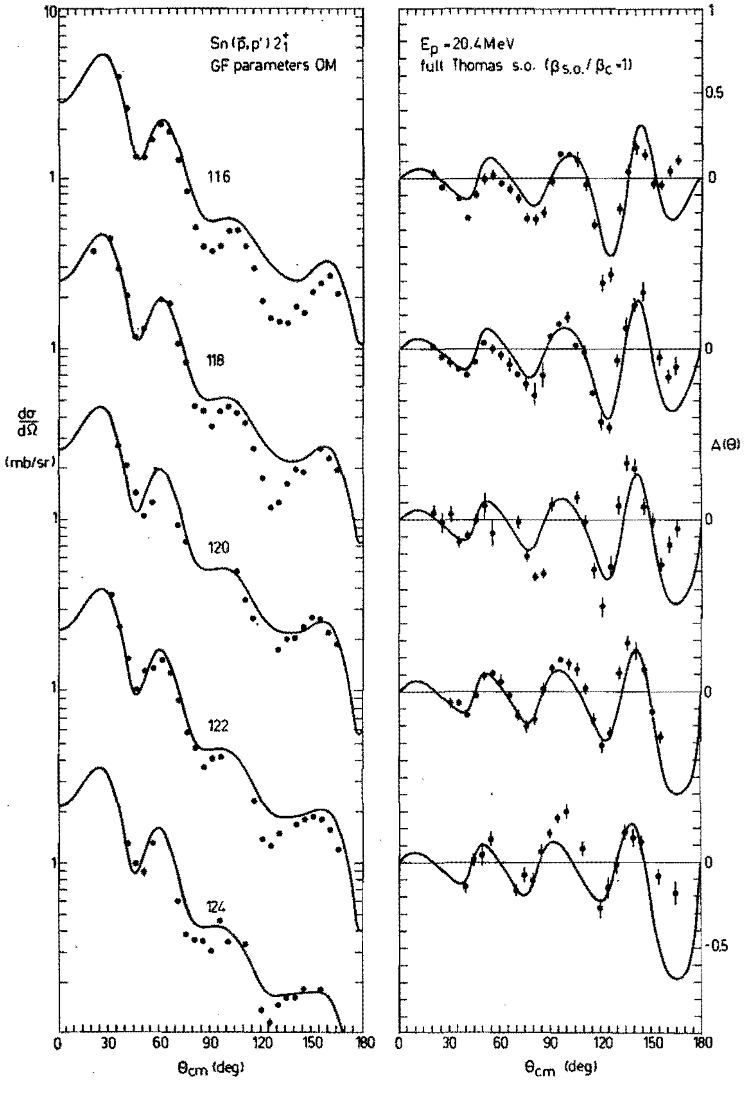

Fig. 4.17 Differential cross section and analysing power for inelastic scattering of protons by ^{116,118,120,122,124}*Sn at 20.4 MeV leaving the target in the* 2_1^+ *state. The curves are calculated with the DWBA, using the FG optical model parameters.*

So the 2_1^+ states of the Sn isotopes show a similar trend as the Ni isotopes (fig. 4.7) and the Zn isotopes (Hal80).

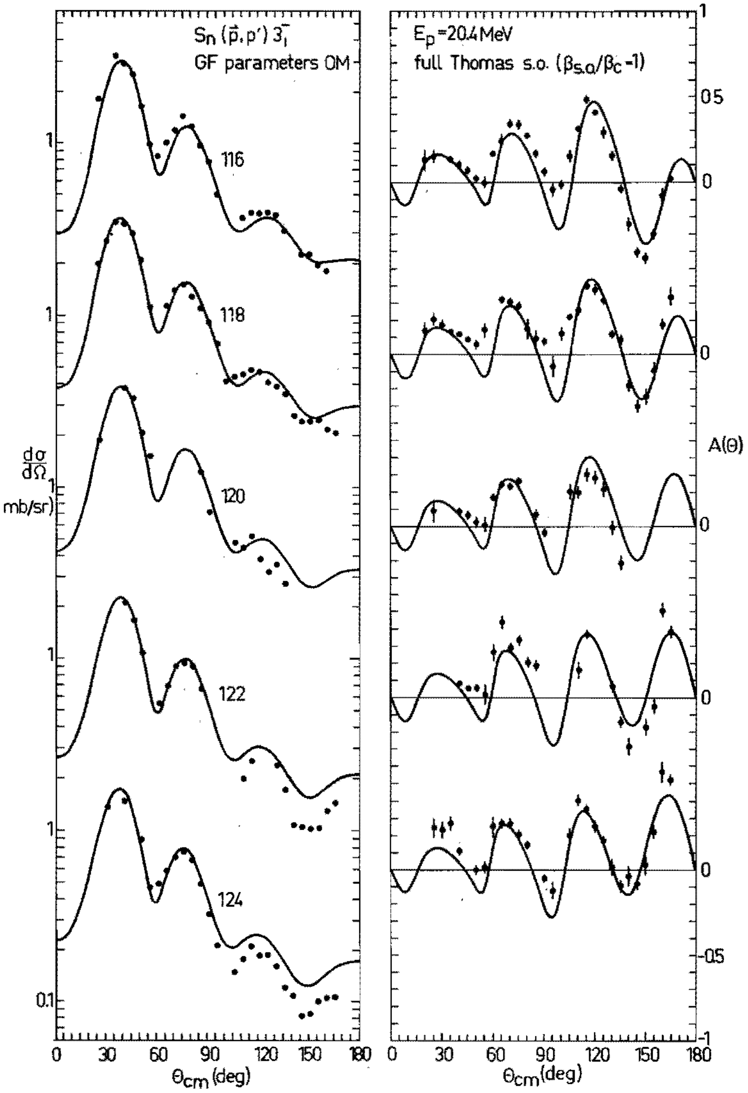

Fig. 4.18 Differential cross section and analysing power for inelastic scattering of protons by $^{116,118,120,122,124}Sn$ *at 20.4 MeV leaving the target in the* 3_1^+ *state. The curves are calculated with the DWBA, using the FG optical model parameters.*

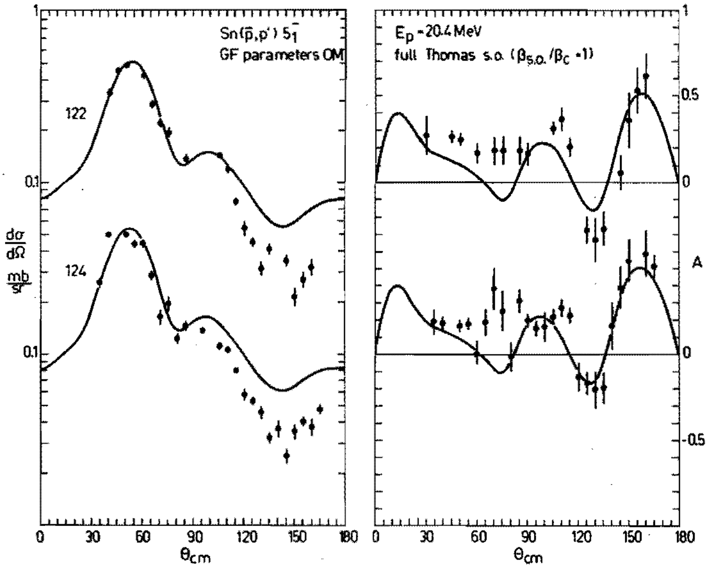

Fig. 4.19 Differential cross section and analysing power for inelastic scattering of protons by ^{122,124}Sn at 20.4 MeV leaving the target in the 5_1^- state.
The curves are calculated with the DWBA, using the FG optical model parameters.

For ^{122,124}Sn, data for the 5_1^- states could be extracted from the spectra. Also here the collective **DWBA** gives a very good description. The results are displayed in fig. 4.19.

In table 4.7 we have compared the extracted deformation parameters with the values given by Beer (Bee70). Our 2^+ parameters are about 6% larger while our 3^- deformation parameters are 8% smaller than those of Beer. The trend of decreasing parameters with increasing mass is equal. The difference could be caused by a different normalization procedure and also by different optical model potentials. The optical model parameters of Beer give, especially for the analyzing powers, rather bad fits.

Also the results of the experiment at 24.6 MeV on ^{120}Sn are very well described by the collective theory. The same proton energy has been used by Beer (Bee70), so we also performed a calculation with his optical model parameters. It appears that the geometrical part of the optical model parameter set of Satchler (Sat67), that has been used by Beer, gives less satisfactory fits than our geometry does, as can be

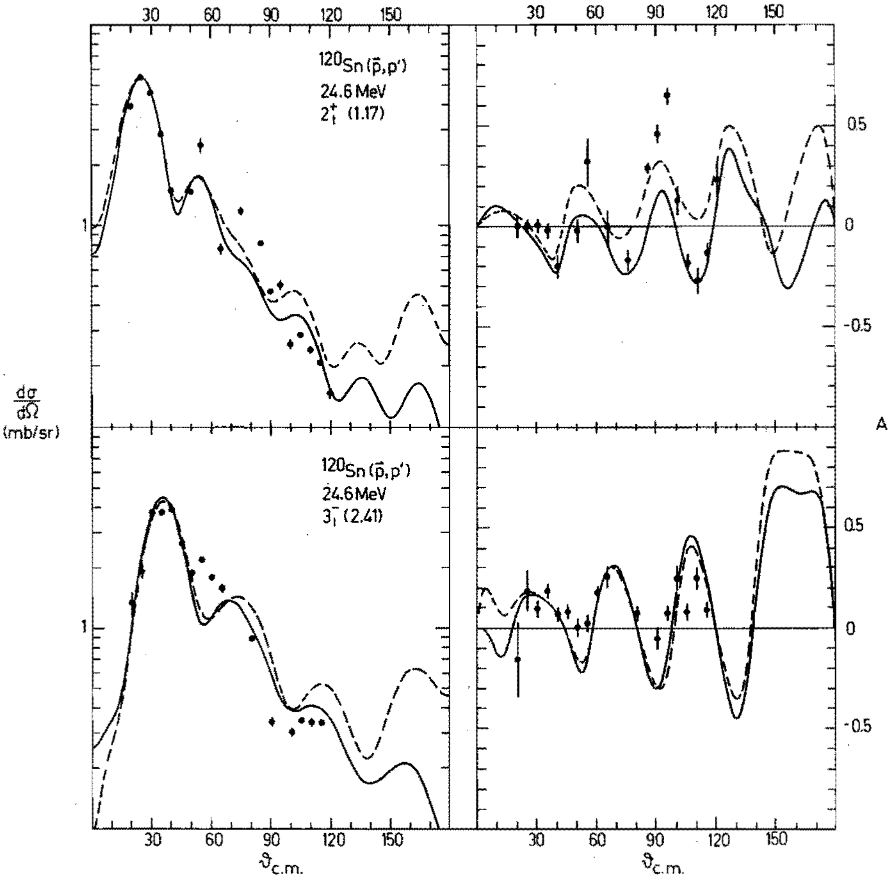

Table 4.20 Differential cross section and analysing power for inelastic scattering of protons by ^{120}Sn at 24.6 MeV leaving the target in the $2_1^+, 3_1^-$ state. The curves are calculated with the DWBA, using the FG optical model parameters (full curve) and those of Beer (dashed curve).

seen in fig. 4.20. Also the normalization differs rather much, namely about 25%. As discussed in section 4.2.2, the deformation parameter extracted using this optical potential, is nearly the same as with the GF potential.

We can conclude from this analysis that the collective model is very suitable for the description of the cross sections and analysing powers. It was not needed to enhance the spin-orbit deformation parameters.

CHAPTER 5 A MICROSCOPIC ANALYSIS OF INELASTIC SCATTERING FROM ^{116}Sn AND ^{124}Sn

5.1 Introduction

In this microscopic analysis we use the antisymmetrized distorted wave formalism as presented in section 3.4. In the previous chapter we have seen that the collective model can give a very good description of the experiment. In this chapter we will show and discuss the results of purely microscopic calculations and of a combination of the collective and microscopic approach.

The following ingredients are required in order to calculate the angular distributions (Ger71, Amo78):

- optical model parameters
- single-particle binding energies
- bound state single-particle wave functions
- spectroscopic amplitudes for all possible allowed single-particle transitions
- effective nucleon-nucleon interaction.

The optical model parameters are used to calculate the distorted waves. We employ the global fit parameter sets (GF), which differ only in the strength of the imaginary volume potential for the diverse Sn isotopes. These parameters are listed in table 5.1. The differences in W_V are only small, so possible differences in the results between

Table 5.1 Optical model parameters for ^{116}Sn and ^{124}Sn, Global fit.

V_o	54.97 MeV	r_i	1.266 fm
r_o	1.178 fm	a_i	0.695 fm
a_o	0.730 fm	V_{so}	5.65 MeV
W_V	1.20 MeV	r_{so}	0.970 fm
W_D	8.84 MeV (^{116}Sn) or 10.01 MeV (^{124}Sn)	a_{so}	0.699 fm

^{116}Sn and ^{124}Sn cannot be caused by differences in the optical model parameters.

The single-particle binding energies, as listed in table 5.2, were derived from the shell model single-particle energies and the separation energy of the proton or neutron. We obtained the single-particle energies by interpolating the values for the odd Sn isotopes as given by Van Gunsteren (Gun74), while the separation energies were taken from the Nuclear Data Sheets (Wap71).

The bound state wave functions were generated in Woods-Saxon wells, from which we varied the depths in order to obtain abovementioned binding energies. The geometry parameters of these wells were chosen equal to the parameters of the real central optical model potential (GF).

Table 5.2 Single-particle binding energies (b.e.) and bound state Woods-Saxon well depths (V_{ws}), both in MeV, for ^{116,124}Sn.

A		116		116		124		124	
state		protons		neutrons		protons		neutrons	
nl	j	b.e.	V_{ws}	b.e.	V_{ws}	b.e.	V_{ws}	b.e.	V_{ws}
1g	7/2	5.52	70.8	7.70	52.8	8.35	71.8	5.89	47.9
2d	5/2	5.02	65.2	7.32	48.5	7.85	66.9	5.83	44.8
3s	1/2	4.27	67.6	8.34	52.6	7.10	69.4	7.14	50.1
2d	3/2	3.27	67.4	8.03	53.1	6.10	69.1	7.14	50.1
1h	11/2	2.75	66.3	7.83	55.2	5.60	67.4	7.16	52.6
1f	5/2	11.27	63.5			14.10	97.5		
2p	3/2	11.27	60.2			13.10	62.0		
2p	1/2	9.27	61.4			12.10	63.2		
1g	9/2	9.27	62.7			12.10	64.1		
s.e.[a]		9.27	-	9.57	-	12.10	-	8.49	-

a) s.e. is the separation energy in MeV.

Separate shell model calculations are needed for the evaluation of the spectroscopic amplitudes. We used the results of BCS quasi-particle calculations of Allaart (All79) and Gillet (Gil76). Both authors used an inert N=50 and Z=28 core, so the Z=50 shell of Sn is open in both analyses. Contrary to Gillet, Allaart used a projection method that conserves the number of particles. In tables 5.3, 5.4 and 5.5 the spectroscopic amplitudes of Allaart and Gillet for the collective 2_1^+, 3_1^- and 5_1^- states are listed, for all possible transitions in our model. We derived the spectroscopic amplitudes

Table 5.3 Spectroscopic amplitudes for the 2_1^+ states of ^{116,124}Sn, in i^1 convention.

A	116	116	124	124
	Allaart	Gillet	Allaart	Gillet
neutron single-particle transitions				
g7 - g7[a]	0.0603	0.0689	0.0704	0.1048
g7 - d5	-0.0191	-0.0113	-0.0160	-0.0161
g7 - d3	-0.3330	-0.3806	-0.2122	-0.2292
d5 - g7	0.0172	0.0153	0.0141	0.0202
d5 - d5	0.0699	0.0231	0.0595	0.0455
d5 - s1	-0.2667	-0.2361	-0.1949	-0.1333
d5 - d3	-0.1447	-0.0898	-0.1102	-0.0948
s1 - d5	-0.0929	-0.0617	-0.0653	-0.0681
s1 - d3	0.3340	0.4361	0.1869	0.2417
d3 - g7	-0.0814	-0.0820	-0.0605	-0.1149
d3 - d5	0.0394	0.0297	0.0356	0.0380
d3 - s1	-0.2604	-0.1928	-0.1802	-0.1696
d3 - d3	0.2525	0.1322	0.2047	0.2386
h11 - h11	0.0846	0.0969	0.4587	0.4319
proton single particle transitions				
g9 - g7	-0.0627	-0.046	-0.0868	-0.074
g9 - d5	-0.2924	-0.245	-0.2894	-0.239

a) g7 is the abbreviation of 1g 7/2 etc.

of Gillet from his RPA amplitudes X and Y (Gil76), using the occupation probabilities u and v (Gil67) of the shell model states. For different single-particle orbits the spectroscopic amplitude from state 1 to 2 is:

$$1 \rightarrow 2: \quad S(j_1 j_2 J_i J_f J) = X_{12} u_2 v_1 + Y_{12} u_1 v_2 \tag{5.1}$$

while for reverse case we have:

$$2 \rightarrow 1: \quad S(j_2 j_1 J_i J_f J) = (-)^{j1+j2+J} \; (X_{12} u_1 v_2 + Y_{12} u_2 v_1) \tag{5.2}$$

For a transition within the same state, i.e. a recoupling, we get:

$$1 \rightarrow 1: \quad S(j_1 j_1 J_i J_f J) = \sqrt{2} \; (X_{11} + Y_{11}) \; u_1 v_1 \tag{5.3}$$

Table 5.4 Spectroscopic amplitudes for the 3_1^- states of tin in i^l convention.

A	116 Allaart	116 Gillet	124 Allaart	124 Gillet
neutron single particle transitions				
g7 - h11	0.1337	0.2655	0.0980	0.1553
d5 - h11	-0.6501	-0.6429	-0.3904	-0.4052
h11 - g7	-0.0142	-0.1083	-0.0446	-0.1046
h11 - d5	-0.0775	-0.2294	-0.2015	-0.2200
proton single particle transitions				
f5 - g7	0.1745	0.266	0.1656	0.244
f5 - d5	-0.0630	-0.131	-0.0629	-0.101
f5 - s1	0.0511	0.125	0.0543	0.098
f5 - d3	-0.0505	-0.129	-0.0505	-0.114
p3 - g7	0.1486	0.144	0.1295	0.130
p3 - d5	0.1636	0.245	0.1610	0.180
p3 - d3	-0.1269	-0.244	-0.1234	-0.204
p1 - g7	-0.4828	-0.271	-0.4536	-0.255
p1 - d5	0.2758	0.297	0.2782	0.222
g9 - h11	0.2103	0.342	0.1950	0.221

We learn from these tables that the differences between both sets are rather small. Because of the number conservation we preferred the use of the set of Allaart in our further analyses.

For the calculation of the single-particle contributions we need an effective nucleon-nucleon interaction. In table 5.6 we list some currently used interactions. Most of our calculations have been performed using the central effective interaction derived from the interaction of Hamada and Johnston (Ham62) (denoted by HJ). This central effective interaction is an approximation of the long range part of the even state HJ interaction, using a separation distance of 1.05 fm. (In the program MEPHISTO this long range part is approximated by a sum of truncated Yukawa functions). We completed this central interaction with the non-central tensor and spin-orbit interactions deduced by Eikemeier and Hackenbroich (Eik71) (abbreviated as EH).

In order to get an idea of the influence of the effective interaction on the angular distributions we performed an additional calculation for the 2_1^+ state of ^{116}Sn using the phenomenological central interaction of Austin (Aus79) combined with the tensor interaction of Sprung (Spr72) and the spin-orbit interaction of Eikemeier and Hackenbroich (Eik71).

Table 5.5 Spectroscopic amplitudes of the 5_1^- state of ^{124}Sn in i^l convention from Allaart.

neutron transitions		proton transitions	
g7 - h11	0.0656	f5 - g7	0.0532
d5 - h11	-0.1330	f5 - d5	-0.0933
s1 - h11	0.3086	p3 - g7	0.1450
d3 - h11	-0.2197	g9 - h11	0.0759
h11 - g7	-0.299		
h11 - d5	-0.0687		
h11 - s1	0.4752		
h11 - d3	0.3509		

Table 5.6 Some effective nucleon-nucleon interactions.

1. Central $= V_{so} + V_{se} + V_{te} + V_{to}$

(a) Hamada-Johnston: the long-range part is approximated by a sum of truncated Yukawa functions Y_t, with a separation distance r_s of 1.05 fm.

$$V_{se} = - 11.152\ Y_t\ (0.7) + 6.62\ Y_t\ (1.4) - 4.81\ Y_t\ (2.1) + {}$$
$$+ 490\ Y_t\ (2.8) - 1477\ Y_t\ (3.5) + 2620\ Y_t\ (4.2)$$

$$V_{te} = - 33.46\ Y_t\ (0.7) + 6.35\ Y_t\ (1.4) - 68.74\ Y_t\ (2.1) + {}$$
$$+ 1516\ Y_t\ (2.8) - 6029\ Y_t\ (3.5) + 10611\ Y_t\ (4.2)$$

(b) Austin

$V_{so} = - 2.7\ Y\ (1.0)$
$V_{se} = - 82.30\ Y\ (1.0)$
$V_{te} = - 97.10\ Y\ (1.0)$
$V_{to} = 10.3\ Y\ (1.0)$

(c) Gillet

$V_{se} = - 32\ G\ (1.7)$
$V_{te} = 8\ G\ (1.7)$

(d) Allaart

$V_{se} = - 32\ G\ (2.02)$
$V_{te} = 8\ G\ (2.02)$

---

2. Tensor = $(V_{te} + V_{to})\, r^2\, S_{12}$

(a) Eikemeier and Hackenbroich

$$V_{te} = -\ 105.3\ G\ (0.960) - 1.95\ G\ (2.034)$$
$$V_{to} = 17.92\ G\ (1.146) + 2.31\ G\ (1.383) + 0.38\ G\ (2.234)$$

(b) Sprung

$$V_{te} = -\ 802.16\ G\ (0.50) - 104.4\ G\ (0.95) - 2.71\ G\ (1.70)\ + \\ -\ 0.18\ G\ (2.85) - 0.001\ G\ (5.00)$$

$$V_{to} = 145.24\ G\ (0.50) + 24.28\ G\ (0.95) + 1.13\ G\ (1.70)\ + \\ +\ 0.046\ G\ (2.85) + 0.0004\ G\ (5.00)$$

3. Spin-orbit = $(V_{te} + V_{to})\ \vec{L}\cdot\vec{S}$

(a) Eikemeier and Hackenbroich

$$V_{te} = 213.9\ G\ (0.747)$$
$$V_{to} = -\ 282.4\ G\ (0.765) - 5.18\ G\ (1.021)$$

(b) Sprung

$$V_{te} = 883.72\ G\ (0.5) - 116.40\ G\ (0.95) + 0.51\ G\ (1.70)\ + \\ +\ 0.017\ G\ (2.85)$$

$$V_{te} = -\ 1412\ G\ (0.5) + 56.95\ G\ (0.95) - 0.69\ G\ (1.70)\ - \\ +\ 0.014\ G\ (2.85)$$

Y is the Yukawa function: $Y(x) = \exp(-r/x)(r/x)$

Y_t is the truncated Y : $Y_t(x) = Y(x)$ for $x > r_s$
$Y_t(x) = 0$ for $x < r_s$

G is the Gauss function : $G(x) = \exp((r/x)^2)$

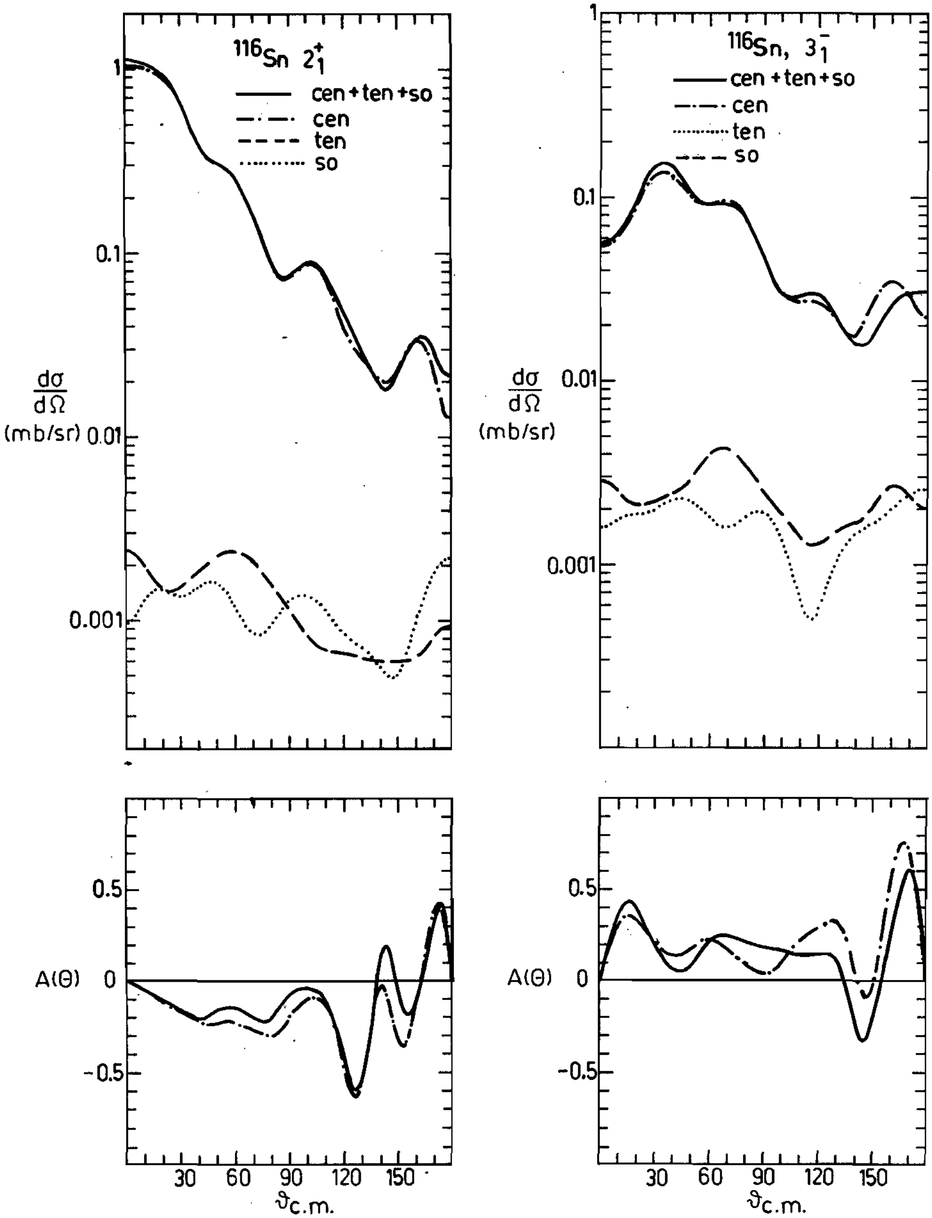

Figs. 5.1a and 5.1b Angular distributions calculated with the central (cen), tensor (ten), spin-orbit (so) and total microscopic interaction.

5.2 Purely microscopic calculations

Disposing of the above ingredients we calculated for all allowed single-particle transitions (proton and neutron transitions) in our model the central, tensor and spin-orbit transition amplitudes. The direct and the exchange contributions were calculated separately. So for each single-particle transition six transition amplitudes were calculated. We used hereto the program MEPHISTO of Von Geramb (Ger73). All these transition amplitudes must be summed using the spectroscopic amplitudes as weight factors (see chapter 3). Then the cross sections and analysing powers can be calculated. There are several combinations possible of the various transition amplitudes:

- First we may sum all central, all tensor and all spin-orbit contributions to get three transition amplitudes.
- Another possibility is to sum all direct (D) and all exchange (E) contributions to two transition amplitudes.
- Finally we can construct a proton (P) and a neutron (N) transition amplitude.

This feature enabled us to investigate the importance of these various components.

5.2.1 Effects of non-central forces

First of all we compare the central, tensor and spin-orbit contributions to the cross section and analysing power. The sum of these three contributions is often called the valence contribution. The central contribution is, as expected, much larger than the non-central contributions, e.g. for a 2^+ transition a factor of 400. So for the cross section the non-central interactions are of minor importance. As can be seen from figs. 5.1a and 5.1b the non-central parts have about the same magnitude.

For the analysing power, however, the differences between the curves of the central and valence interaction are not unimportant, especially for the 3^- states. See figs. 5.1a and 5.1b, where we show the various contributions to the valence cross section and analysing power.

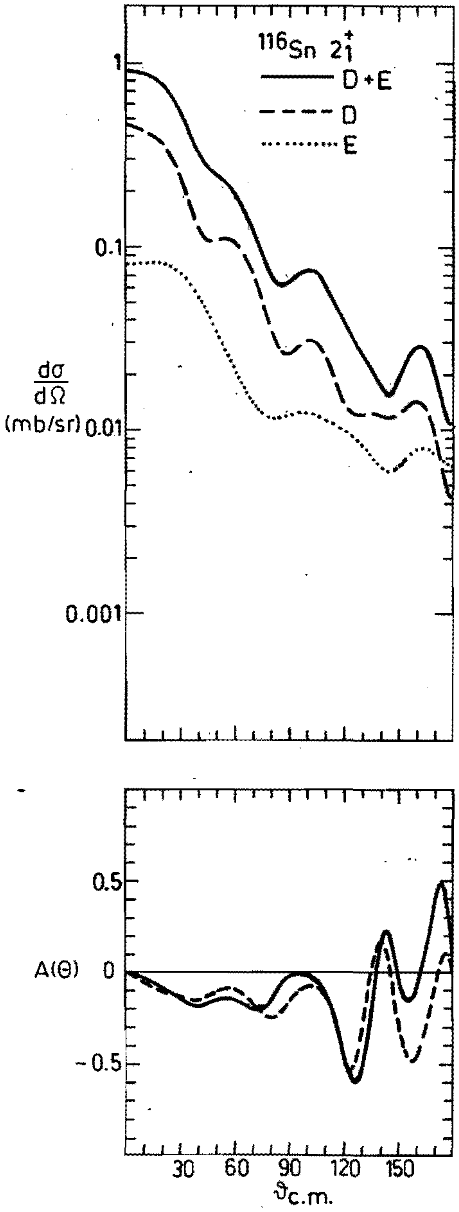

Fig. 5.2 Direct (D), exchange (E) and total angular distributions.

5.2.2 The importance of exchange

In the program MEPHISTO the exchange distribution was calculated to full extent. We find that the importance of the exchange contributions increases with increasing L-values. The ratios of the D and E cross sections are 3.5, 2 and 1 for L = 2, 3 and 5, respectively. For the excitation of the 5_1^- state in ^{124}Sn the exchange contribution in the proton transitions is even somewhat larger than the direct part.

It turns out that the cross section of the total contribution (D+E) is about a factor of two till three larger than the cross section of the direct contribution only, while the shapes are nearly the same as can be seen in fig. 5.2 for the 2_1^+ state of ^{116}Sn. This effect for the cross section has also been found by Terrien (Ter73). Also for the analysing powers the differences between D and (D+E) curves are small, except for 5_1^- states which show some differences. So the increase of cross section by adding the exchange contributions is the most important point here, the shape of the curves is not changed essentially. In our calculations in the next sections we always use the total microscopic contribution.

5.2.3 Proton and neutron contributions

The neutron contribution (N) is always larger than the proton contribution (P), as can be expected for nuclei with a closed proton shell. For the 2_1^+ and 5_1^- states the neutron contribution is about a factor of 100 larger, for the 3_1^- states a factor of about 4. This stems from two facts. In the first place the proton-neutron interaction is a factor of 2 stronger than the neutron-neutron interaction. In addition less proton than neutron contributions are possible (see tables 5.3, 5.4 and 5.5). In figs. 5.3a and 5.3b we display the proton, neutron and valence contributions for ^{116}Sn, 2_1^+ and 3_1^-. We see for the 3_1^- state that the shapes of the total and N cross sections are nearly equal but that the analysing powers differ. So, though the proton contribution is not so large, it influences the analysing power substantially.

The valence microscopic transition amplitudes give cross sections that are much smaller than the experimental cross sections. For example a factor of 3, 19 and 12 lower for the 2_1^+, 3_1^- and 5_1^- states

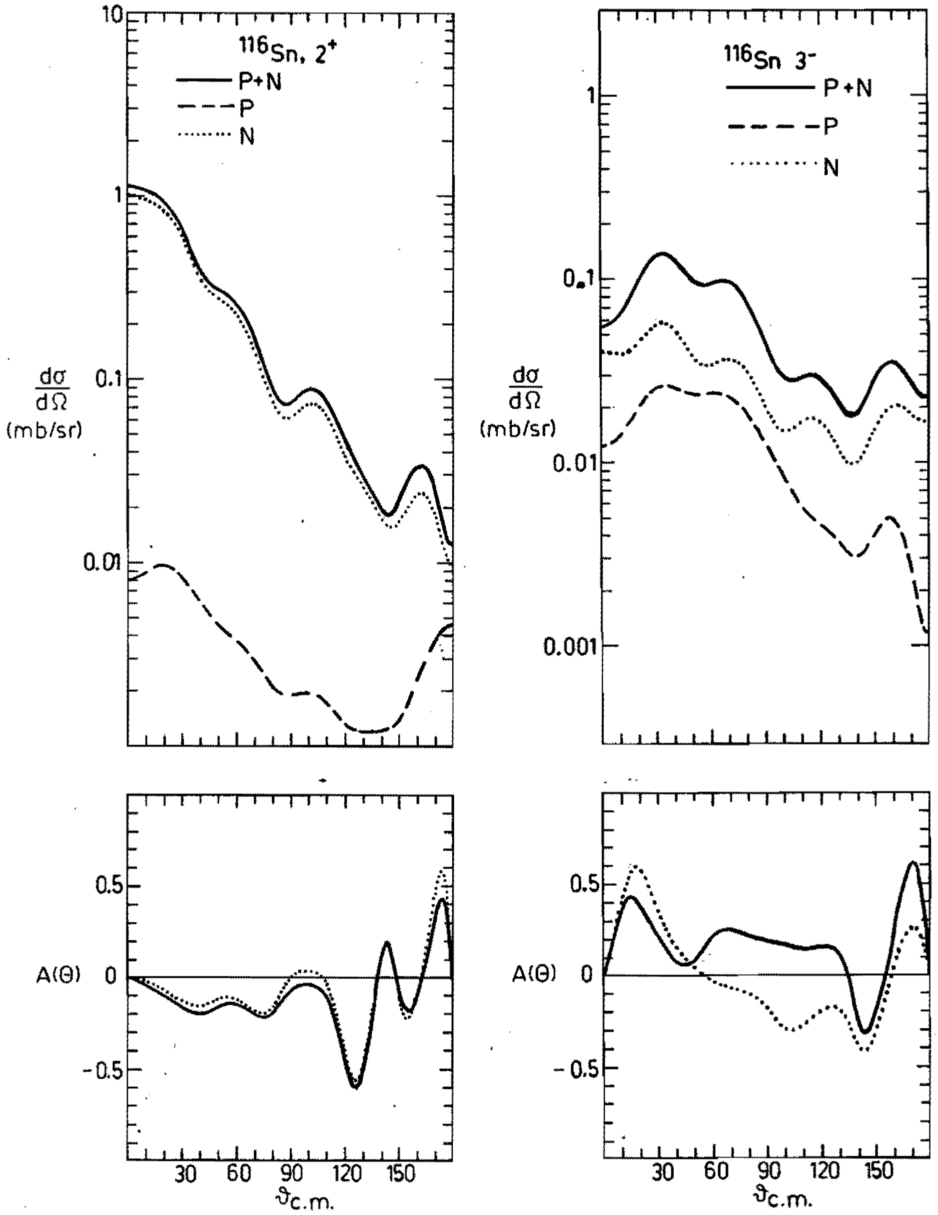

Figs. 5.3a and 5.3b Proton (P) and neutron (N) contributions to the total (P+N) angular distributions.

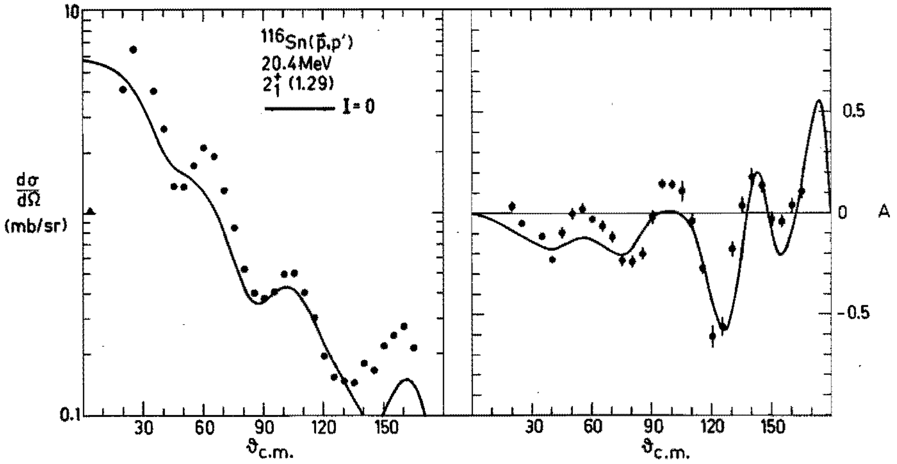

Fig. 5.4a Fit to the experimental cross section and analysing power of ^{116}Sn, 2_1^+. An imaginary contribution is not included (I=0). The enhancement parameters are $\lambda_p=1.0$ and $\lambda_n=2.5$.

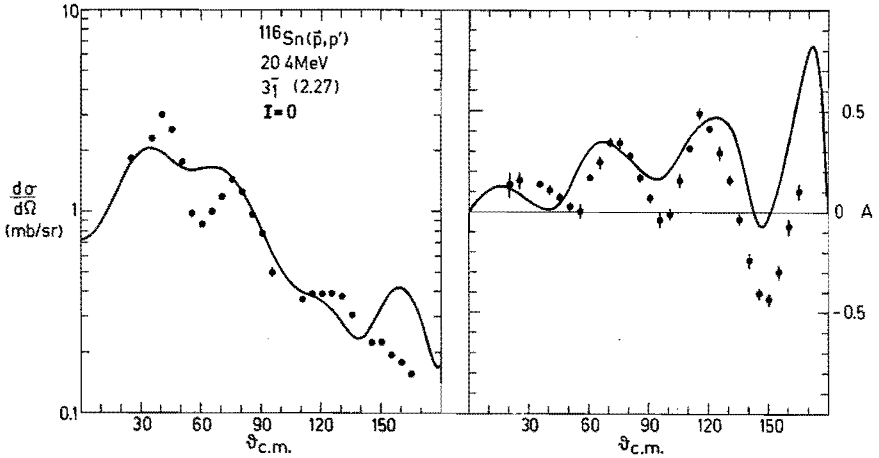

Fig. 5.4b Fit to the experimental cross section and analysing power of ^{116}Sn, 3_1^-. An imaginary contribution is not included (I=0). The enhancement parameters are $\lambda_p=5.8$ and $\lambda_n=1.6$.

of ^{124}Sn, respectively. Also the shapes of these theoretical curves do not fit well the experimental angular distributions. The reduced transition probabilities B(EL) calculated with the microscopic model, are also much smaller, at least a factor of two, than the experimental values (see section 5.2.4).

So we conclude here that the purely microscopic calculation cannot describe the inelastic scattering from the collective states, though we have used all possible single-particle transitions in our model. Oftenly in these cases the effective charges of the protons and neutrons, e_p and e_n, are adjusted in order to fit the height of the cross section. The enhancement factors for the transition amplitudes are namely $\lambda_p = e_p$ and $\lambda_n = e_n+1$. In this way it is possible to fit the height of the cross section as can be seen in figs. 5.4a and 5.4b. Here, for ^{116}Sn, 2_1^+, the values of λ_p and $_n$ are 1.0 and 2.5, respectively, and for ^{116}Sn, 3_1^-: 5.8 and 1.6. We see, however, from the figure that the cross section lacks structure. This is originated by the fact that no imaginary interaction has been included. It is nowadays well known that the effective nucleon-nucleon interaction has such a component. From theoretical calculations (Bri78) and from the collective model it is known that the imaginary form factor has the effect of giving structure to the cross section. Following the somewhat 'frivolous' model of Satchler (Sat67), we have simulated this effect, in section 5.3, by adding the collective imaginary form factor to the microscopic one.

5.2.4 Reduced transition probabilities

Together with the transition amplitudes we calculated the microscopic contributions to the reduced transition probabilities B(EL), according to the formulae given in section 3.7. In table 5.6b we compare the theoretical values with the experimental results from Coulomb excitation experiments (Alk65, Ste70). We see that the pure microscopic values with effective charges for the protons of 1 and of the neutrons of 0, give transition probabilities that are a factor of 14 to 90 too low. With effective charges of 1.5 and 0.5, respectively, the discrepancy is reduced to a factor of about 4.

Compared to the Allaart amplitudes, the Gillet set leads to somewhat lower B(E2) values, but the B(E3) values are a little larger.

When we generate the bound state wave functions in a harmonic oscillator well instead of a Woods-Saxon well, the theoretical transition probabilities increase. Depending on the harmonic oscillator parameters this increase can be considerable. The harmonic oscillator shape used by Allaart, combined with effective charges of $e_p=1.5$ and $e_n=0.5$, gives B(E2) values which are only a factor of 1.5 too low, while the B(E3) values are nearly equal to the experimental values.

In eq. 3.15 we gave the formula for the calculation of the collective transition probability. This approach, where we use our experimental deformation parameters from the DWBA, gives too high values for the B(E2). The B(E3) values compare rather well with the experiments.

So the low values of the pure microscopic transition probabilities show the need for relatively large effective charges and/or the inclusion of collective contributions. In our analysis in the next section we come back to this point.

5.3 Calculations including core polarization

We have seen that the pure microscopic calculations cannot describe the experimental data satisfactorily. When the collective imaginary interaction is added the structure of the cross section is described much better, but the experimental height is not reached yet. The core polarization should be taken into account in order to fit this height. There are two approaches possible for including core polarization effects in the microscopic calculations. In both cases the imaginary collective transition amplitude is added to the microscopic one.

In the first approach the proton (P) and neutron (N) contributions are enhanced. The total transition amplitude is then:

$$T = \lambda_p T_p + \lambda_n T_n + T_I \tag{5.4}$$

Here λ_p and λ_n are the proton and neutron enhancement parameters of the microscopic P and N transition amplitudes. In T_I, which is the collective imaginary transition amplitude, the (DWBA) deformation parameter is incorporated. The transition probability is:

Table 5.7a Reduced transition probabilities $B(EL, 0 \rightarrow L)$ for $^{116,124}Sn$.

			state		2^+_1		3^-_1		5^-_1
			units		(e^2fm^4)		$(10^3\ e^2fm^6)$		$(10^6\ e^2fm^{10})$
			A		116	124	116	124	124
BS a)	S b)	e_p	e_n	λ_c	B(E2)	B(E2)	B(E3)	B(E3)	B(E5)
WS	All	1.0	0.0	0	24	26	18	16	2
WS	All	0.0	1.0	0	1069	1332	12	9	58
WS	All	1.5	0.5	0	563	672	66	57	32
WS	Gil	1.5	0.5	0	448	635	90	63	-
HO	All	1.5	0.5	0	777	913	114	104	84
HOa	All	1.5	0.5	0	1246	1431	232	198	273
WS	All	1.0	0.0	1	372	233	163	131	14
WS	All	λ_p c)	λ_n-1 c)	0	1659	1069	495	156	73
WS	All	1.0	0.0	λ_c d)	181	122	119	95	14
collect. e)		-	-	-	4649	2642	260	162	250
exper.		-	-	-	2160 f)	1610 f)	220 g)	200 g)	-

a) BS = bound state wave function:
WS = Woods-Saxon well,
HO = Harmonic oscillator with energy of 8.3 MeV,
HOa = HO used by Allaart, energy is 6.62 MeV.

b) S = spectroscopic amplitudes:
All = set of Allaart,
Gil = set of Gillet.

c) Fit EC, see table 5.8.

d) Fit CP, see table 5.8.

e) Calculated with the collective model, using the deformation parameters from table 4.7.

f) Experimental values of Stelson (Ste70), relative error 25%.

g) Experimental values of Alkhazov (Alk65), relative errors 40%.

$$B(EL) = (e_p D_{pv} + e_n D_{nv})^2 \tag{5.5}$$

where D_{pv} and D_{nv} are the proton and neutron microscopic contributions (see section 3.7).

In this approach both the protons and neutrons have an effective charge: $e_p = \lambda_p$ and $e_n = \lambda_n - 1$. The two parameters λ_p and λ_n can be varied in order to fit the cross section, analysing power and the transition probability simultaneously. We call this method the "effective charge method", denoted by EC.

Terrien (Ter73) followed a somewhat different procedure. He took $e_n = 0$ and $\lambda_p = e_p$ where e_p is calculated from:

$$e_p = (B_{exp}(EL))^{\frac{1}{2}}/D_{pv} \tag{5.6}$$

So in his analysis e_p followed directly from the experimental transition probability. Now λ_n is the only parameter left to fit the experimental cross section. We will call this method the "proton charge method" and denote it by PC.

In the second approach the complete core plays a role. We can say say that the whole nuclear core is excited and deexcited during the scattering process, so the core will be polarized. Following the prescription of Love and Satchler (Lov67, Ger73), a part of the complete (real plus imaginary) collective transition amplitudes is added to the microscopic one. The relative strength of this addition is the core coupling parameter y_L. The microscopic part remains fixed (λ_p=1 and λ_n=1). In this case the total transition amplitude is:

$$T = T_p + T_n + \lambda_I T_I + \lambda_c T_c \tag{5.9}$$

In the terms T_c and T_I, the real and imaginary transition amplitudes, the collective deformation parameter is incorporated. Since the collective and core form factors are proportional (see section 3.6), we can take instead of the transition amplitudes of the core those of the collective model. We do this since in the collective DWBA code of Verhaar the full Thomas spin-orbit form factor is incorporated, while in the program MEPHISTO another type is used. The transition probability is now

$$B(EL) = (D_{pv} + \lambda_c D'_{pc})^2 \tag{5.8}$$

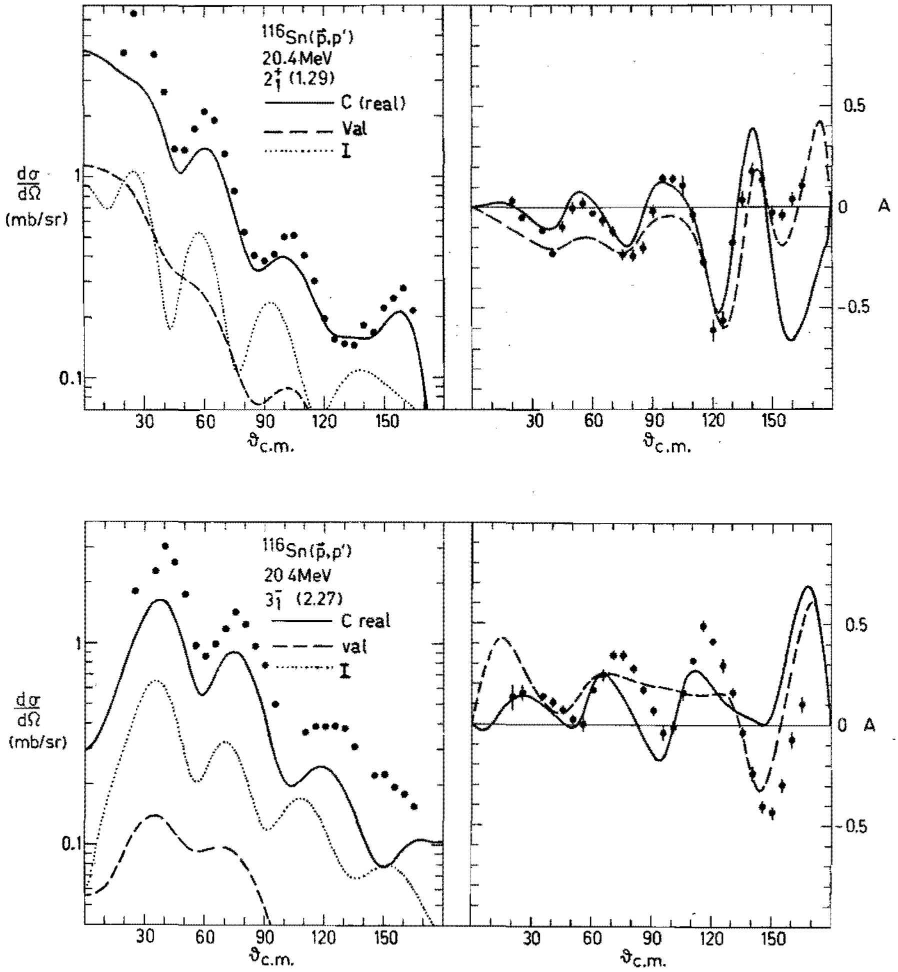

Figs. 5.5a and 5.5b The experimental cross section and analysing power of ^{116}Sn, compared with the real collective contribution (C), the imaginary collective contribution (I) and the total microscopic contribution (val).

Table 5.7b
Core coupling coefficients y_L found in the CP fits.

A	L	y_L (10^{-3} MeV^{-1})
116	2	1.04
	3	1.03
124	2	0.70
	3	0.86
	5	0.95

Since here the effective charge of the protons is 1 and of the neutrons 0. Also the transition probabilities calculated with the (pure) core and collective model are the same which gives us the following equation for D'_{pc}:

$$D'_{pc} = \frac{\beta_L \; (B_{coll}(EL;R_{eq}=R_c))^{\frac{1}{2}}}{D_{pc} + D_{nc}} \tag{5.9}$$

We use here eq. 3.15 for the calculation of $B_{coll}(EL)$ and D_{nc} is defined in a similar way for the neutrons as D_{pc} for the protons (eq. (3.18)).

Also here two methods are possible. In the first approach we take $\lambda_l=\lambda_c$, so λ_l is less than 1. In the second method we take $\lambda_l=1$, like in the EC and CP methods, and treat λ_c as a parameter. These methods we will call the core polarization (CP) and the corrected core polarization (CCP) method, respectively.

Before starting with the fitting procedures we will compare the cross sections of the microscopic valence, the imaginary collective and real collective interactions. We see from figs. 5.5a and 5.5b that for ^{116}Sn, 2_1^+ the cross sections are of the same order of magnitude but that for the 3_1^- state of ^{116}Sn the imaginary cross section is about a factor of 5 larger. In both cases the imaginary curve shows large oscillations, in other words it will be responsible for the structure in the curves.

The real collective cross section is almost a factor of three higher than the imaginary one. So inclusion of a small part of this contribution will have a large effect on the angular distributions.

Table 5.8 Results of the microscopic analysis with four types of calculations:
EC = effective charge,
PC = proton charge,
CP = core polarization,
CCP = corrected core polarization.

A	L	type	λ_p	λ_n	λ_I	λ_c	χ^2_σ	χ^2_A	B(EL)c)
116	2	EC	1.02	2.11	1.00	0.00	4533	1058	1659
		PC	9.43	1.00	1.00	0.00	8673	2686	2160a)
		CP	1.00	1.00	0.59	0.59	1583	426	181
		CCP	1.00	1.00	1.00	0.44	2809	387	128
116	3	EC	4.86	1.50	1.00	0.00	1933	646	495516
		PC	3.52	2.37	1.00	0.00	2351	446	220000b)
		CP	1.00	1.00	0.78	0.78	407	427	119163
		CCP	1.00	1.00	1.00	0.69	490	315	101907
124	2	EC	1.00	1.76	1.00	0.00	1688	755	1069
		PC	7.85	1.00	1.00	0.00	5945	1795	1610a)
		CP	1.00	1.00	0.59	0.59	570	500	122
		CCP	1.00	1.00	1.00	0.43	936	380	90
124	3	EC	1.28	3.41	1.00	0.00	3915	1054	156616
		PC	3.54	1.76	1.00	0.00	2774	2269	200000b)
		CP	1.00	1.00	0.77	0.77	549	581	95235
		CCP	1.00	1.00	1.00	0.62	1154	450	73888
124	5	EC	1.82	1.82	1.00	0.00	27608	813	7.29×10^7
		CP	1.00	1.00	0.99	0.99	1410	181	1.44×10^7
		CCP	1.00	1.00	1.00	1.00	4117	178	1.45×10^7

a) Experimental values of Stelson (Ste70).
b) Experimental values of Alkhazov (Alk65).
c) Units: e^2fm^{2L}.

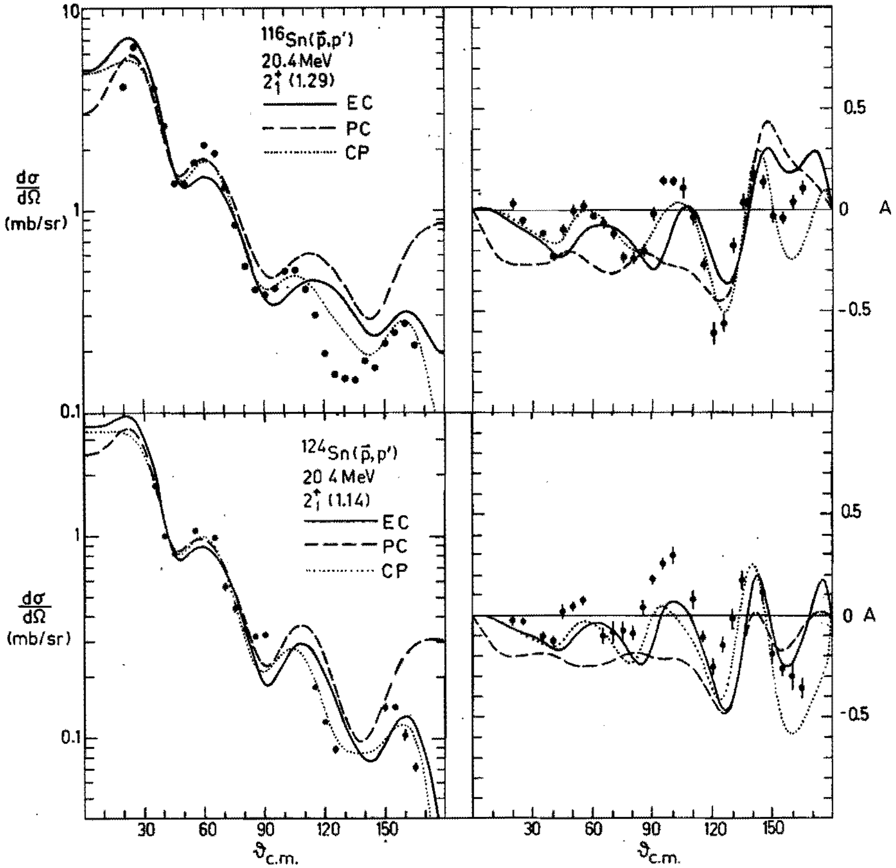

Fig. 5.6a EC, PC and CP fits to the experimental cross sections and analysing powers of ^{116,124}*Sn,* 2_1^+.

For the 2_1^+ and 3_1^- states of ^{116}Sn and ^{124}Sn and for the 5_1^- state of ^{124}Sn we have fitted the experimental data using above four methods. The results are compiled in table 5.8 and plotted in figs. 5.6a, 5.6b and 5.6c. We know already from the collective analyses of these data that the collective model gives good fits. Since in the CP and CCP methods a rather large part of the collective amplitude is admixed also here the results are quite good. The differences between the CP and CCP methods are only small and not essential.

In general the EC and PC fits are also satisfactory, though not as good as the CP and CCP fits. For the 2^+ states we can see some differences between the curves of the EC and PC methods. Here the EC approach gives better fits, especially regarding the analysing powers.

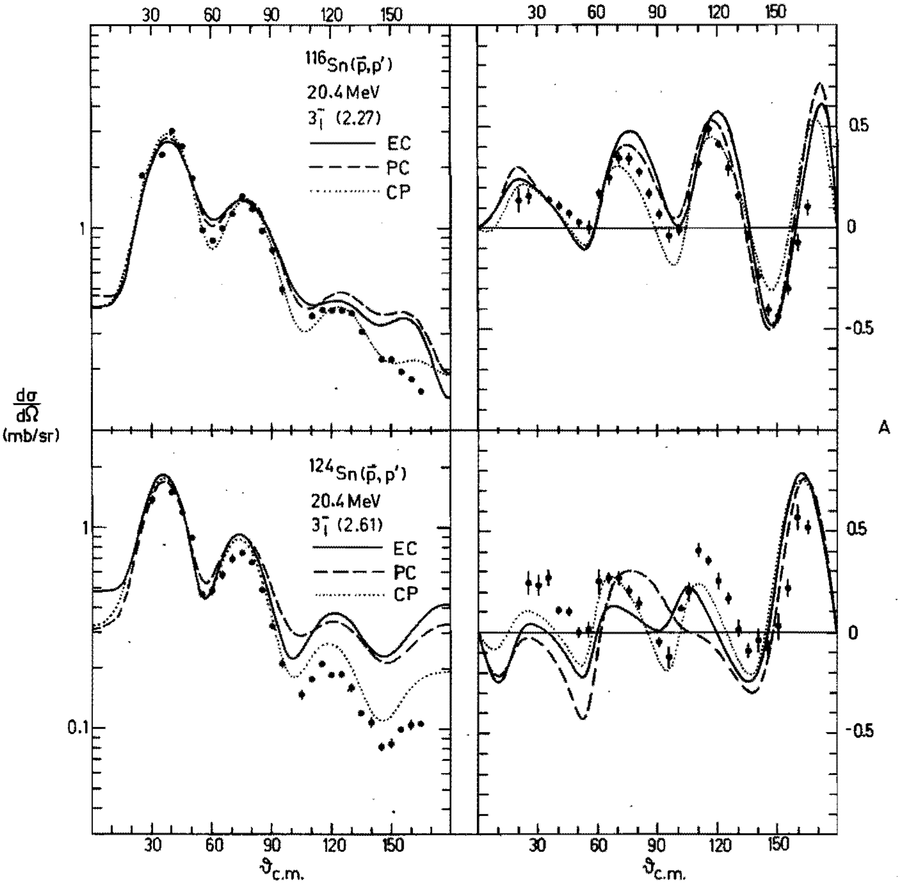

Fig. 5.6b EC, PC and CP fits in the experimental cross sections and analysing powers of ^{116,124}*Sn*, 3_1^-.

The chi squared values are remarkably lower for the EC method. This effect is caused by the fact that the microscopic contribution to the transition probability, D_{pv}, for the 2_1^+ is very small, so the calculated effective charge e_p is unrealistically high. Due to this large value of e_p, and consequently of λ_p, the fit to the analysing power is spoiled.

The EC fit for the 5_1^- state of ^{124}Sn is rather bad. The PC method was not possible here because of the lack of experimental B(EL) values. The core polarisation methods give good results so the real collective term is very important at higher L values, while the microscopic approach is incapable to describe the experimental data.

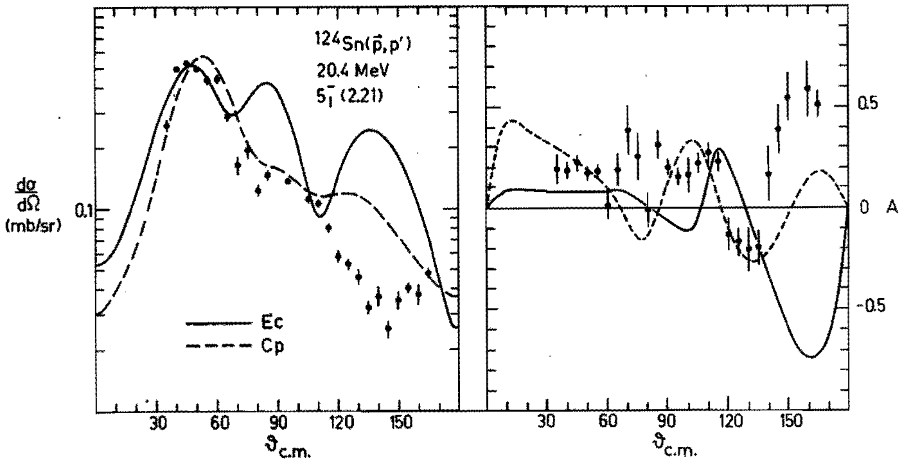

Fig. 5.6c EC and CP fits to the experimental cross section and analysing power of ^{124}Sn, 5_1^-.

Using the EC method we have analysed some states with the spectroscopic amplitudes of Gillet. We see from table 5.9 that the chi squared values of these fits are somewhat larger than those of the fits with the set of Allaart. For the eye there is hardly any difference between these two of fits.

We have already seen that the microscopic central interaction gives much larger cross sections than the non-central parts. We have performed some fits wherein we used the central instead of the valence interaction. The imaginary collective interaction was always included, using method EC. In nearly all cases the analysing power was fitted better with the valence (total) interaction than with the central interaction. For the cross sections, however, the opposite is true. The same result was found with the interaction of Austin etc. instead of the interaction of HJ etc. In general the differences between the valence and central fits are small, as can be seen in fig. 5.7 for ^{116}Sn, 2_1^+.

For the 2_1^+ state of ^{116}Sn we also performed calculations with the central nucleon-nucleon interaction of Austin, completed with the tensor interaction of Sprüng and the spin-orbit interaction of Eikemeier-Hackenbroich. The results of the variation process with different methods are presented in table 5.10, where we see that for the analysing power the results with the interactions of Austin etc.

Table 5.9 Comparison of the fits with the spectroscopic amplitudes S of Allaart and Gillet, using the effective charge method (EC, $\lambda_I=1$, $\lambda_G=0$).

A	L	S	λ_p	λ_n	χ^2_σ	χ^2_A	B(EL)
116	2	Allaart	1.02	2.11	4533	1058	1659
		Gillet	1.00	2.31	4656	790	1883
116	3	Allaart	4.86	1.50	1933	646	495516
		Gillet	3.48	1.67	2371	806	419304

Table 5.10 Fits for ^{116}Sn, 2^+ using the effective charge method (EC, $\lambda_I=1$, $\lambda_G=0$) and various nucleon-nucleon interactions.

N-N interaction							
central part	tensor part	s-o part	λ_p	λ_n	χ^2_σ	χ^2_A	B(EL)
HJ	EH	EH	1.02	2.11	4533	1058	1659
HJ	0	0	3.25	1.93	3348	1637	2137
Austin	Sprung	EH	2.67	1.57	4277	1032	999
Austin	0	0	3.83	1.51	3290	1320	1253

Table 5.11 The strengths of the central, tensor and spin-orbit parts of the microscopic interaction varied. The imaginary collective interaction is included.

							N-N interaction		
A	L	λ_{cen}	λ_{ten}	λ_{s-o}	χ^2_σ	χ^2_A	central part	tensor part	s-o part
116	2	1.64	0.00	0.00	3571	1203	Austin	Sprung	EH
		2.02	0.00	0.00	3499	1525	HJ	EH	EH
116	3	2.95	1.12	0.52	1796	530	HJ	EH	EH
124	2	0.47	3.48	1.41	668	354	HJ	EH	EH

better than those with the interactions of Austin etc. In most cases also the cross section is fitted better using HJ etc. When we compare the central interactions only, the results remain the same.

We remark further that the strengths of the neutron transition amplitude λ_n are smaller for the interaction of Austin. The proton contribution for the 2_1^+ state in only weak, so it can be neglected for the moment. So we see here that the HJ interaction is weaker than the Austin interaction, by a factor of about 1.5. The same factor was found by Alons (Alo80). In fig. 5.8 we have plotted some curves for both types of interactions.

In our program CHIMIX it is possible to take complex numbers for the parameters λ_p, λ_n etc. So we performed some fits without collective contributions compensating this with an extra free parameter, namely the phase of λ_p. The resulting cross sections, however, were nearly the same as with a real parameter λ_p: the structure was too flat. So in our model it is not possible to construct in a microscopic way transition amplitudes that can describe the cross section satisfactorily.

The essential property of the used imaginary term is that the form factor is peaked just outside the nuclear surface. This cannot be simulated by varying the parameters λ_p and λ_n.

The strengths of the nucleon-nucleon interactions used (see table 5.1) have been deduced by the various authors (HJ, Austin, etc.) by means of fitting procedures. Here we show the results of the variation of the strengths of the central, tensor and spin-orbit parts of the nucleon-nucleon interactions. As in all previous procedures also here the imaginary collective contribution has been added to the microscopic transition amplitudes. In this case we have three free parameters, i.e. one more than in the EC procedure. So a lower chi squared value can be expected. From the results, listed in table 5.11, we see that for ^{116}Sn, 2_1^+ the tensor and spin-orbit parameters have become zero and that the central enhancement is about equal to the value of λ_n in table 5.8 (T_p is small here). The cross sections are fitted better but the analysing powers worse. The similar effect was found already when we varied the central parts only. The fit of ^{116}Sn, 3_1^- is comparable with the fit with the EC method, but for ^{124}Sn, 2_1^+ a different result is found, see fig. 5.9. So we can conclude that the variation of the individual strengths gives us no new information. No

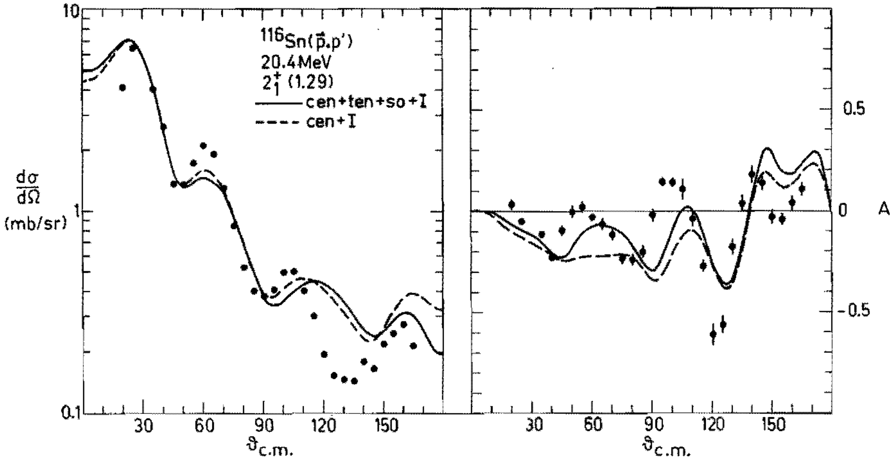

Fig. 5.7 *EC fits to the experimental cross section and analysing power of ^{116}Sn, 2_1^+, using the total (cen+ten+so+I) and the central (cen+I) microscopic interaction. In both cases the collective imaginary interaction is included.*

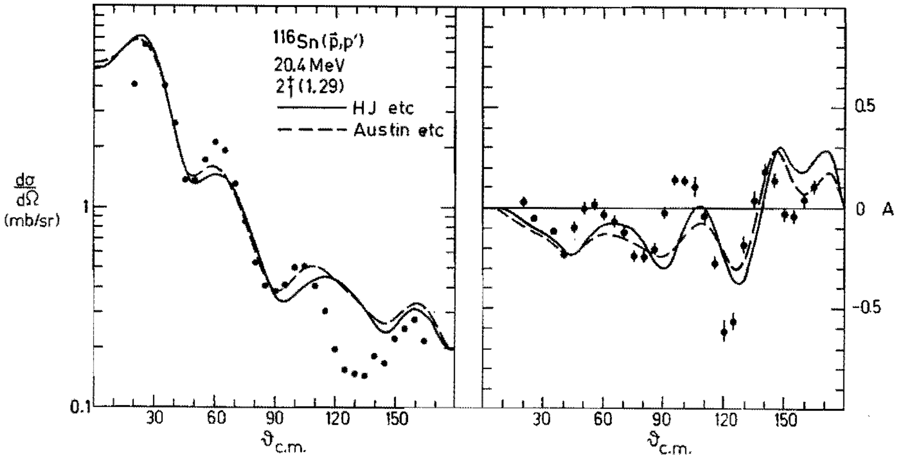

Fig. 5.8 *EC fits to the experimental cross section and analysing power of ^{116}Sn, 2_1^+, using the nucleon-nucleon interactions of HJ and Austin. In both cases the collective imaginary interaction is included.*

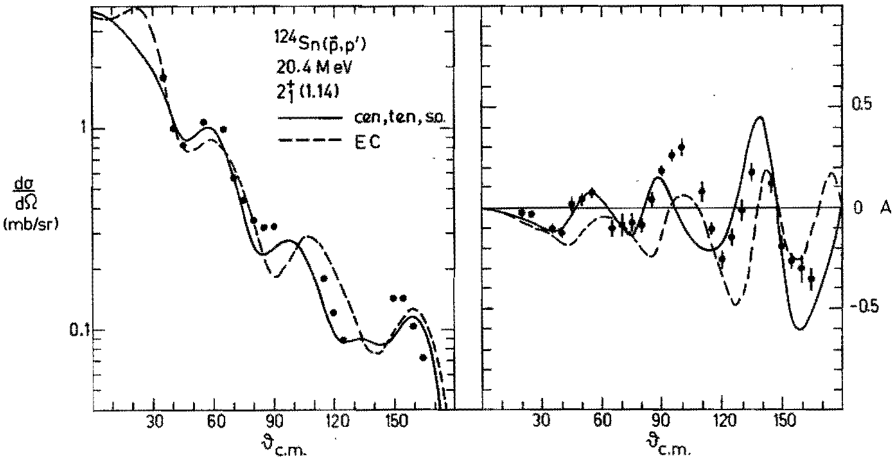

Fig. 5.9 EC fit and a fit wherein the separate strengths of the central (of HJ), tensor (of EH) and spin-orbit (of EH) parts of the microscopic interaction are varied. In both cases the collective imaginary interaction is included.

definite trend can be found, except that the non-central interactions are important for the fit of the analysing powers. Also when we use the interaction of Austin the same result was found. So in this way it is not possible to deduce the individual strengths of the various parts of the nucleon-nucleon interaction.

Conclusions

In this microscopic analysis we have shown that an imaginary interaction is needed to get a reasonable fit to the cross sections. When the neutrons have no effective charge, then the effective charge for the protons is calculated too high for the 2_1^+ states, which disturbs the analysing powers. For the high L values, only the core polarization methods give a reasonable description. The influence of different nucleon-nucleon interactions or spectroscopic amplitudes is in general rather small.

REFERENCES

Alk65 D.G. Alkhazov, Yu.P. Gangrskii, I.Kh. Lemberg and Yu.I. Udralov, Bull. Acad. Sci. USSR, Ser. Phys. 28 (1965) 149.

All79 K. Allaart, Vrije Universiteit Amsterdam, private communication.

Alo80 P.W.F. Alons, thesis, Vrije Universiteit Amsterdam (1980).

Amo78 Ken Amos, Amand Faessler, Iain Morrison, Ross Smith and Herbert Muether, Nucl. Phys. A304 (1978) 191.

Agr75 D.G. Agrawel and P.C. Sood, Phys. Rev. C11 (1975) 1854.

Aub79 R.L. Auble, Nuclear Data Sheets 28 (1979) 103.

Aus70 N. Austern, Direct nuclear reaction theories, Wiley, New York (1970).

Aus79 S.M. Austin, report Michigan State University C.L. 302 (1979).

Bar64 B.M. Bardin, M.E. Ricky, Rev. Sci. Instr. 35 (1964) 902.

Bec69 F.D. Becchetti Jr. and G.W. Greenlees, Phys. Rev. 182 (1969) 1190.

Bee70 O. Beer, A.El. Behay, P. Lopato, Y. Terrien, G. Vallois and Kamal K. Seth, Nucl. Phys. A147 (1970) 326.

Beu67 R. Beurty and J.M. Durand, Nucl. Instr. and Methods 57 (1967) 313.

Bla59 J.S. Blair, Phys. Rev. 115 (1959) 928.

Blo72 H.P. Blok, thesis, Vrije Universiteit Amsterdam (1972).

Blo75 H.P. Blok, J.C. de Lange and J.W. Schotman, Nucl. Instr. and Methods 128 (1975) 545.

Boh53 A. Bohr and B.R. Mottelson, Mat. Fys. Medd. Dan. Vid. Selsk., 27 (1953) 16 (see also Boh75).

Boh75 A. Bohr and B.R. Mottelson, Nuclear structure vol 2, Benjamin Inc., London (1975).

Bot81 J.M. Botman, thesis, Eindhoven University of Technology (1981).

Bri77 F.A. Brieva and J.R. Rook, Nucl. Phys. A291 (1977) 299 and 317.

Bri78 F.A. Brieva and J.R. Rook, Nucl. Phys. A297 (1978) 206.
F.A. Brieva and J.R. Rook, Nucl. Phys. A307 (1978) 493.
F.A. Brieva and B.Z. Georgiev, Nucl. Phys. A308 (1978) 27.

Bru77 P.J. Brussaard and P.W.M. Glaudemans, Shell model applications in nuclear spectroscopy; North Holland, Amsterdam (1977).

Car66 A.L. McCarthy and G.M. Crawley, Phys. Rev. 150 (1966) 935.

Cla56 C. Clausnitzer, R. Fleischmann and H. Schopper, Z. Phys. 144 (1956) 336.

Cle75 T.B. Clegg, Proceedings of the fourth International Symposium on Polarization Phenomena in Nuclear Reactions, Zuerich (1975), (eds. W. Gruebler and V. Koenig, Birkhauser Verlag, Basel, 1976) p. 111.

Eik71 H. Eikemeier and H.H. Hackenbroich, Nucl. Phys. A169 (1971) 407.

Fin80 R.W. Finlay, J. Rapaport, M.H. Hadizadeh, M. Mirzaa and D.E. Bainum, Nucl. Phys. A338 (1980) 45.

Ger71 H.V. Geramb and K.A. Amos, Nucl. Phys. A163 (1971) 337.

Ger73 H.V. Geramb, computer code MEPHISTO, unpublished (1973).

Gil67 V. Gillet, B. Giraud and M. Rho, Nucl. Phys. A103 (1967) 257.

Gil69 V. Gillet, B. Giraud and M. Rho, Phys. Rev. 178 (1969) 1695.

Gil76 V. Gillet, B. Giraud and M. Rho, Le Journal de Phys. 37 (1976) 189.

Gla67 C. Glashausser, R. de Swiniarski, J. Thirion and A.D. Hill, Phys. Rev. 164 (1967) 1437.

Gla69 C. Glashausser, R. de Swiniarski, J. Goudergues, R.M. Lombard, B. Mayer and J. Thirion, Phys. Rev. 184 (1969) 1217.

Gla70 H.F. Glavish, Proceedings of the third International Symposium on Polarizarion Phenomena in Nuclear Reactions, Madison 1970 (eds. H.H. Barschall and W. Haeberli, Univ. of Wisconsin Press, Madison, Wisc., (1971) p. 267.

Gre68 G.W. Greenlees, G.J. Pyle and Y.C. Tang, Phys. Rev. 171 (1968) 1115.

G.W. Greenlees, G.J. Pyle and Y.C. Tang, Phys. Lett. 26B (1968) 658.

Gun74 W.F. van Gunsteren, E. Boeker and K. Allaart, Z. Phys. 267 (1974) 87.

W.F. van Gunsteren and K. Allaart, Nucl. Phys. A236 (1974) 317.

Gun76 W.F. van Gunsteren, thesis, Vrije Universiteit Amsterdam (1976).

Hag70 H.L. Hagedoorn, J.W. Broer and F. Schutte, Nucl. Instr. and Methods 86 (1970) 253.

Hal75 P.J. van Hall, J.P.M.G. Melssen, H.J.N.A. Bolk, O.J. Poppema, S.S. Klein and G.J. Nijgh, Proc. of the fourth International Symposium on Polarization Phenomena in Nuclear Reactions, Zuerich (1975), (eds. W. Gruebler and V. Koenig, Birkhauser Verlag, Basel, 1976) p. 725 ff.

Hal77 P.J. van Hall, J.P.M.G. Melssen, S.D. Wassenaar, O.J. Poppema, S.S. Klein and G.J. Nijgh, Nucl. Phys. A291 (1977) 63.

Hal80 P.J. van Hall, J.F.A.G. Ruyl, J. Krabbenborg, W.H.L. Moonen and H. Offermans, Proceedings of the fifth International Symposion on Polarization Phenomena in Nuclear Reactions, Santa Fé (1980) paper 2.43.

Ham62 T. Hamada and I.D. Johnston, Nucl. Phys. 34 (1962) 382.

Hei72 J.A. van der Heide, thesis, Eindhoven University of Technology (1972).

Hod76 P.E. Hodgson, Phys. Lett. 65B (1976) 331.

Ino68 Makoto Inoue, Nucl. Phys. A119 (1968) 449.

Jam75 F. James and M. Roos, computer code MINUIT, Computer Physics Communications 10 (1975) 343.

Kap78 E.J. Kaptein, thesis, Vrije Universiteit Amsterdam (1978).
E.J. Kaptein, H.P. Blok and J. Blok, Nucl. Phys. A312 (1978) 97.

Kun69 P.D. Kunz, computer code CHUCK, University of Colorado, unpublished (1969).

Lep77 A. Lepine, C. Volant, M. Conjeaud, S. Harar and E.F. Da Silveira, Nucl. Phys. A289 (1977) 187.

Lov67 W.G. Love and G.R. Satchler, Nucl. Phys. A101 (1967) 424.

Mak68 W. Makofske, W. Savin, H. Ogata and T.H. Kruse, Phys. Rev. 174 (1968) 1429.

Mel78 J.P.M.G. Melssen, thesis, Eindhoven University of Technology (1978).

Mel82 J.P.M.G. Melssen, P.J. van Hall, S.D. Wassenaar, O.J. Poppema, G.J. Nijgh and S.S. Klein, Nucl. Phys. A376 (1982) 183.

Nij78 G.J. Nijgh, internal report NK-277, Eindhoven University of Technology (1978).

Nij79 F.C. van Nijmweegen, internal report VDF/CO 79-10, Eindhoven University of Technology (1979).

Owe64 L.W. Owen and G.R. Satchler, Nucl. Phys. 51 (1964) 155.

Pol81 J.H. Polane, thesis, Eindhoven University of Technology (1981).

Raa79 A.J. de Raaf, Nucl. Instr. and Methods 163 (1979) 313.

Ram72 A.V. Ramayya, J.L.C. Ford Jr., R.L. Robinson and J.H. Hamilton, Nucl. Phys. A193 (1972) 186.

Ray71 J. Raynal, Structure of Nuclei, Trieste Lectures (1971) 75.

Ray72 J. Raynal, code ECIS, Report IAEA-SMR-918 (1972) 281.

Ros53 M.E. Rose, Phys. Rev. 91 (1953) 610.

Sat67 G.R. Satchler, Nucl. Phys. A92 (1967) 273.

Sat69 G.R. Satchler, Isospin in nuclear physics, ed. D.H. Wilkinson, North Holland, Amsterdam (1969) 389.

Sat71 G.R. Satchler, Phys. Lett. 35B (1971) 279.

Sch72 J.P. Schiffer, Proc. Gull Lake Conf. on the two body forces in nuclei, eds. Austin and Crawly, Plenum, New York (1972) 205.

Sha61 A. de Shalit, Phys. Rev. 122 (1961) 1530.

She68 H. Sherif and J.S. Blair, Phys. Lett. 26B (1968) 489.

She70 H. Sherif and J.S. Blair, Nucl. Phys. A140 (1970) 33.

Sin75 B. Sinha, Phys. Reports 20C (1975) 1.

Smi77 J.W. Smits, thesis Rijksuniversiteit Groningen (1977).

Spr72 D.W.L. Sprung, Nucl. Phys. A182 (1972) 97.

Ste70 P.H. Stelson, F.K. McGowan, R.L. Robinson and W.T. Milner, Phys. Rev. C2 (1970) 2015.

Swi77 R. de Swiniarski, Dinh-Lien Pham and G. Bagieu, Can. J. of Phys. 55 (1977) 43.

Swi78 R. de Swiniarski, Dinh-Lien Pham and G. Bagieu, Phys. Lett. 79B (1978) 47.

Swi79 R. de Swiniarski, Dinh-Lien Pham, G. Bagieu and H.V. Geramb, Can. J. of Phys. 57 (1979) 540.

Tam65 T. Tamura, Rev. Mod. Phys. 37 (1965) 241.

Ter73 Y. Terrien, Nucl. Phys. A199 (1973) 65.

Y. Terrien, Nucl. Phys. A215 (1973) 29.

Ver72 B.J. Verhaar, W.C. Hermans and J. Oberski, Nucl. Phys. A195 (1972) 379.

B.J. Verhaar and L.D. Tolsma, DWBA code, Eindhoven University of Technology (1972), unpublished.

Ver74 B.J. Verhaar, Lecture notes in Physics 30 (1974) 268, Springer Verlag Berlin.

Vos72 H. Vos, thesis, Vrije Universiteit Amsterdam (1972).

Vri77 W.H. Vriend, thesis, Vrije Universiteit Amsterdam (1977).

Wap71 A.H. Wapstra, Nucl. Data Tables 9 (1971) 324.

Was80 S.D. Wassenaar, P.J. van Hall, S.S. Klein, G.J. Nijgh, O.J. Poppema, W.F. Feix, J.H. Polane and J.F.J. Dautzenberg, Proceedings of the fifth International Symposion on Polarization Phenomena in Nuclear Reactions, Santa Fé(1980) papers 2.44, 2.45, 2.46 and 2.47.

SAMENVATTING

Experimenten waarbij gepolariseerde protonen verstrooid worden aan atoomkernen zijn een belangrijk middel om de reactietheorie en het gebruikte kernmodel te testen. Twee gangbare modellen zijn daarvoor genomen, namelijk het collectieve model, waarbij de kern als één geheel wordt beschouwd en het microscopische of schillen-model waarbij ook rekening gehouden wordt met de nucleonen in de kern. Als de protonen gepolariseerd zijn, kan naast de differentiële werkzame doorsnede ook het analyserend vermogen bepaald worden. Deze grootheid is in sommige gevallen gevoeliger voor bepaalde parameters van reactietheorie en kernmodel.

We hebben de volgende kernen bestudeerd met een energie E_p = 20.4 MeV van de opvallende protonen ^{60,64}Ni (Z=28), ^{110,112,114}Cd (Z=48), ^{115}In (Z=49), ^{116,118,120,122,124}Sn (Z=50), en met 24.6 MeV: ^{86}Sr (N=48), ^{88}Sr (N=50) en ^{120}Sn (Z=50). Hierbij hebben we gebruik gemaakt van de gepolariseerde protonenbundel van de THE, met de bijbehorende meetopstelling (hoofdstuk 2). Van de elastische en inelastische verstrooiing hebben we de hoekverdelingen gemeten van de doorsnedes en de analyserende vermogens van 20-165 graden. De keuze van de energie van de protonen had de volgende redenen:

- Er is dan bijna geen compound-kernverstrooiing zodat de directe-reactietheorie kan worden toegepast.
- De beschikbare apparatuur, met name het cyclotron.
- Vergelijking met gegevens uit de literatuur.
- De grote positieve waarde van het analyserend vermogen van de eerste 2^+ toestand, gevonden bij kernen met een (bijna) gesloten neutronenschil. Dit analyserend vermogen kon slechts 'beschreven' worden door de verhouding λ van de spin-baan en de centrale deformatieparameters te vergroten van 1 (normaal) naar 2 (bij E_p = 20 MeV) of 3 (bij E_p = 17 MeV). Dit geldt bijvoorbeeld voor ^{54}Fe (N=28).

Dit laatste punt houdt ook verband met de keuze van de bestudeerde kernen, die op de Sr-isotopen na alle een (bijna) gesloten protonenschil hebben, om ook hiervoor de waarde van λ te bepalen. Verder zijn deze kernen gekozen omdat ze even-even zijn (behalve ^{115}In), middelzwaar en verkrijgbaar in de vorm van geschikte targets (dunne folies).

Vaak hebben we een serie isotopen genomen om het verloop van parameters met het massagetal te onderzoeken.

De elastische verstrooiing hebben we geanalyseerd met het standaard optisch model (eerste deel van hoofdstuk 4). De experimentele hoekverdelingen worden zeer goed beschreven. Doordat nu doorsnedes en analyserende vermogens aangepast moeten worden, zijn de optische modelparameters goed bepaald. De overeenstemming met parametersets uit de literatuur is zeer bevredigend. Voor de analyse van de inelastische verstrooiing volgens het collectieve model hebben we de gebruikelijke vervormde-golf Born-benadering (DWBA), of in een enkel geval de gekoppelde kanalen (CC) methode toegepast (tweede deel van hoofdstuk 4). De parameters in dit model zijn de deformatieparameters die gevonden worden door aanpassing van de theoretische curves aan de experimentele hoekverdelingen. Ook hier is de beschrijving van de experimenten in het algemeen heel goed te noemen. De door ons gevonden spin-baan deformatieparameters blijken echter normale waarden ($\lambda \simeq 1$) te hebben. Dus voor kernen met een gesloten protonenschil treedt bovengenoemd effect niet op. Hetzelfde geldt voor de Sr-isotopen omdat daar de energie al vrij hoog is ($E_p = 24.6$ MeV). De gevonden deformatieparameters zijn in goede overeenstemming met gegevens uit de literatuur.

Enkele gevallen willen we nog nader bespreken. De doorsnede van de 2^+-toestand van ^{60}Ni kon niet zo goed beschreven worden met de DWBA. Het bleek namelijk dat bij normering van de theoretische curve op de voorwaartse hoeken deze curve achterwaarts veel hoger lag dan de experimentele doorsnedes. Een CC berekening gaf een betere beschrijving, echter nog niet voldoende om dit verschijnsel te verklaren. Voor hetzelfde isotoop hebben we ook enige hoger-aangeslagen toestanden met de CC-theorie geanalyseerd. Door de verhouding van één- en twee-phonon bijdragen te varieren konden we voor enkele van de toestanden de structuur bepalen. ^{115}In is de enige kern met een oneven massagetal die we bestudeerd hebben. Volgens het z.g. weak-coupling model kunnen we deze kern beschouwen als een ^{116}Sn-kern met een gat in de protonenschil. De collectieve aangeslagen toestanden zijn dan opgesplitst maar moeten nog wel dezelfde structuur vertonen als de 'parent'-toestanden in ^{116}Sn. We hebben dit inderdaad heel duidelijk gevonden en de deformatieparameters van het L=2 multiplet stemmen goed overeen met weak-coupling berekeningen.

We hebben de inelastische verstrooiing aan de 2_1^+, 3_1^- en 5_1^- toestanden van ^{116}Sn en ^{124}Sn ook met behulp van het microscopische model geanalyseerd (hoofdstuk 5). In de literatuur zijn al enkele van dergelijke analyses gepubliceerd, maar experimentele analyserende vermogens waren toen niet beschikbaar. Verder zijn er aan Sn, vanwege de min of meer gesloten protonenschil, veel schillenmodelberekeningen (BCS) gedaan, zodat de benodigde spectroscopische amplitudes beschikbaar waren. De zuiver microscopische berekeningen, met de antisymmetrische DWBA, geven echter doorsnedes die veel te laag zijn en te vlak van structuur. Bovendien zijn de electromagnetische overgangswaarschijnlijkheden B(EL) te laag. Dat de doorsnede te vlak is, wordt veroorzaakt door het ontbreken van een imaginaire term in de gebruikte effectieve nucleon-nucleon wisselwerking. Toevoeging van zo'n term is dan ook noodzakelijk en we hebben daarvoor de collectieve imaginaire interactie genomen, volgens het enigszins 'frivole' model van Satchler. De veronderstelling dat de nucleonen in de binnenschillen geen bijdrage leveren is niet zo realistisch. Daarom hebben we deze 'core polarisatie' (CP) bijdragen in rekening gebracht teneinde het probleem van de te lage doorsnedes te kunnen oplossen. De CP kunnen we op twee manieren in rekening brengen n.l. door de effectieve ladingen van de protonen en neutronen te vergroten of door een reële collectieve term toe te voegen aan de microscopische en imaginaire wisselwerkingen. Op deze manieren konden de experimentele hoekverdelingen vrij goed beschreven worden, zij het nog niet zo goed als met het collectieve model mogelijk is. Voor de methode van de effectieve ladingen hebben we naast de bestaande procedure een variant ontwikkeld, die voor de 2^+ toestanden een beter resultaat geeft voor de analyserende vermogens. Het toevoegen van een deel van de reële collectieve term heeft tot gevolg dat het uiteindelijk resultaat veel op de collectieve aanpassing gaat lijken vanwege de sterke invloed van deze term. Vooral voor de L=5 toestand is dit heel duidelijk. De methode van de effectieve ladingen geeft hier een slecht resultaat. Het zou interessant zijn te proberen voor de collectieve termen microscopische equivalenten te vinden.

Concluderend kunnen we zeggen dat deze experimenten een goede test van de reactietheorie en de kernmodellen vormen, waarbij de analyserende vermogens een belangrijke rol spelen.

NAWOORD

Hierbij wil ik alle mensen, die aan de experimenten en aan de totstandkoming van dit proefschrift hebben bijgedragen, hartelijk bedanken.

Binnen de werkgroep 'experimentele kernfysica' van de THE zijn dit prof. Poppema en Piet van Hall, die het schrijven van het proefschrift begeleid hebben. De gehele meetopstelling is door de groep, een ieder op zijn vakgebied, opgebouwd. De experimenten werden door de groep als geheel uitgevoerd, tijdens de zogenaamde meetweken. In de loop der jaren hebben de volgende personen hun bijdrage geleverd: de fysici: prof. Poppema, Piet van Hall, Sieb Klein en Gerard Nijgh, de 'collega-promovendi': Frank Dautzenberg, Jos Melssen en Jan Polane, de technici: Jan van den Berg, Leo de Folter, Wim Gudden en Harm Rozema (die ook targets gemaakt heeft in het KVI te Groningen), de electronici: Gerard Hamers, Rob Janson en Peter Teunisse en de computerdeskundige Adri de Raaf. Fred van Nijmweegen heeft ons geholpen o.a. met de scalers en het Eurobussysteem.

Zonder een goed werkend cyclotron zouden de experimenten uiteraard niet mogelijk zijn geweest, waarvoor dank aan de bedrijfsgroep, o.a. Wim van Genderen, Frits van Hirtum, Adri Platje, Marinus Queens, Carel Soethout en Wim Verseijden.

Er is, zoals gebruikelijk bij dit soort onderzoek, zeer veel rekenwerk verricht op de computer. De service verleend op het Rekencentrum, waar de operators heel wat computeruitvoer voor ons hebben verwerkt, heeft veel bijgedragen aan het resultaat.

De volgende personen van de Vrije Universiteit te Amsterdam ben ik erkentelijk voor hun hulp. Klaas Allaart voor de spectroscopische amplitudes van tin, Peter Alons voor de berekeningen met ECIS, Henk Blok voor de programmas POESPAS en MEPHISTO en Jan van Hienen voor de informatie over de B(EL)'s.

De vele tekeningen zijn door Ruth Gruyters keurig verzorgd. Verder hebben Marijke Schilstra en Aafje de Wit tabellen getypt. Rian Teurlings heeft op voortreffelijke wijze het manuscript getypt en de lay-out verzorgd.

Voor zijn medewerking om het proefschrift af te ronden, ben ik Michael Rethans, chef van de afdeling SWP van Nixdorf Computer, erkentelijk.

LEVENSLOOP

25 december 1949	geboren te Leeuwarden, daarna opgegroeid in Berlikum (Fr).
april 1955- juli 1961	Chr. Nat. School te Berlikum.
juli 1965	mulodiploma B, aan de Chr. Nat. School, de 'Slotschool' te St. Annaparochie.
juli 1967	getuigschrift Hogereburgerschool B, aan de Chr. H.B.S. en M.M.S. te Leeuwarden.
augustus 1974	doctoraal examen natuurkunde, experimentele kernfysica, aan de Vrije Universiteit te Amsterdam.
april 1975- juli 1980	wetenschappelijk medewerker in dienst van de stichting F.O.M., in de werkgroep K VIII, experimentele kernfysica van de Technische Hogeschool te Eindhoven.
vanaf november 1980	medewerker in de groep Software Production (SWP) van Nixdorf Computer B.V. te Vianen (Z.H.)

STELLINGEN

behorende bij het proefschrift van

SIETSE DIRK WASSENAAR

Eindhoven, 12 november 1982

1. In het 'core polarisatie-model' volgt Terrien1) een procedure waarbij alleen de protonen-overgangen bijdragen tot de electromagnetische overgangswaarschijnlijkheid B(EL). Dit is niet correct daar ook de neutronen-overgangen een bijdrage geven als de effectieve lading van de neutronen groter dan 0 is 2).

   1) Y. Terrien, Nucl. Phys. A199 (1973) 65, Nucl. Phys. A215 (1973) 29.
   2) dit proefschrift, hoofdstuk 5.

2. In het 'frivole' model van Satchler1) wordt de imaginaire microscopische wisselwerking gesimuleerd door de collectieve imaginaire wisselwerking toe te voegen aan de microscopische termen. Het belangrijkste aspect van deze wisselwerking is niet het imaginair zijn, maar de radiële vorm ervan 2).

   1) G.R. Satchler, Phys. Lett. 35B (1971) 279.
   2) dit proefschrift, hoofdstuk 5.

3. Volgens het 'folding-model' is het mogelijk de middelbare straal (rms) van de neutron-distributie van een kern te bepalen, uit de elastische verstrooiing van protonen van niet te hoge energie1).
   Het resultaat is echter sterk afhankelijk van de gebruikte effectieve nucleon-nucleon wisselwerking. De waarden die o.a. Boyd en Lombardi 2) bepaald hebben zijn dan ook twijfelachtig.

   1) G.W. Greenlees, G.J. Pyle en Y.C. Tang, Phys. Rev. 171 (1968) 1115.
   2) J.C. Lombardi, R.N. Boyd, R. Arking en A.B. Robbins,
      Nucl. Phys. A188 (1972) 103.

4. Het verdient aanbeveling om in theoretische berekeningen van differentiële werkzame doorsneden ook de curves van de analyserende vermogens te publiceren. Dit geldt uiteraard ook voor andere gebieden waarbij nevenresultaten van theoretische berekeningen waardevol kunnen zijn voor experimentatoren.

5. De hoeveelheid werk, gemoeid met het programmeren van een algemeen software-pakket voor administratieve doeleinden, wordt meestal sterk onderschat.

6. Door het verschijnen van het rapport over de aard van het Schriftgezag 1) is niet het gezag van de Bijbel verminderd, maar wel dat van de Generale Synode van de Gereformeerde Kerken in Nederland.

   1) "God met ons", Kerkinformatie, nr. 113, feb. 1981; uitgave: Dienstencentrum van de Gereformeerde Kerken in Nederland te Leusden.

7. De terugkeer naar de ambachtelijke werkwijze van beroemde orgelbouwers uit de zeventiende en achttiende eeuw, is het belangrijkste kenmerk van de vooruitgang in de huidige orgelbouw in Nederland 1,2).

   1) W.A. Reil, Organist en Eredienst, maandblad van de gereformeerde organistenvereniging, mei 1982, p.93.
   2) Jan Jongepier, Organist en Eredienst, mei 1981, p.68.

8. De sterke opkomst van het plankzeilen, als ontspanningsbezigheid, is mede te verklaren uit het toenemend individualisme in onze maatschappij.

9. De kop in het zand steken, ten aanzien van het milieubeheer, is een zeer gevaarlijke bezigheid geworden.